DISSERTATION

CLIMATOLOGY AND VARIABILITY OF ATMOSPHERIC RIVERS OVER THE NORTH PACIFIC

Submitted by

Bryan D. Mundhenk

Department of Atmospheric Science

In partial fulfillment of the requirements

For the Degree of Doctor of Philosophy

Colorado State University

Fort Collins, Colorado

Summer 2017

Doctoral Committee:

Advisor: Elizabeth A. Barnes
Co-Advisor: Eric D. Maloney

David A. Randall
Jay M. Ham

ABSTRACT

CLIMATOLOGY AND VARIABILITY OF ATMOSPHERIC RIVERS OVER THE NORTH PACIFIC

Atmospheric rivers (ARs) are plumes of intense water vapor transport that dominate the flux of water vapor into and within the extratropics. Upon landfall, ARs are a major source of precipitation and often trigger weather and/or hydrologic extremes. Over time, landfalling AR activity, or a lack thereof, can influence periods of regional water abundance or drought. An objective detection algorithm is developed to identify and characterize these features using gridded fields of anomalous vertically integrated water vapor transport. Output from this algorithm enables the investigation into the relationships between tropical variability and ARs over the North Pacific undertaken in this dissertation.

In the first segment of this study, an all-season analysis of AR incidence within the North Pacific basin is performed for the period spanning 1979 to 2014. The variability of AR activity due to the seasonal cycle, the El Niño-Southern Oscillation (ENSO) cycle, and the Madden-Julian oscillation (MJO) is presented. The results highlight that ARs exist throughout the year over the North Pacific. In general, the seasonal cycle manifests itself as northward and westward displacement of AR activity during boreal summer, rather than a seasonal change in the total number of ARs within the domain. It is also shown that changes to the North Pacific mean-state due to the ENSO cycle and the MJO may enhance or completely offset the seasonal cycle of AR activity, but that such influences vary greatly based on location within the basin.

The second segment of this study investigates ARs at high northern latitudes. Comparatively little is known about the dynamics supporting these ARs in contrast to their mid-latitude counterparts. ARs are found to occur near the Gulf of Alaska and the U.S. West Coast with similar frequency, but with different seasonality. Composited atmospheric conditions reveal that a broad height anomaly over the northeast Pacific is influential to AR activity near both of these regions. When a positive height anomaly exists over the northeast Pacific, AR activity is often deflected poleward toward Alaska, while the U.S. West Coast experiences a decrease in AR activity, and vice versa. This tradeoff in AR activity between these two regions applies across a range of time scales, not just with respect to individual transient waves. Both ARs and

height anomalies are found to be associated with Rossby wave breaking, thereby dynamically linking the modulation of AR activity with broader North Pacific dynamics.

The third segment of this study explores the predictability of anomalous landfalling AR activity within the subseasonal time scale (approximately 2–5 weeks). An empirical prediction scheme based solely on the initial state of the MJO and the stratospheric quasi-biennial oscillation (QBO) is constructed and evaluated over 36 boreal winter seasons. This scheme is based on the premise that the MJO modulates landfalling AR activity along the west coast of North America within the subseasonal time scale by exciting large-scale circulation anomalies over the North Pacific. The QBO is found to further modulate the MJO–AR relationship. The prediction scheme reveals skillful subseasonal "forecasts of opportunity" when knowledge of the MJO and the QBO can be leveraged to predict periods of increased or decreased AR activity. Moreover, certain MJO and QBO phase combinations provide predictive skill competitive with, or even exceeding, a state-of-the-art numerical weather prediction model.

ACKNOWLEDGMENTS

I wholeheartedly acknowledge the incredible support that I received throughout my time at CSU that enabled the timely completion of this dissertation. Specifically, I offer my sincere thanks to:

- My co-advisors Libby Barnes and Eric Maloney for taking me on as a student and for their unwavering support and guidance.
- My committee members Dave Randall and Jay Ham for their willingness to serve and provide candid feedback.
- Barnes research group members, especially the "original" group members Chengji Liu and Marie McGraw for pretty much everything, to Kyle Nardi for being a great summer intern whose explorations helped launch the research in Chapter 3, and to Cory Baggett whose own research inspired some aspects of the research in Chapter 4.
- Maloney research group members for the many thought-provoking conversations.
- Ammon Redman and Matt Bishop for their deft systems administrator/IT support.
- Mark Branson for his help exhausting my National Center for Atmospheric Research Educational Computing Request allocation (#UCSU0045). Though that work did not make the cut for this dissertation, the research detour was educational nonetheless.
- Chris Slocum for sharing this LaTeX dissertation template.
- Bob Tournay for encouraging me to apply to CSU.
- My wife Kelly for delaying her career ambitions and enduring yet another set of moves all while providing her untiring support.

This academic endeavor and research was supported by the United States Air Force. That being said, the conclusions expressed in this dissertation are those of the author and do not reflect the official policy or position of the United States Air Force, Department of Defense, or the U.S. Government. I acknowledge and appreciate the additional travel and/or publication support provided by the National Science Foundation Climate and Large-Scale Dynamics Program, the National Oceanic and Atmospheric Administration

(NOAA) Modeling, Analysis, Predictions, and Projections Program, and the NOAA National Weather Service Office of Science and Technology. Thanks, as well, to the MAC Foundation of Fort Collins for the generous student travel award.

TABLE OF CONTENTS

CHAPTER 1

INTRODUCTION

1.1. THAT WHICH IS CALLED AN “ATMOSPHERIC RIVER”

Prominent features in infrared and/or visible geostationary satellite imagery are bands of mixed clouds that extend from the tropics into the extratropics (see, for example, Figure 1.1a). McGuirk et al. (1987) described these features that are frequently observed over the Pacific Ocean as “moisture bursts.” When observed by polar-orbiting microwave sensors, the same features often appear as narrow plumes of high amounts of integrated water vapor (IWV) extending into and through the extratropics (see Figure 1.1b). These features are not uncommon; indeed, satellite imagery reveals that, at any given time, approximately 3–5 of these features exist in each hemisphere in some stage of development (e.g., Zhu and Newell 1998). The seminal work of Newell et al. (1992) first described these bands of enhanced moisture flux as “tropospheric rivers.” The “river” reference relates to early estimates of the associated transport of water at volumetric flow rates similar to that of the world’s largest rivers (e.g., Zhu and Newell 1998). The “tropospheric” was soon replaced by “atmospheric” for a string of influential papers regarding atmospheric rivers (ARs) over two decades ago (Zhu and Newell 1994; Newell and Zhu 1994; Zhu and Newell 1998).

Studies nearly a decade later further characterized ARs as transient regions within the warm conveyor belt of the pre-cold-frontal region of extratropical cyclones (e.g., Ralph et al. 2004, 2005). The same studies documented characteristic dimensions of these features: (1) high water vapor content (e.g., IWV $\geq$ 2 cm); (2) strong low level winds ($\geq$ 12.5 m s^{-1} in the lowest 2 km); and (3) a shape that is narrow ($\sim$300-500 km) and long ($\geq$ 2000 km). However, this characterization of ARs is not without confusion, complication, and disagreement regarding its application (e.g., Knippertz and Wernli 2010; Sodemann and Stohl 2013).

One area of uncertainty has been the dominant source of the water vapor within ARs. Bao et al. (2006), for example, categorized two types and/or life stages of ARs: those that are dominated by local moisture flux convergence and those that are more representative of long-distance, river-like transport. After analyzing

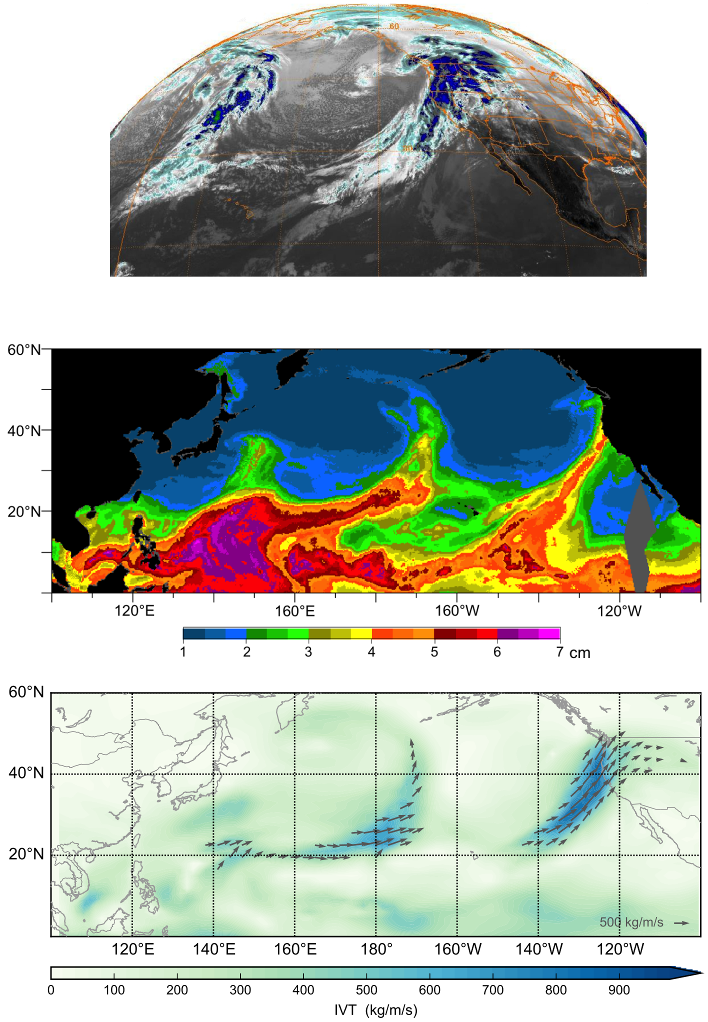

FIG. 1.1. Characteristic ARs over the central and eastern North Pacific on 9 February 2017; one AR is impacting the U.S. West Coast. (top) 1800 UTC GOES-15 enhanced infrared (10.2–11.2 μm) satellite image (Knapp 2008). (center) 1200-2400 UTC Special Sensor Microwave Imager/Sounder meshed image of integrated water vapor (IWV; cm) courtesy of the NOAA Earth System Research Laboratory. (bottom) daily mean integrated water vapor transport (IVT; kg m^{-1} s^{-1}) from MERRA-2 (GMAO 2015); IVT vectors highlight two ARs identified by the detection algorithm documented in Appendix A.

the water vapor budget of ARs in the North Pacific, Cordeira et al. (2013) described a continuum of remote and local moisture sources important in the development and maintenance of each AR's moisture flux. More recently, Dacre et al. (2015) documented the importance of local moisture sources associated with ARs in the North Atlantic. Thus, ARs not only represent the direct transport of water vapor from the tropics into the extratropics as the "river" name suggests, but also characterize a mix of remote and local moisture sources. Therefore, ARs are not always analogous to so-called tropical moisture exports (Knippertz and Wernli 2010;

Ralph et al. 2017). Some of the disagreement regarding the dominant source of water vapor may also be ascribed to differing perspectives regarding the transport. For example, the static images in Figure 1.1 suggest an Eulerian perspective of transport, while a Lagrangian perspective may be more appropriate to characterize the evolving nature of the transport (evaporation, moisture convergence, rainout, etc.) (e.g., Ralph et al. 2011).

Another area of complication regarding ARs has been their association and complex interplay with other atmospheric phenomena. The knowledge that horizontal water vapor transport within the troposphere is dominated by elongated regions within the warm sector of extratropical cyclones predates any discussion of ARs (e.g., Palmén and Newton 1969; Browning and Pardoe 1973). In fact, ARs are part of the three-dimensional flow within the warm sector of extratropical cyclones (e.g., Sodemann and Stohl 2013). However, while ARs have been found to be dynamically related to extratropical cyclones, they should be considered as distinct features with their own evolution and lifecycle (Sodemann and Stohl 2013). Therefore, ARs may be related to, but are also distinct from, a cyclone's warm conveyor belt (e.g., Carlson 1998) or the so-called moisture conveyor belt (Bao et al. 2006).

Perhaps because of the consternation surrounding the term AR events were held at the American Geophysical Union's 2016 Fall Meeting and the American Meteorological Society's 2017 Annual Meeting, at the request of the editor of the *Glossary of Meteorology*, to better define the term (Ralph et al. 2017). The events focused on the AR science and definitions applied in recent studies and discussed the overlap of ARs with related phenomena (Ralph et al. 2017). The result is the definition of AR, and accompanying schematic (see Figure 1.2), that appear in the online *Glossary of Meteorology* as of 1 May 2017 (American Meteorological Society 2017):

> A long, narrow, and transient corridor of strong horizontal water vapor transport that is typically associated with a low-level jet stream ahead of the cold front of an extratropical cyclone. The water vapor in atmospheric rivers is supplied by tropical and/or extratropical moisture sources. Atmospheric rivers frequently lead to heavy precipitation where they are forced upward—for example, by mountains or by ascent in the warm conveyor belt. Horizontal water vapor transport in the midlatitudes occurs primarily in atmospheric rivers and is focused in the lower troposphere.

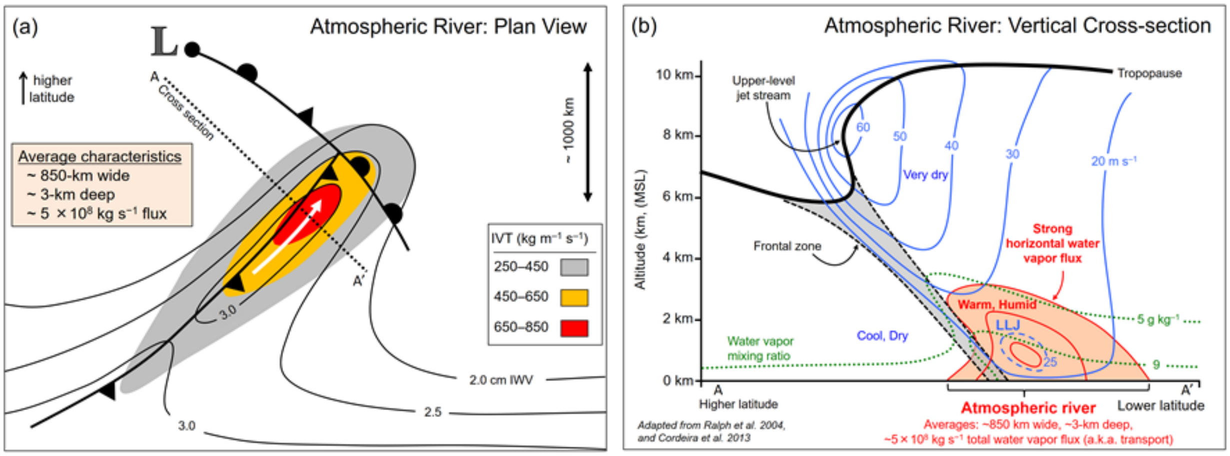

FIG. 1.2. Schematic summary of the structure and strength of an AR based on dropsonde measurements deployed from research aircraft across many ARs and on corresponding reanalyses that provide the plan-view context. Magnitudes of variables represent an average midlatitude AR. Average width is based on AR boundaries defined by vertically integrated water vapor transport (IVT; from surface to 300 hPa) lateral boundary threshold of 250 kg m^{-1} s^{-1}. Depth corresponds to the altitude below which 75% of IVT occurs. The total water vapor transport (a.k.a. flux) corresponds to the transport along an AR, bounded laterally by the positions of IVT = 250 kg m^{-1} s^{-1} and vertically by the surface and 300 hPa. (a) Plan view including parent low pressure system and associated cold, warm, and warm-occluded surface fronts. IVT is shown by color fill (magnitude; kg m^{-1} s^{-1}) and direction in the core (white arrow). Vertically integrated water vapor (IWV; cm) is contoured. A representative length scale is shown. The position of the cross section shown in (b) is denoted by the dashed line A-A'. (b) Vertical cross-section perspective, including the core of the water vapor transport in the AR (orange contours and color fill) and the pre-cold-frontal low-level jet (LLJ), in the context of the jet-front system and tropopause. Water vapor mixing ratio (green dotted lines; g kg^{-1}) and cross-section-normal isotachs (blue contours; m s^{-1}) are shown. Figure and caption from American Meteorological Society (2017).

Notwithstanding confusion and disagreement regarding terminology, ARs have been and remain an active research focus. Ralph et al. (2017) documents a rapid increase in publications using the term "atmospheric river" from fewer than 10 articles before 2004 to over 600 by late 2016. Certainly the advent of new satellite measurements of IWV has benefited this research, as has a set of field experiments during which research aircraft probed ARs (e.g., Ralph et al. 2016). Perhaps even more supportive of this rapid expansion of research is the fact that ARs are identifiable within ubiquitous gridded datasets of IWV or moisture flux (e.g., reanalysis datasets, numerical weather prediction output).

Interest in AR research—and perhaps research funding—is buoyed by some oft-referenced numbers relating to ARs. For example, approximately 90% of the total meridional water vapor flux across 35°N is attributed to ARs; meanwhile, these structures only cover about 10% of the total hemispheric circumference at that latitude (Zhu and Newell 1998). Or that ARs have been observed that transport water vapor at a rate of 13–26 km^3 per day, a rate equivalent to 7.5–15 times the average daily discharge of the Mississippi River into the Gulf of Mexico (Ralph et al. 2005, 2011). Certainly, ARs contribute significantly to the global climate and the global hydrologic cycle (e.g., Newman et al. 2012). However, it is important to note that while ARs are generally synoptic in scale, they are comprised of multi-scale contributions (i.e, time-mean, low-frequency, and synoptic components); therefore, these "sound bite" numbers should be interpreted as such (Newman et al. 2012).

Perhaps even more than the statistics regarding ARs themselves, the wide-ranging impacts associated with ARs have motivated—and continue to motivate—research into these features. ARs give rise to a dichotomy of both environmental and societal risks and benefits, in that they are both responsible for hazards and are the main agent of water supply for many coastal locations (e.g., Ralph and Dettinger 2011). For example, landfalling ARs supply roughly 40–50% of northern California's annual precipitation (Guan et al. 2012a; Dettinger et al. 2011). Meanwhile, the same landfalling features can trigger extreme precipitation events and catastrophic flooding, especially in locations with complex terrain (e.g., Ralph et al. 2006). On longer time scales, up to three quarters of persistent droughts along the U.S. West Coast have been ended by a landfalling AR (Dettinger 2013).

Based on the growing body of research regarding ARs, it appears the term "atmospheric river" shall endure. Though the term and concept may be fairly new in comparison to many other meteorological phenomena, the AR name and associated conceptual model have their benefits. First, the name is rather straightforward and intuitive even if, at times, the river aspect may be misleading. The model is also rather easy to communicate with lay individuals. A second benefit is the AR model enables feature identification and characterization, features that may then be related to (1) large-scale dynamics, (2) hydrologic cycle contributions, and (3) local impacts. Third, the AR model enables feature analysis that may be more fruitful than impact analysis alone. By definition, ARs constitute the local extremes of moisture flux in AR-prone regions. Though ARs may be associated with extratropical cyclones, the close relationship between ARs and their impacts positions ARs closer to impacts than, say, an analysis of extratropical cyclones and their impacts. Additionally, impact-only analysis can be muted when expanded beyond individual watersheds (e.g., grid cell mean of precipitation rate) and do not always characterize the potential extreme impacts (landslide, etc.). Furthermore, new research shows that the moisture flux associated with ARs is more predictable than the related impacts (e.g., precipitation) (Lavers et al. 2016). Fourth and finally, as noted by Gimeno et al. (2014), the AR model enables the attribution of socioeconomic impacts to a meteorological phenomenon and, thus, bolsters a direct link between researcher and decision makers.

1.2. SCOPE AND ORGANIZATION

The research documented in this dissertation aims to assess the temporal and spatial variability of ARs over the North Pacific. More specifically, the overarching research goal is to investigate how variability associated with tropical climate anomalies—namely the ENSO cycle and the MJO, at interannual and intraseasonal time scales, respectively—impacts ARs over the North Pacific. This research addresses questions such as:

- What dynamical mechanisms are most responsible for the influential relationships?
- What is the time evolution of the mid- and high-latitude response to tropical variability?
- How do changes in the atmospheric and/or oceanic mean-state modify these relationships?
- Do such changes appear predominantly in terms of AR frequency of occurrence, intensity, location, and/or evolution?
- Do these relationships provide predictive power such that they may be useful for the operational forecasting of ARs and/or their impacts?

In exploring these questions, this research advances the dynamical understanding of ARs and their variability, with implications regarding the prediction of the myriad impacts linked to this high-impact phenomenon.

Chapter 2 documents the all-season climatology of ARs over the North Pacific and assesses the variability in AR frequencies due to: 1) the seasonal cycle, 2) the ENSO cycle, 3) the MJO, and 4) their interactions.

To emphasize how these modes of variability impact local AR frequencies, AR incidence for five subregions of societal importance within the broader North Pacific domain are shown. This work is also published, with slight modifications, in *Journal of Climate* as:

> Mundhenk, B. D., E. A. Barnes, and E. D. Maloney, 2016: All-season climatology and variability of atmospheric river frequencies over the North Pacific. *J. Climate*, **29**, 4885–4903, doi:10.1175/JCLI-D-15-0655.1.

Chapter 3 compares and contrasts the occurrence and attributes of "high-latitude" ARs identified near southern Alaska with the comparatively well-documented ARs that occur near the U.S. West Coast. Common meteorological conditions associated with these ARs and the differences between them are shown. This chapter also investigates the large-scale atmospheric dynamics that help explain the variability in AR activity near these locations at synoptic, subseasonal, and interannual time scales. This work is also published, with slight modifications, in *Journal of Geophysical Research: Atmospheres* as:

> Mundhenk, B. D., E. A. Barnes, E. D. Maloney, and K. M. Nardi, 2016: Modulation of atmospheric rivers near Alaska and the U.S. West Coast by northeast Pacific height anomalies. *J. Geophys. Res. Atmos.*, **121**, 12751–12765, doi:10.1002/2016JD025350.

Chapter 4 investigates the predictability of anomalous landfalling AR activity along the west coast of North America within the subseasonal time scale. The text describes the construction and evaluation of an empirical prediction scheme based solely on the initial state of the MJO and the stratospheric quasi-biennial oscillation (QBO). This chapter also compares the skill of this empirical prediction scheme with a state-of-the-art numerical weather prediction model. This work has been submitted to *npj Climate and Atmospheric Science* as:

> Mundhenk, B. D., E. A. Barnes, E. D. Maloney, and C. F. Baggett, 2017: Skillful empirical subseasonal prediction of landfalling atmospheric river activity using the Madden-Julian oscillation and

quasi-biennial oscillation, submitted to *npj Climate and Atmospheric Science*.

Chapter 5 briefly summarizes the scientific impact and significance of the results of this body of research and lists possible extensions as "future work." Appendices to this dissertation provide additional information regarding the AR detection algorithm (Appendix A) and data access and availability (Appendix B).

CHAPTER 2

CLIMATOLOGY AND VARIABILITY OF ATMOSPHERIC RIVER FREQUENCIES[1]

2.1. INTRODUCTION

Atmospheric rivers (ARs) give rise to a dichotomy of both environmental and societal risks and benefits. With associated impacts ranging from torrential rainfall to replenishment of water reserves, ARs merit attention from not only scientists and operational forecasters, but also governments, resource managers, and local populations. Deservingly, ARs remain an active area of scientific research since their naming by Zhu and Newell over two decades ago (see Zhu and Newell 1994; Newell et al. 1992; Newell and Zhu 1994; Zhu and Newell 1998) and since the widespread availability of meteorological satellite data facilitated such inquiries. ARs have been the focus of numerous articles, field campaigns, and initiatives in the recent past. Such investigations have elevated the understanding of these features and clarified their associated local dynamics, but the extent to which variations in large-scale dynamics regulate the frequency and character of these events is not as well understood.

ARs are often characterized by their plumelike structure of focused tropospheric water vapor content and intense low-level winds (see Ralph et al. 2004; Gimeno et al. 2014, and references therein). While ARs have been found to be dynamically related to extratropical cyclones that support the synoptic-scale water vapor transport, they should be considered as distinct features with their own evolution and lifecycle (Sodemann and Stohl 2013). Isolating the dominant source of moisture within individual ARs remains an active research topic. Bao et al. (2006), for example, categorized two types and/or life stages of ARs: those that are dominated by local moisture flux convergence and those that are more representative of long-distance, river-like transport. After thoroughly analyzing the water vapor budget of two ARs in the North Pacific, Cordeira et al. (2013) described a continuum of remote and local moisture sources important in the development and maintenance of each AR's moisture flux. More recently, Dacre et al. (2015) documented

[1] Mundhenk, B. D., E. A. Barnes, and E. D. Maloney, 2016: All-season climatology and variability of atmospheric river frequencies over the North Pacific. *J. Climate*, **29**, 4885–4903, doi:10.1175/JCLI-D-15-0655.1. © American Meteorological Society. Used with permission.

the importance of local moisture sources associated with intense systems in the North Atlantic. Whether remote or local moisture sources dominate, ARs often contribute substantially to the water vapor flux within the atmospheric branch of the hydrologic cycle.

The majority of the recent work regarding ARs in the Pacific region focuses on these filamentary features making landfall along the west coast of North America, if not more specifically, along the contiguous U.S. West Coast. Furthermore, many of these recent studies are limited in scope to some manifestation of a Northern Hemisphere cool season or extended boreal winter (e.g., Payne and Magnusdottir 2014; Warner et al. 2015; Kim and Alexander 2015), perhaps due in part to their comparatively small study domains. Here, we take a broader perspective and examine the climatology and large-scale variability of ARs in the North Pacific basin without restricting ourselves to landfalling and/or wintertime features. We aim to provide insight into the existence of ARs throughout the year, with a deliberate look at how their frequency of occurrence varies by location, by season, and by changes in the background state due to climate variability. In doing so, we will spatially and temporally expand upon the work of Neiman et al. (2008b) who compared and contrasted a sample of summertime and wintertime ARs along the west coast of North America and noted seasonal differences in their character and impacts, but stopped short of assessing impacts due to variability beyond seasonality.

Earlier works by Higgins et al. (2000) and others revealed that tropical variability can influence the intensity and location of circulation anomalies in the extratropical Pacific and downstream, translating into variability in the poleward transport of water vapor. In specific reference to ARs, Bao et al. (2006) hypothesized the possible impacts that El Niño-Southern Oscillation (ENSO) may have on the direct transport of tropical moisture over the eastern Pacific, suggesting that such moisture exports are likely enhanced during ENSO neutral conditions and suppressed during El Niño periods. Similarly, Ryoo et al. (2013) detailed how ENSO may modify the subtropical jet and Rossby wave breaking near the U.S. West Coast, thereby impacting the region's tropospheric moisture transport and extreme precipitation events. Based on a detailed review of one winter's snow in California's Sierra Nevada, Guan et al. (2013) documented the potential impacts of large-scale variability (i.e., Arctic Oscillation, Pacific-North American teleconnection, and ENSO) on post-landfall AR-related impacts. Furthermore, Payne and Magnusdottir (2014) found that El Niño conditions result in an increase in the number of wintertime ARs making landfall along the west coast of North America and an equatorward shift in the mean latitude of landfall, while La Niña conditions reduce the number of wintertime landfalling ARs and shift the mean latitude of landfall poleward. Others have identified relationships between the Madden-Julian oscillation (MJO) and individual AR events over the Pacific Ocean (Ralph et al. 2011) and/or AR-related impacts following landfall along the U.S. West Coast (Guan et al. 2012b).

The purpose of this research detailed in this chapter is to explore the climatology of ARs over the North Pacific and the impacts of seasonality and climate variability on AR frequencies within this domain. We first develop an alternative anomaly-based method to identify ARs from gridded data. We then evaluate the climatology of ARs over the North Pacific. Finally, we use a compositing approach to assess variability about this climatology due to: 1) seasonality, 2) ENSO, 3) MJO, and 4) their interactions. To emphasize how these forms of variability impact local AR frequencies, we also examine AR incidence for five subregions within the broader North Pacific domain.

The remainder of this chapter is organized as follows: data and methods are outlined in Section 2.2; the climatology and variability of ARs in the North Pacific are presented in Section 2.3; further discussion and the conclusions of this study are found in Section 2.4; Appendix A of this dissertation provides additional information regarding the AR detection algorithm.

2.2. DATA AND METHODS

2.2.1. Data Sources

2.2.1.1. Atmospheric Variables

We employ the National Aeronautics and Space Administration's Modern-Era Retrospective Analysis for Research and Applications (MERRA) reanalysis dataset as the source for all atmospheric variables in this study. Though the MERRA dataset was chosen because of its refined representation of the atmosphere's hydrological cycle (Rienecker et al. 2011), other studies have found few differences among the suite of current generation reanalyses in their representation of ARs (e.g., Lavers et al. 2012, 2013). Thirty-six years (1979–2014) of instantaneous horizontal winds and specific humidity were retrieved at native spatial resolution ($\frac{1}{2}^{\circ}$ latitude $\times$ $\frac{2}{3}^{\circ}$ longitude) and 6-hourly temporal resolution on isobaric surfaces. The use of instantaneous fields is preferential for the objective detection of AR-like filamentary features; additionally, the sub-daily temporal resolution is favored for the study of features that may exist at or near their maximum intensity for less than one day.

2.2.1.2. El Niño-Southern Oscillation

ENSO conditions are characterized by the Oceanic Niño Index (ONI), the National Oceanic and Atmospheric Administration's (NOAA's) official ENSO indicator, which is based on a three-month running mean of sea surface temperature anomalies in the east-central tropical Pacific Ocean. Following NOAA's conventions, ENSO warm and cold events (El Niño and La Niña, respectively) are defined by ONI values meeting or exceeding threshold values of 0.5 and -0.5°C, respectively, for a minimum of five consecutive overlapping seasons. In this work, ENSO neutral conditions are defined as all seasons wherein the ONI value falls between -0.5 and 0.5°C; however, defining ENSO neutral conditions by ONI values between -0.3 and 0.3°C, in order to provide greater separation between the phases, has little impact on the results. These conventions applied to the ONI based on the Extended Reconstructed Sea Surface Temperature (ERSST) version 3b dataset (see Smith et al. 2008) results in 98, 108, and 201 overlapping three-month periods defined as El Niño, La Niña, and neutral, respectively. Additionally, the El Niño composites described in Section 2.3 include all qualifying periods, regardless of whether the period was more reflective of an eastern Pacific or a central Pacific (also known as Modoki) warm event (see Capotondi et al. 2015). Combining eastern and central Pacific warm events may subdue the possible ENSO-related signals in the El Niño composites; however, composites based on the El Niño subtypes are noisier than the combined composite due to the smaller number of periods in each composite.

2.2.1.3. Madden-Julian Oscillation

The strength and evolution of the MJO is indicated by the real-time multivariate MJO index (RMM), as developed by Wheeler and Hendon (2004). In this work, unless specified otherwise, an MJO phase event is retained in a phase composite analysis if the RMM indicates the same phase for at least four consecutive days and the amplitude of the index meets or exceeds an amplitude of 1.5 at least once during the phase event. The 1.5 amplitude threshold was selected to focus the analysis on only the strongest MJO phase events; however, reducing the threshold to one has little impact on the conclusions.

2.2.2. ARs Defined

2.2.2.1. Calculation of IVT

As discussed by other authors (e.g., Lavers et al. 2012; Gimeno et al. 2014), two different spatial fields are commonly used to detect ARs: some form of precipitable water and some form of integrated water vapor transport (IVT). In this work we define ARs in terms of IVT, also referred to as vertically-integrated moisture flux. We follow Lavers et al. (2012) and others and calculate the magnitude of IVT as:

$$IVT = \sqrt{\left(\frac{1}{g}\int_{1000}^{300} qu\ dp\right)^2 + \left(\frac{1}{g}\int_{1000}^{300} qv\ dp\right)^2},$$

where g is gravitational acceleration, q is specific humidity, u is zonal wind, v is meridional wind, and dp is the pressure difference between adjacent pressure levels. The mass-weighted vertical integration is performed using data from 1000 hPa to 300 hPa; however, the value of IVT is insensitive to the upper bound of the integral given the generally modest water vapor content of the upper troposphere.

The mean and first two harmonics of the IVT time series are removed at each grid point via fast Fourier transform in order to exclude the seasonal cycle and to create anomaly fields in which to detect AR-like features. The use of such anomalies removes the slowly-varying features, such as the semi-persistent tropical moisture reservoir, thus much of the potential for low-latitude AR "false positives" that may plague methods using full values of IVT. The use of anomalies also facilitates the use of a static 250 kg m^{-1} s^{-1} anomalous

IVT threshold within the detection algorithm that does not itself vary seasonally, but that actually varies spatially and temporally across the domain in terms of an equivalent full IVT detection threshold (see Figure A.1 in Appendix A). Adjusting the number of harmonics removed within reasonable bounds has little impact on the resulting instantaneous anomaly fields or the performance of the detection algorithm.

2.2.2.2. Identification of ARs

AR-like features, hereafter simply referred to loosely as ARs, are objectively identified within the fields of anomalous IVT via the automated detection algorithm described in Appendix A. We are certainly not the first to apply a detection algorithm to a reanalysis dataset to quantify ARs, but are motived to do so in order to further investigate AR dynamics and variability. We aim to explore ARs over the entire North Pacific and throughout the entire year, thus requiring a more generalized methodology compared to many previously developed algorithms. This algorithm takes an occurrence-based approach (i.e., one AR "hit" for each time step during which the requisite intensity and geometric criteria are met); therefore, each time step is scrutinized independently. As a result, the AR frequencies described in this work are calculated based on the number of periods during which an AR exists over a given grid point divided by the number of periods included in the composite. Similarly, the numbers of AR periods listed herein represent the total number of 6-hourly periods during which ARs were detected, not counts of independent AR events. Figure 2.1 depicts three example time steps during which ARs are identified by the algorithm, with the outlines of the detected features superimposed on fields of full IVT. Figure 2.1a shows an expansive summertime AR making landfall over the Alaska Panhandle, Figure 2.1b displays three less traditional ARs, and Figure 2.1c reveals a series of ARs that impacted the west coast of North America in December 2014. As described in Appendix A, running the detection algorithm over the entire 36-year period at 6-hourly resolution results in 81,409 retained features identified as ARs that have a center of mass within the North Pacific domain (10°–64°N and 123°–242°E), as defined by the map area of Figure 2.2. The total of 81,409 AR features equates to an average of approximately 1.5 features per 6-hourly time step. Again, the total number of AR features is a summation of occurrences detected within the 6-hourly time steps and should not be construed as analogous to independent ARs events.

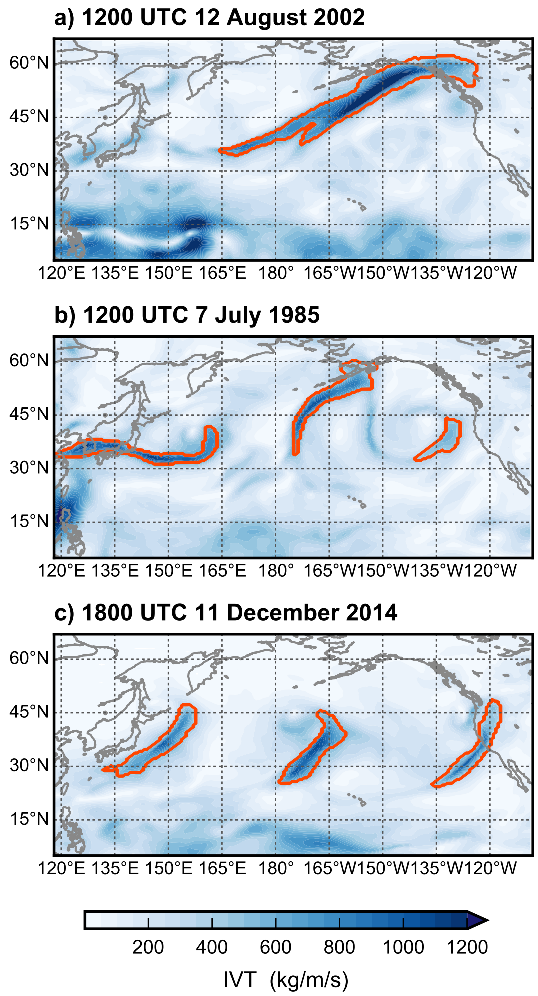

FIG. 2.1. Examples of detected AR-like features (outlined in red) within fields of instantaneous full-field IVT (shaded, in kg m^{-1} s^{-1}) for (a) 1200 UTC 12 August 2002, (b) 1200 UTC 7 July 1985, and (c) 1800 UTC 11 December 2014.

2.3. RESULTS

2.3.1. CLIMATOLOGY

The output from the detection algorithm affords a calculation of, among other things, an all-season climatology of AR frequency within the North Pacific domain, as displayed in Figure 2.2. The contouring in Figure 2.2 reveals a maximum frequency of just over 13% near 33°N and 168°E and frequencies in excess of 1% throughout the basin poleward of approximately 20°N. Interestingly, ARs identified via this methodology are found to be at least as frequent in places such as along the Aleutian Islands and near mainland Japan as they are along the U.S. West Coast. The frequency gradient that extends across the basin bracketing the Tropic of Cancer is robust to the method and appears to be tied to Rossby wave dynamics and the climatological northern extent of the Hadley circulation (not shown). The climatological depiction in Figure 2.2 resembles the North Pacific portion of the 2-year global climatology of ARs in Waliser et al. (2012). Differences between this climatology and those based on tropical moisture exports (e.g., Knippertz et al. 2013) may be due to our inclusion of AR-like features sustained by local moisture flux convergence and evaporation processes not exclusively tied to the transport of moisture from the tropics into the mid-latitudes. Though the actual frequency values plotted in Figure 2.2 are sensitive to the static thresholds within the detection algorithm, the spatial relationships are robust. This climatology provides useful reference values against which we will assess the impacts of seasonal and tropical variability on AR frequencies.

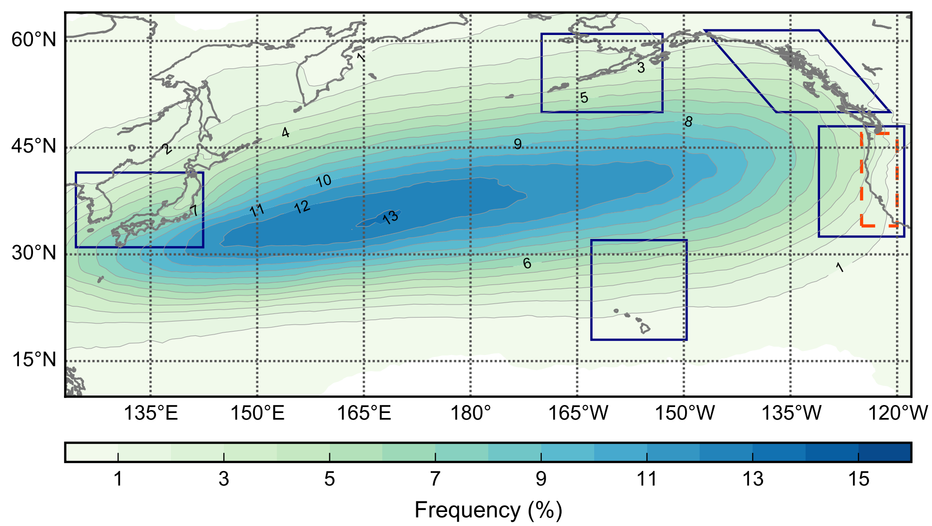

FIG. 2.2. All-season mean frequencies of AR occurrence over the North Pacific. The five blue boxes denote the locations that are used for in-depth, subregional analyses; the region identified by the dashed orange boundary is used to approximate U.S. West Coast landfalling events for Figure 2.3.

2.3.2. Seasonal Variability

The first class of variability we will explore is the seasonal cycle. As noted above, the majority of recently published work related to ARs in the North Pacific focused on some representation of an extended boreal winter season. Those same studies often concentrated only on ARs making landfall along the U.S. West Coast or some subdivision thereof. As shown in Figure 2.3, such a wintertime focus on landfalling features neglects sustained or even enhanced activity over the North Pacific during other seasons. The cyan curve represents the mean number of AR periods detected near the U.S. West Coast during overlapping three-month seasons, scaled to represent uniform 90-day seasons. ARs near the U.S. West Coast exhibit a pronounced seasonal cycle, with a minimum during boreal summer and a maximum during boreal winter. However, the gray curve representing the mean number of AR periods detected within the entire North Pacific domain does not display that same seasonality, suggesting that the seasonality of ARs varies by location within the domain. Moreover, the substantial separation between the curves in Figure 2.3 reveals the small proportion of ARs occurring near the U.S. West Coast compared to the basin-wide total. At times considered to be only rare or extreme events, analyses such as this emphasize that ARs are nearly ever-present contributors to the hydrological cycle on a basin-wide scale.

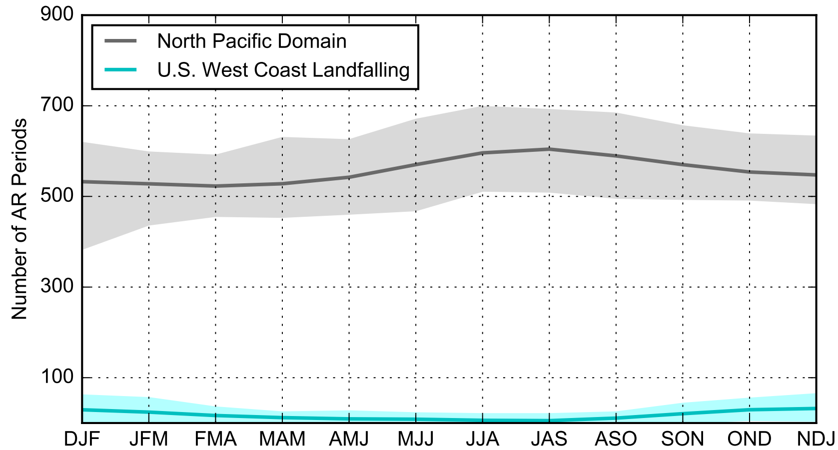

FIG. 2.3. Comparison between the mean number of AR periods within the entire North Pacific domain (10–64°N by 123–242°E) and within a subregion that encompasses much of the U.S. West Coast (identified by the dashed orange outline in Figure 2.2) by overlapping three-month seasons. The lines represent the seasonal mean over the 36-year record, while the shading highlights the range between the highest and lowest seasonal values. All seasons are scaled to represent uniform 90-day seasons.

While statements that ARs making landfall along the U.S. West Coast are most common during the boreal winter are supported by this analysis, the seasonality of AR frequencies varies strongly by region. To illustrate this point, Figure 2.4 displays the mean number of AR periods by overlapping three-month seasons for the five subregions outlined in Figure 2.2. These locations are not studied for their distinct depiction of AR variability per se, but rather for their potential societal importance. Regardless, differences among the locations' AR seasonal cycles are apparent in Figure 2.4. For example, the "Korea/Japan" subregion (gray curve), with a clear peak in AR occurrence in June–August (JJA), displays a seasonality nearly opposite to that of the U.S. West Coast. Additionally, a comparison of the "Southwest Alaska," "Coastal British Columbia," and "U.S. West Coast" mean numbers of AR periods (green, red, and amber curve, respectively) shows that the seasonal maximum AR occurrence shifts earlier in the year—toward the warm seasons—with an increase in latitude along the North American coast, similar to the behavior observed by Neiman et al. (2008b).

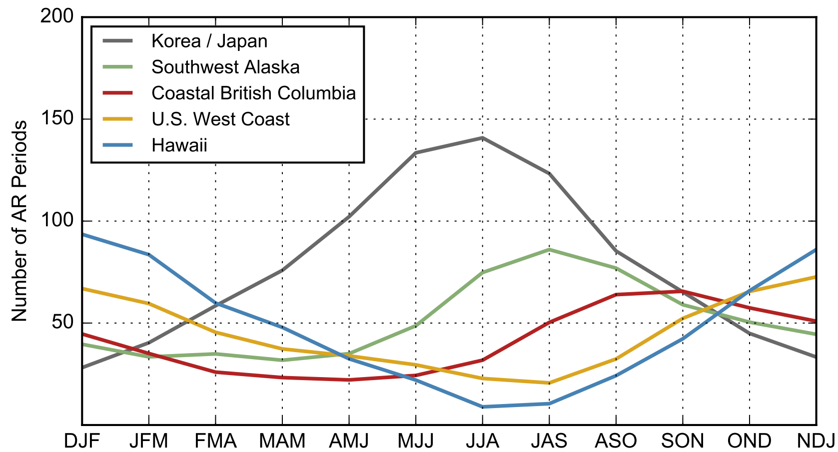

FIG. 2.4. As Figure 2.3, but of the mean number of AR periods for the subregions described in the text and depicted in Figure 2.2. Shading is omitted for clarity.

Taking a spatial, basin-wide perspective, Figure 2.5 reveals remarkable location-dependent changes in AR frequency with season, here represented as the difference between JJA or December–February (DJF) AR frequency and the all-season mean AR frequency. The nearly opposing patterns in the two panels of Figure 2.5 are more indicative of a spatial shift in AR incidence, rather than an overall seasonal increase or decrease in basin-wide AR occurrence. The depicted patterns of frequency difference are consistent with the previously-observed wintertime peak in AR frequencies along the U.S. West Coast and the seasonal contrast in that region suggested by Figures 2.3 and 2.4. The contrasting panels also capture the warm season increase in AR activity near Alaska mentioned earlier, out of phase with the seasonality observed near California and the Pacific Northwest. Seasonal differences in the range of 1–8% are not trivial considering that the maximum all-season AR frequency of occurrence is only approximately 13% in the heart of the domain, with most locations having a considerably lower mean AR frequency.

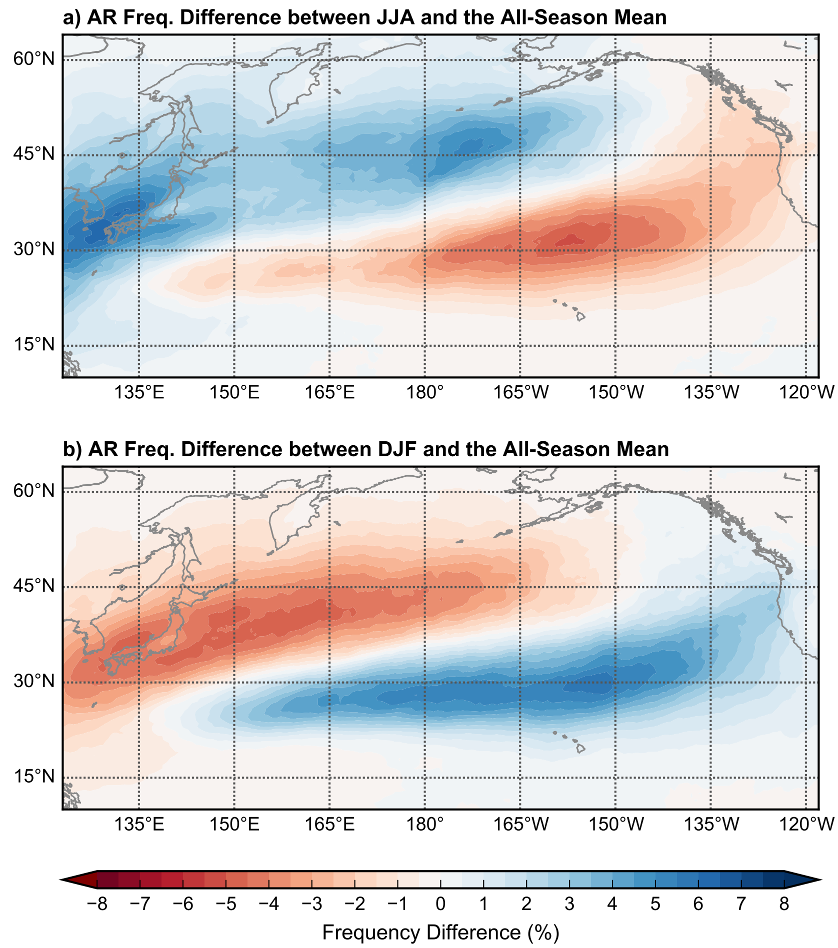

FIG. 2.5. AR frequency differences for (a) JJA and (b) DJF resulting from the subtraction of the all-season AR frequencies for the period 1979 to 2014 from the seasonal composite frequencies. Positive (blue) values indicate seasonal frequencies of occurrence higher than the annual mean, while negative (red) values indicate seasonal frequencies lower than the annual mean.

Figures 2.4 and 2.5 also begin to reveal the complexity of AR behavior near eastern Asia relative to other parts of the North Pacific domain, behavior previously documented by Knippertz and Wernli (2010) in terms of tropical moisture exports. The pronounced summertime peak in AR numbers in the "Korea/Japan" subregion in Figure 2.4 (gray curve) and the comparatively large positive values of frequency difference near Korea and Japan in Figure 2.5a relate to increased summertime activity in that region associated with the East Asian monsoon. A visual review of a subset of the detected summertime ARs in that region indicates an interesting mix of features, some not unlike the ARs detected elsewhere in the domain, while others appear as enhanced activity along the monsoonal Meiyu, Baiu, and/or Changma boundaries (see Sampe and Xie 2010, and references therein). The detection algorithm does filter out conventional tropical cyclones, but may retain AR-like features associated with transitioning/recurving tropical cyclones (e.g., Cordeira et al. 2013), tropical synoptic systems (e.g., Maloney and Dickinson 2003), and elongated regions of enhanced IVT along the semi-persistent monsoon boundaries. The far western Pacific/eastern Asia region is included in this work because of its importance in the lifecycle of the systems that support ARs elsewhere in the domain, and for societal reasons.

The latitudinal shift in frequencies apparent in Figure 2.5 may be associated with the well-documented seasonal migration of eddy activity along the eddy-driven jet (see Riehl et al. 1950, and others). Figure 2.6 compares the seasonal latitudinal migration of the eddy-driven jet with the mean position of maximum AR frequencies across the domain. Here, we follow standard practice and calculate the jet latitude by computing the latitude of the maximum low-level zonal mean zonal wind, vertically averaged from 925-700 hPa, within the North Pacific domain (e.g., Woollings et al. 2010). Similarly, the position of the maximum AR frequency is computed based on the latitudinal position of the maximum zonal mean AR frequency. In Figure 2.6 both the eddy-driven jet—used here as a proxy for eddy activity—and the AR frequency maximum are most poleward during boreal summer and most equatorward during boreal winter, suggesting a relationship between the position of the eddy-driven jet and AR activity in the North Pacific. Furthermore, the equatorward offset of maximum AR frequency compared to the jet position may be a result of Rossby wave breaking on the flank of the jet. As depicted in Figure 10g of Barnes and Polvani (2013), Rossby wave breaking preferentially occurs equatorward of the jet throughout the year. Here we find that the frequency maximum of ARs also preferentially occurs 10° equatorward of the seasonal mean eddy-driven jet position. The relationship between Rossby wave breaking and ARs is an area of ongoing research (e.g., Ryoo et al. 2013; Sodemann and Stohl 2013; Payne and Magnusdottir 2014), but ventures beyond the scope of this chapter.

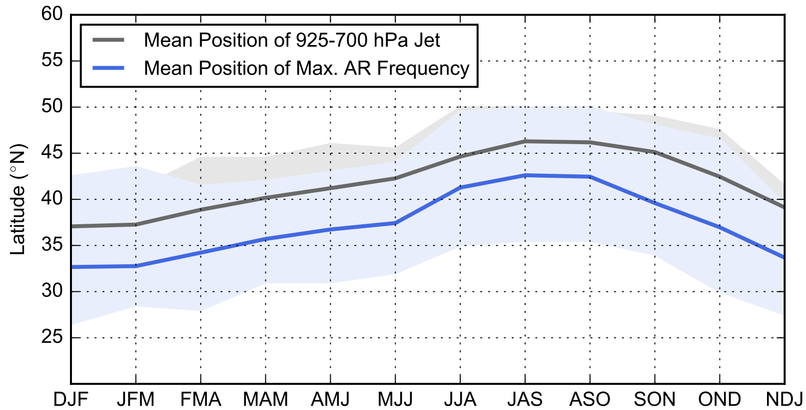

FIG. 2.6. Comparison of the latitudinal variation of the position of the eddy-driven jet stream and the position of the zonal mean maximum AR frequency by overlapping three-month seasons within the North Pacific domain. The shading highlights the range between the highest and lowest seasonal values for each variable.

2.3.3. Tropical Variability

The seasonal spread of the number of AR periods—indicated by the shaded regions in Figures 2.3 and 2.6—suggests a fair amount of variability, a significant portion of which may be influenced by tropical variability. While the background atmospheric conditions in the North Pacific may be more conducive to support tropical teleconnections during boreal winter (e.g., Horel and Wallace 1981), we evaluate possible connections between tropical variability and AR activity during all seasons. Though other well-documented modes of tropical variability exist, we focus our assessment here on the leading modes of interannual and intraseasonal variability, the ENSO cycle and the MJO, respectively.

2.3.3.1. El Niño-Southern Oscillation

Figure 2.7 shows frequency differences between ENSO phase composites and the all-season mean. The El Niño composite (Figure 2.7a) depicts the impacts of an enhanced and extended jet (e.g., Arkin 1982) on AR activity, with statistically significant (at 90% confidence level based on 1,000 bootstrap samples) positive anomalies along 30°N in the eastern Pacific and negative anomalies to the north along 45°N. In contrast, the enhanced activity extending from the central Pacific into the Gulf of Alaska in the La Niña composite (Figure 2.7b) is reminiscent of the previously observed poleward displacement of the storm track.

This pattern suggests that the displaced storm track shifts the extratropical cyclone activity, resulting in an overall poleward shift in AR occurrence. The ENSO neutral composite (Figure 2.7c) is reminiscent of the JJA seasonal AR frequency difference composite in Figure 2.5a, likely influenced by the disproportionate number of ENSO neutral periods occurring during warm seasons and the fact that El Niño and La Niña events tend to peak in amplitude during the winter half-year.

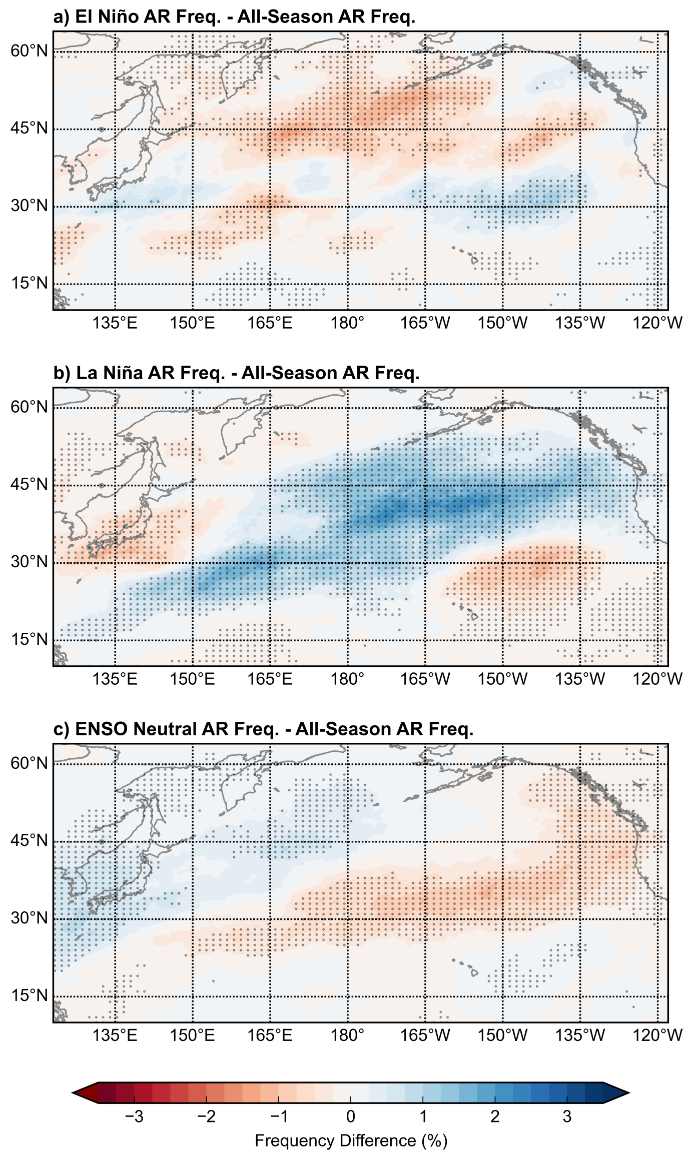

FIG. 2.7. As Figure 2.5, but comparing AR frequencies composited based on ONI values for (a) El Niño, (b) La Niña, and (c) ENSO neutral conditions with the annual mean AR frequencies removed. Stippled regions denote significance at the 90% confidence level based on 1,000 bootstrap samples.

Capturing the impacts of tropical variability on AR activity is complicated by the marked seasonality of ARs within the North Pacific domain shown earlier. Figure 2.8 displays the frequency differences between ENSO composites and the respective seasonal mean AR frequencies for two opposing seasons: JJA (left column) and DJF (right column). As presented, Figure 2.8 reveals that ENSO-related impacts vary by season. The classic El Niño and La Niña signals relating to the modification of the storm track and Rossby wave train response to ENSO-like heating (e.g., Hoerling and Kumar 2002) are most apparent in the enhanced AR frequency anomalies during the cool season (i.e., DJF). However, the large, statistically significant frequency differences during the warm season (i.e., JJA) suggest that ENSO may influence AR activity throughout the year. Also visible are the impacts of the seasonal cycle of AR frequencies on the seasonal ENSO phase composites; for example, the poleward enhancement of ARs during DJF La Niña periods is displaced farther poleward during JJA La Niña periods, likely due to the seasonal shift in the AR activity shown in Figure 2.6. Though the stippling indicates regions where the frequency differences are significant at the 90% confidence level, we confirmed that the majority of three-month periods within each composite display frequency anomalies of the same sign and similar distribution as those depicted in each of the panels, supporting the robustness of these spatial patterns of ENSO-related impacts.

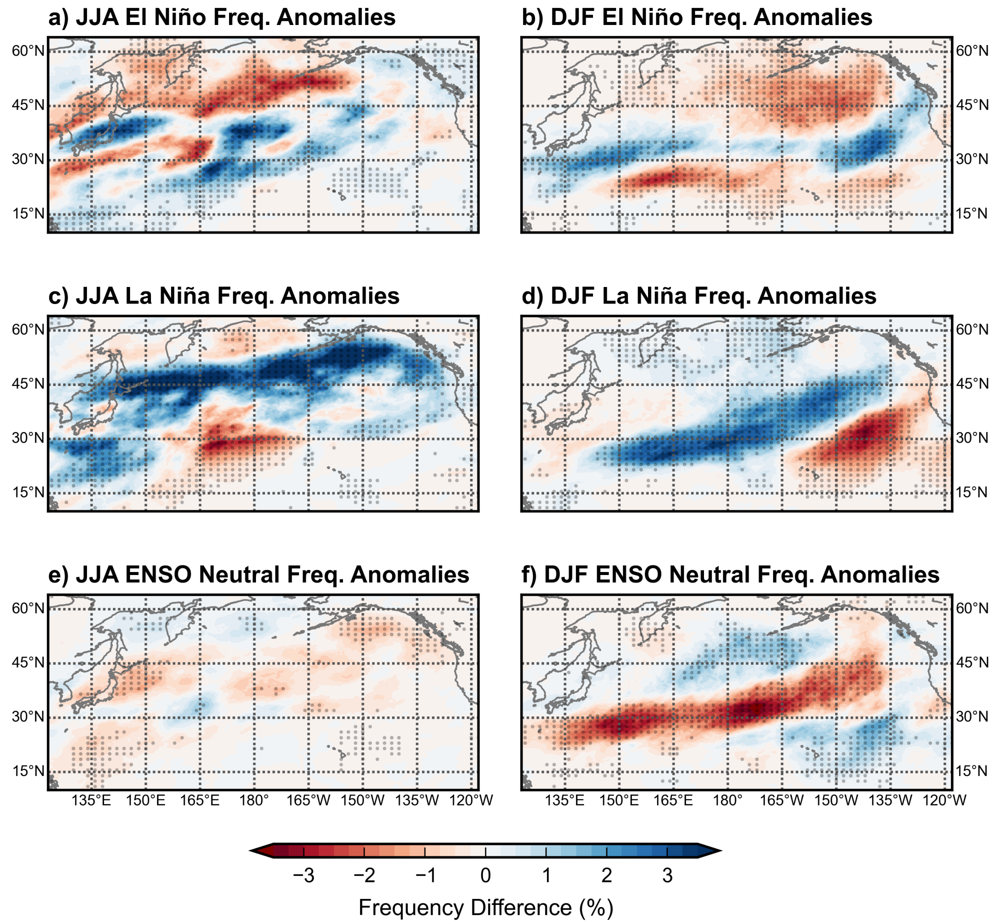

FIG. 2.8. As Figure 2.7, but comparing AR frequencies composited based on ONI values for (a–b) El Niño, (c–d) La Niña, and (e–f) ENSO neutral conditions with the seasonal mean AR frequencies removed for JJA (left column) and DJF (right column). Note that the range of values used for the colorfill is equivalent to that used in Figure 2.7, but different from the range displayed in Figures 2.5 and 2.10. Stippled regions denote significance at the 90% confidence level based on 1,000 bootstrap samples.

To further illustrate the impacts of the ENSO cycle and the seasonal cycle on AR occurrence, we return to the five subregions described earlier. Rather than presenting AR frequencies or frequency differences, we present the impacts of El Niño and La Niña on AR frequencies in Figure 2.9 in terms of the percent change relative to the local, seasonal mean AR frequencies. Here statistical significance is based on a *t* test comparing the seasonally-composited El Niño and La Niña values, with the degrees of freedom being the number of seasonal El Niño and La Niña events combined minus two. This representation of ENSO's impact on AR frequencies, in terms of percent change, varies based on location and season. Though not highlighted as being statistically significant by the t test—likely due to the limited reanalysis observational record—AR frequencies along the U.S. West Coast are increased during El Niño events, but only during winter months when ARs are climatologically most common. In contrast, El Niño conditions may actually reduce AR activity during summer months along the U.S. West Coast. Another feature that emerges is that the greatest impacts relating to ENSO variability do not always occur during boreal winter; indeed, several locations show peak changes of approximately 40% during the warm seasons (e.g., near Hawaii and along the coast of British Columbia). Also, El Niño and La Niña do not always have opposing impacts on a location; for example, during much of the summer half-year in the "Coastal British Columbia" subregion both El Niño and La Niña conditions increase AR activity above the seasonal norm (Figure 2.9c). Furthermore, in comparing ENSO's impacts on AR frequencies with the climatological seasonal cycle of the number of AR periods (e.g., the dashed brown lines in Figure 2.9), it emerges that ENSO variability can greatly alter the seasonal cycle. For example, the "Southwest Alaska" subregion (Figure 2.9b) sees an average of approximately 40 AR periods during the scaled 90-day FMA season. A local El Niño-related decrease of AR frequency of approximately 40% during that period could decrease that seasonal norm of 40 AR periods down to approximately 24 AR periods. In contrast, La Niña conditions stem a mean increase in AR activity, resulting in a mean of nearly 56 AR periods in that subregion during FMA.

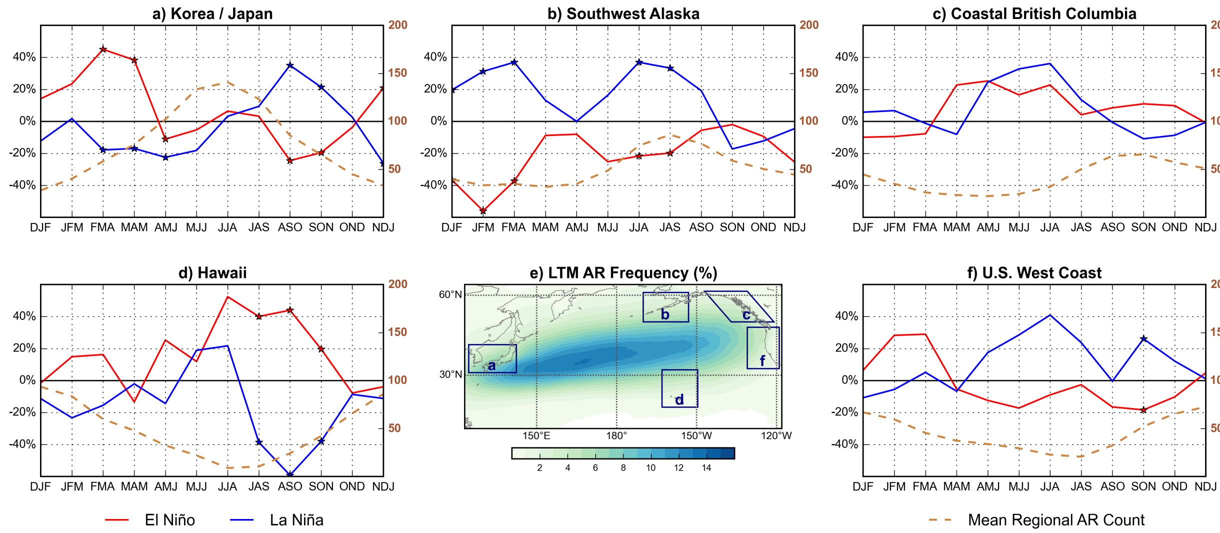

FIG. 2.9. Analyses of seasonal variability in terms of percent change in subregional AR frequency compared to the three-month seasonal mean for five locations identified in (e). For each location, lines representing El Niño (red) and La Niña (blue) conditions are plotted based on the legend and aligned with the vertical axis on the left-hand side of each subplot (ENSO neutral conditions are omitted for clarity). Also included in each subplot is a depiction of the seasonality of the mean number of AR periods within the location's bounds according to the vertical axis on the right-hand side of each subplot (dashed brown line). Stars indicate seasons where the percent change in AR frequency for El Niño periods is statistically significant from La Niña periods at the 90% confidence level based on a t test.

2.3.3.2. MADDEN-JULIAN OSCILLATION

Transitioning from ENSO's interannual scale to MJO's intraseasonal scale, we present Figure 2.10 with its eight RMM-based MJO phase composite AR frequencies, each with the all-season AR frequency removed. The panels in Figure 2.10 depict a somewhat progressive evolution of patterns of positive and negative values of frequency difference anomalies during an MJO lifecycle. Most pronounced are the higher frequencies of AR occurrence in the central and eastern Pacific during phases 7 and 8, when the anomalous convective activity associated with the MJO is transitioning from the Pacific to the Western Hemisphere. The increased AR activity depicted in the eastern Pacific during phases 6–8 may be linked to an enhanced eddy-driven jet resulting from the anomalous convection, with impacts similar to the El Niño composites but on a different time scale.

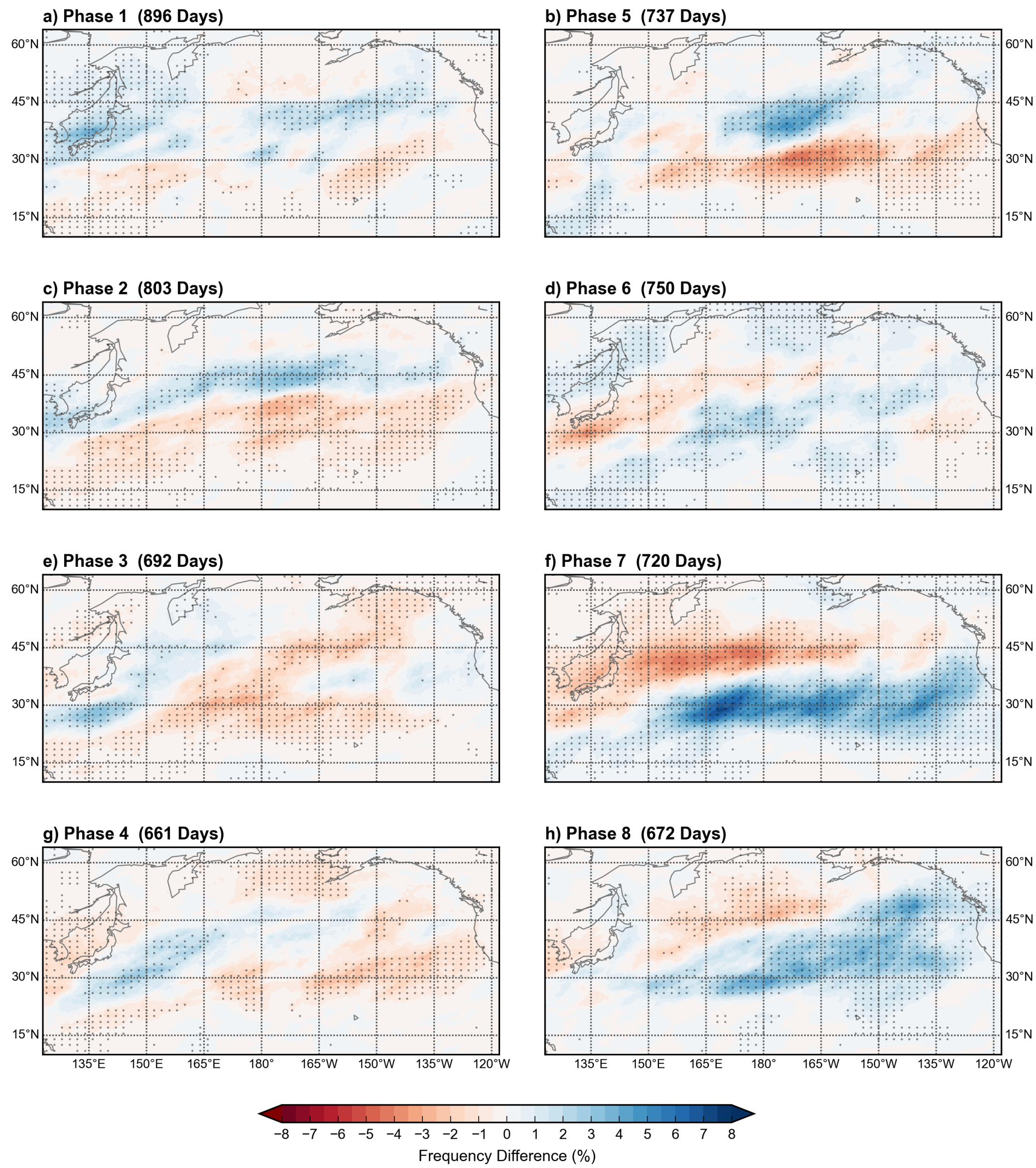

FIG. 2.10. As Figure 2.7, but for RMM-based MJO phase composites with the annual mean AR frequencies subtracted. As described in the text, only periods when the RMM index remained in the same phase for at least four consecutive days and during which at least one day had an RMM index amplitude greater than or equal to 1.5 are composited. Stippled regions denote significance at the 90% confidence level based on 1,000 bootstrap samples.

Figure 2.11 revisits the five subregions to further assess the MJO impacts on AR frequencies. The composited MJO impacts on AR frequency anomalies vary by location. For example, AR frequencies are reduced near Hawaii when the anomalous heating associated with the MJO is in the Indian Ocean (phases 2 and 3) and over the maritime continent (phases 4 and 5), then frequencies are enhanced as the active convection progresses from the western Pacific into the Western Hemisphere (phases 6–8). In contrast, AR frequency anomalies in the subregion encompassing much of Korea and Japan show a nearly opposite and weaker response to that of the subregion surrounding Hawaii. Though not as pronounced as the AR frequency impacts near Hawaii, Figure 2.11f indicates a reduction in ARs near the U.S. West Coast when the active phase of the MJO is near the maritime continent (phases 4 and 5) and an increase in ARs approaching the west coast of the U.S. when the MJO is in phases 7 and 8. The subplots displayed in Figure 2.11 are based on the average subregional AR frequency impact during MJO phase events compared to mean AR frequencies. An alternate approach comparing the number of AR "hits" within each subregion—like that used for the earlier AR period count plots—provides similar results (not shown).

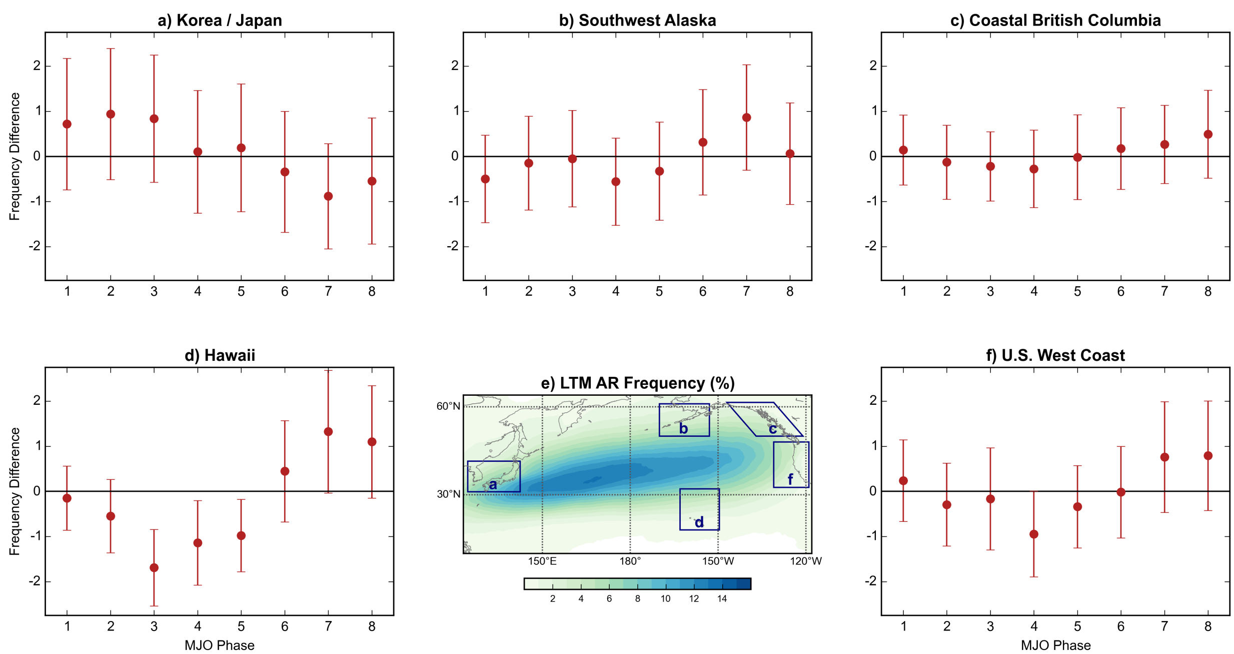

FIG. 2.11. MJO phase composite frequency anomalies by subregion as a function of MJO phase. Error bars encompass a 90% confidence interval based on the estimated standard error of sample proportions using the number of periods in each composited phase as the sample size.

We have shown that most locations have a pronounced seasonal cycle in AR frequencies and that seasonality matters when considering ENSO's impact on AR incidence; therefore, it is natural to wonder whether these all-season MJO composites are being muted by seasonality. Figure 2.12 depicts the percent change in

AR frequency (as in Figure 2.9) in paired MJO phase composites compared to the seasonal mean AR frequencies for the five subregions. Here the phases are paired (1 and 2, 3 and 4, and so on) to reduce the noise and increase plot clarity. This subregional analysis reveals how an all-season assessment of MJO-related impacts will subdue, if not completely mask, the seasonal impacts within a region. For example, the "Korea/Japan" subregion in Figure 2.11 displays a modest frequency response due to MJO forcing; however, Figure 2.12 reveals that the MJO activity may result in significant frequency changes of 25–50% during certain seasons (e.g., AR frequency increase in excess of 50% during DJF with MJO's active convection captured by RMM phase 1 and 2). Indeed, all five subregions show paired phase frequency responses of at least 50% during one or more seasons. As with ENSO-related variability, Figure 2.12 suggests that MJO-related variability has the potential to significantly counter or enhance low frequency variability like the seasonal cycle or ENSO background with respect to AR frequencies, but on a shorter time scale.

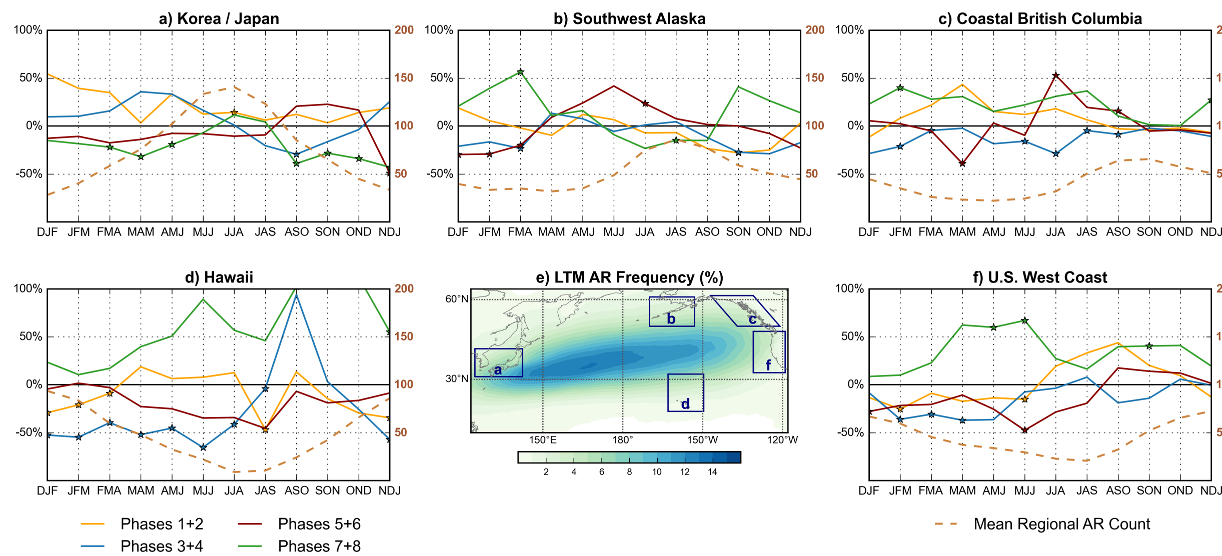

FIG. 2.12. As Figure 2.9, but for the percent change of paired seasonal MJO phase composite frequencies compared to three-month seasonal mean AR frequencies. Stars indicate season/phase combinations where the percent change in AR frequency from the seasonal mean AR frequency is statistically significant at the 90% confidence level based on a *t* test.

These MJO relationships are evaluated without a lag or lead separating the MJO event and the AR impacts. Depending on the location within the domain and dynamical mechanisms making the teleconnection, MJO-related forcing takes time, on the order of days to weeks (e.g., Hoskins and Karoly 1981; Matthews

2004; Branstator 2014), to evolve and communicate across the basin. However, the domain-wide view of this work complicates the evaluation of lagged response to MJO-like heating in such a manner, as the MJO response presumably takes differing lengths of time to impact different locations in the domain. Quantifying the lag/lead relationships and identifying the dynamical aspects of MJO-like heating that are most impactful to downstream AR relationships will remain for future work.

2.3.3.3. Variability Interactions

The results presented here suggest that variability due to ENSO and the MJO can compound or negate each other and have profound impacts on the occurrence of ARs in the North Pacific. Figure 2.13 examines the five subregions once again, but in terms of AR frequency anomalies within each region binned by ONI values—representing the state of ENSO—and RMM-based MJO phases. The binned, composited AR frequency anomaly values are standardized to more clearly reveal those ENSO/MJO combinations that result in changes in AR occurrence and to allow for a visual intercomparison of the subregions. Each panel is generated based on 845 independent high-amplitude MJO phase occurrences, each binned according to the coincident state of ENSO. Bins containing fewer than 10 phase occurrences are masked and hatched. Apparent from these two-dimensional histograms is that the combined ENSO/MJO relationships are complicated and vary based on location. For example, AR activity near Hawaii appears more dominated by MJO variability (left-to-right contrast in Figure 2.13d) than ENSO variability (top-to-bottom contrast) in this all-season analysis, with the frequency of ARs being enhanced when MJO-like heating is over the western Pacific and transitioning into the Western Hemisphere (phases 6–8). In contrast, the "Coastal British Columbia" subregion generally shows enhanced AR activity (green shading) more preferentially during La Niña periods, while reduced AR activity (red shading) is more common during El Niño events. The complicated—perhaps even noisy—appearance of the subplots in Figure 2.13 is not unexpected, due to the anticipated complex interactions between modes of tropical variability. This may be especially true for these particular subregions—each chosen for their potential societal importance, not for their representation of AR variability—well removed from the high AR frequencies of the central North Pacific. Hence, more coherent anomaly patterns can be expected for subregions positioned over oceanic locations with more frequent AR activity.

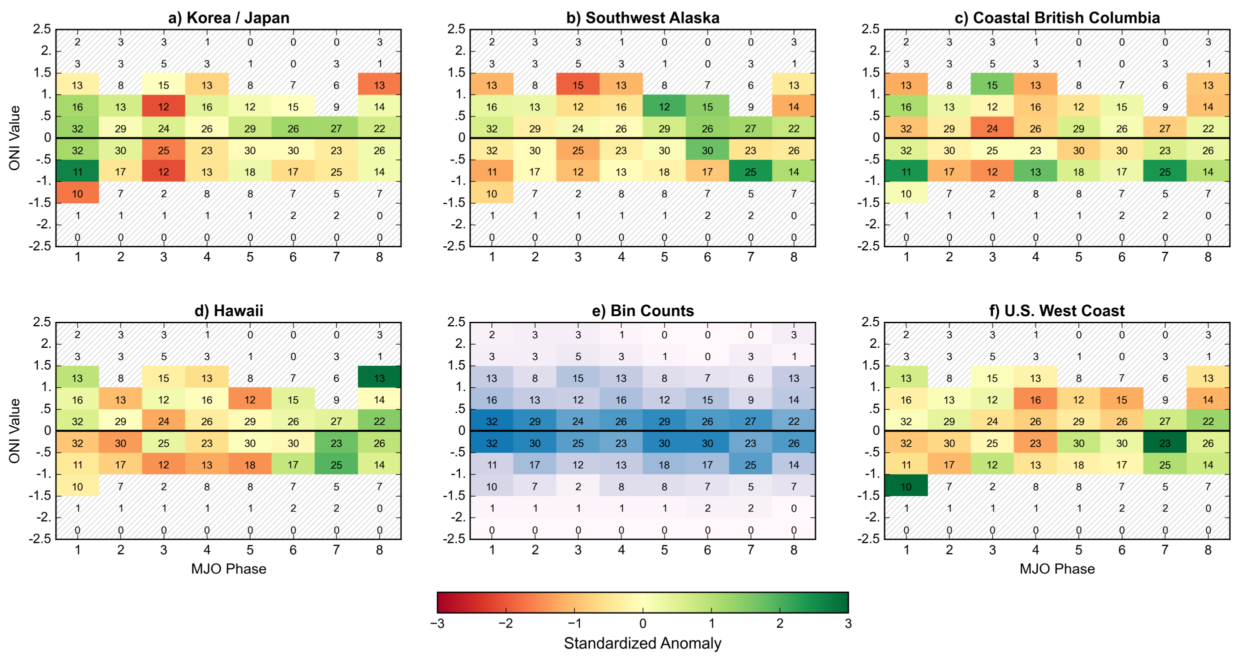

FIG. 2.13. Two-dimensional histograms of AR frequencies arranged by binned ONI values (°C) vs. RMM-based MJO phase for the five subregions depicted in Figure 2.2. The number of independent MJO phase occurrence/ONI value pairs in each bin are shown and shaded in panel (e) and repeated as the numeric overlay in each of the panels. The AR frequency difference values are standardized for each region and represented by the bin colorfill according to the colorbar; bins with fewer than 10 unique phase occurrences are masked and hatched.

2.4. DISCUSSION AND CONCLUSIONS

An automated detection algorithm is used to objectively identify ARs within 36 years of gridded reanalysis data. The resulting output allows for a compositing approach to investigate how the seasonal cycle and climate variability influence ARs over the North Pacific in the reanalysis record. Here we focus on the all-season climatology of ARs over the North Pacific, as well as the impacts of three forms of variability on AR frequencies of occurrence: seasonal cycle, ENSO, and MJO, as well as their interactions.

ARs exist throughout the year within the North Pacific domain, but a clear seasonality exists in the spatial distribution of AR frequency. This seasonal cycle of AR activity manifests itself more as a displacement of ARs toward the north and west during the warm seasons—in association with the seasonal migration of the eddy-driven jet—than it does in a marked change in the total number of ARs that occur within the North Pacific region.

Studies that focus only on some representation of the boreal winter season may provide incomplete assessments of ARs and their impacts across the Pacific. In particular, such focused work may miss important warm season AR contributions to the general circulation and/or hydrologic cycle, especially for domains that extend beyond the U.S. West Coast. This issue may be particularly critical when investigating potential future changes in AR frequency and/or behavior, as examinations within limited temporal or spatial domains may mask shifts in the seasonal cycle or preferred locations of ARs. Additionally, statements regarding the seasonality of ARs must clearly specify the location(s) for which such statements apply, as the claims in current literature that more ARs occur during the winter half-year (e.g., Gimeno et al. 2014; Payne and Magnusdottir 2014) only hold true in specific subregions (such as near Hawaii and along the west coast of the contiguous U.S.).

Furthermore, the composite analyses undertaken here suggest a complex interaction between classes of variability and their impact on ARs. Changes to the seasonally varying North Pacific mean state due to the leading forms of interannual and intraseasonal tropical variability can enhance or offset the pronounced seasonal cycle and/or each other by forcing local changes upwards of +/- 40–50% of the seasonal mean AR frequency of occurrence. As ENSO and the MJO can both modify the eddy-driven jet position and strength over the North Pacific, both are shown to impact the displacement and occurrence of ARs in a way not unlike the seasonal cycle, but on different time scales. This exploration into the large-scale variability of ARs in the North Pacific is not all-inclusive; indeed, one could imagine composites based on other characterizations of variability (e.g., Arctic Oscillation, Pacific-North American teleconnection) beyond those presented here.

Recently published work by Guan and Waliser (2015) largely corroborates the results of this investigation. They developed and documented an AR detection algorithm based on full-field IVT calculated from the ECMWF Interim reanalysis and using an 85th percentile detection threshold specific to each season and grid cell. Their depictions of global AR climatology and variability are similar to the North Pacific plots shown herein, especially after adjusting for differences in the period of record (18 years compared to the 36 years used in this work), composite periods, and colorbar conventions (not shown). This comparison lends credence to the robustness of both works' conclusions, despite the differences in detection methods and underlying datasets.

As ARs bridge weather and climate scales, this work addresses the climatology and variability in terms of actual AR occurrences versus a more general approach of investigating total or filtered fields of water vapor transport employed by others (e.g., Newman et al. 2012; Kim and Alexander 2015). We postulate that our identified relationships between climate variability and water vapor transport would be similar even if some moisture flux variable or field was composited; however, this feature-based approach affords a more detailed observational examination and impact assessment of these weather-makers not afforded by a filtering or field approach.

Whether the likelihood of AR occurrence is altered by seasonality or tropical variability, AR impacts on day-to-day weather and seasonal climate anomalies are where these features matter most to forecasters, resource managers, and the regional population. As shown, location and the state of the climate system matter when considering frequencies of AR occurrence and their potential impacts. As a result, the well-posed arguments made regarding the importance of considering wintertime landfalling ARs along the U.S. West Coast (heightened flood risk, hydrological budgeting, etc.) in earlier works (e.g., Ralph et al. 2006; Dettinger et al. 2011; Warner et al. 2012; Dettinger 2013) may also be applied to other subregions of interest, although the season and climate background state require consideration.

CHAPTER 3

MODULATION OF ATMOSPHERIC RIVERS BY NORTHEAST PACIFIC HEIGHT ANOMALIES[2]

3.1. INTRODUCTION

Atmospheric rivers (ARs) are filamentary plumes of focused tropospheric water vapor transport that dominate the flux of water vapor into and within the extratropics (e.g., Zhu and Newell 1998; Ralph et al. 2004; Neiman et al. 2008b). Landfalling ARs may trigger weather extremes such as heavy rainfall and localized flooding (e.g., Ralph et al. 2006; Neiman et al. 2008a; Smith et al. 2010; Neiman et al. 2011; Ralph and Dettinger 2012; Warner et al. 2012), and influence periods of regional drought and/or precipitation abundance (e.g., Neiman et al. 2008b; Guan et al. 2012a; Dettinger et al. 2011; Dettinger 2013). Perhaps due to these wide-ranging impacts, ARs affecting the western coastline of the contiguous United States (U.S.) have been extensively studied (see Rutz et al. 2014; Payne and Magnusdottir 2014; Jackson et al. 2016, and references therein).

In contrast to ARs making landfall along the U.S. West Coast, high-latitude ARs in the Pacific basin have received comparatively little attention. The most comprehensive work available addressing ARs near Alaska, for example, is a National Oceanic and Atmospheric Administration (NOAA) National Weather Service (NWS) internal paper on heavy precipitation and flooding in Alaska (Papineau and Holloway 2011). That paper concluded that the majority of the surveyed rain-generated flooding events in Alaska resulted from landfalling ARs.

Peer-reviewed literature provides background regarding the latitudinal variability of AR characteristics (Ralph et al. 2004) and the composite synoptic-scale signatures of ARs near western North America (Neiman et al. 2008b; Roberge et al. 2009); however, such studies do not address the high-latitude ARs that will be evaluated in this work. Recently, Guan and Waliser (2015) provided a global climatology of ARs

[2] Mundhenk, B. D., E. A. Barnes, E. D. Maloney, and K. M. Nardi, 2016: Modulation of atmospheric rivers near Alaska and the U.S. West Coast by northeast Pacific height anomalies. *J. Geophys. Res. Atmos.*, **121**, 12751–12765, doi:10.1002/2016JD025350. © American Geophysical Union. Used with permission.

that included an assessment of the landfall frequency, seasonality, and variability of ARs from 18 years of reanalysis data. Mundhenk et al. (2016a) also evaluated the climatology and variability of ARs, but focused on the North Pacific basin and included a brief analysis of a subregion extending over southwestern Alaska. Brands et al. (2016) calculated boreal wintertime AR counts through the twentieth century in four reanalysis datasets for five regions along the North American west coast that included two regions bordering the Gulf of Alaska. They corroborated Guan and Waliser (2015) who found AR activity along much of western coastline is correlated with the Pacific-North American teleconnection pattern, though the significance of the relationship varied based on the season and particular reanalysis dataset. Brands et al. (2016) also found seasonal AR counts near British Columbia and the Gulf of Alaska to be correlated with the strength of the climatological Aleutian low. None of these works methodically explored the atmospheric dynamics associated with high-latitude ARs over the North Pacific, and so we address this knowledge gap in sections 3.3–3.5 of this dissertation.

Recent research into the dynamics supporting poleward moisture fluxes into the Arctic provides a framework for our research in terms of actual ARs and their connection with the large-scale dynamics of the North Pacific. For example, Woods et al. (2013) investigated the broad circulation patterns associated with wintertime transport of moisture across 70°N. They found that the most intense moisture intrusions into the Arctic occur when high pressure is positioned over the eastern Pacific. Liu and Barnes (2015) advanced the analysis of Woods et al. (2013) by documenting the link between synoptic-scale moisture transport into the Arctic across 60°N and Rossby wave breaking. They found that a substantial fraction of the extreme moisture intrusions into the Arctic are closely related to Rossby wave breaking. More recently, Woods and Caballero (2016) corroborated these and other works relating poleward moisture flux into the Arctic with mid-latitude dynamics and variability. Motivated by these studies, we will examine the relationship between ARs and Rossby wave breaking in section 3.5.

Despite the limited mention of high-latitude ARs in the literature, they constitute a worthy and timely topic of investigation. Not only do high-latitude ARs cause notable impacts upon landfall (Papineau and

Holloway 2011, 2012), but AR-like features may also be responsible for the majority of the moisture flux into the Arctic (e.g., Woods et al. 2013; Liu and Barnes 2015; Dufour et al. 2016) and may contribute to the Arctic amplification (e.g., Woods and Caballero 2016). Understanding these features and their resulting radiative effects and precipitation impacts is important for characterizing the climatology and variability of weather and climate at high latitudes.

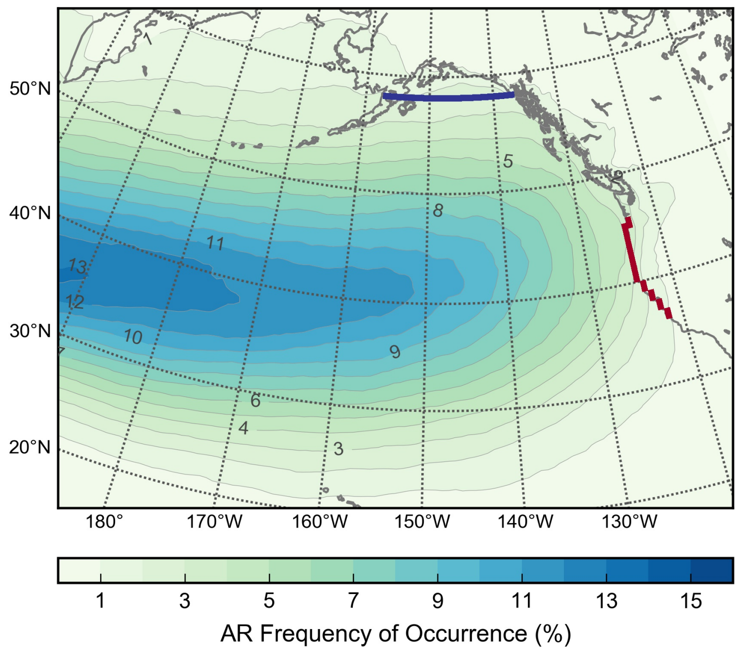

FIG. 3.1. Location of the Gulf of Alaska (blue) and U.S. West Coast (red) landfall boundaries overlaying the annual mean AR frequency of occurrence (contoured shading).

In this work, we will analyze ARs that pass over the two distinct boundaries approximating landfall plotted in Figure 3.1, referred to as "Gulf of Alaska" (blue) and "U.S. West Coast" (red). The purpose of this study is threefold: (1) to compare and contrast the occurrence and attributes of ARs near southern Alaska with the comparatively well-documented ARs near the U.S. West Coast, (2) to assess the common meteorological conditions associated with these ARs and the differences between them, and (3) to investigate the large-scale atmospheric dynamics that may explain the variability of AR activity at synoptic, subseasonal, and interannual time scales.

The remainder of this chapter is organized into five sections. Section 3.2 includes a brief description of the datasets and methods used in this work. Section 3.3 compares and contrasts the occurrence and attributes of ARs over the two landfall boundaries. Section 3.4 assesses the relationship between the large-scale atmospheric conditions and AR activity at the synoptic, subseasonal, and interannual time scales. Section 3.5 explores the related dynamics. Finally, the chapter's results are concluded in section 3.6.

3.2. DATA AND METHODS

3.2.1. ATMOSPHERIC VARIABLES

The National Aeronautics and Space Administration (NASA) Modern-Era Retrospective Analysis for Research and Applications (MERRA) reanalysis dataset (Rienecker et al. 2011) is the source for all of the atmospheric variables analyzed in this work. Unless specified otherwise, thirty-seven years (1979–2015) of instantaneous data at 6-hourly temporal resolution and native spatial resolution ($\frac{1}{2}^\circ$ latitude $\times$ $\frac{2}{3}^\circ$ longitude) on isobaric surfaces are used.

3.2.2. ATMOSPHERIC RIVERS

ARs are objectively identified using the detection algorithm described in Mundhenk et al. (2016a). The algorithm uses fields of positive anomalous, instantaneous vertically-integrated water vapor transport (IVT′), calculated from MERRA reanalysis data spanning 1000 to 300 hPa, together with a series of intensity and geometric (e.g., total area, length, length-to-width ratio) criteria, to detect AR-like features. As noted in Mundhenk et al. (2016a), the use of anomalies aids automated feature detection in large spatial domains and across all seasons and allows for the use of a static 250 kg m^{-1} s^{-1} IVT′ threshold within the detection scheme. Although the actual detection threshold does not vary in the algorithm, the comparable, or equivalent, full IVT threshold (i.e., mean and seasonal cycle *not* removed) varies spatially and temporally, as evidenced by Figure 3.2. The detection threshold, shown by the dashed orange curves, follows the seasonal cycle of IVT in both regions and appears suitable for the year-round detection of ARs for both of the landfall boundaries in this analysis. Furthermore, the 250 kg m^{-1} s^{-1} IVT′ threshold should not be considered as equivalent to a 250 kg m^{-1} s^{-1} threshold for full IVT that one may encounter in other detection schemes (e.g., Rutz et al. 2014; Radić et al. 2015).

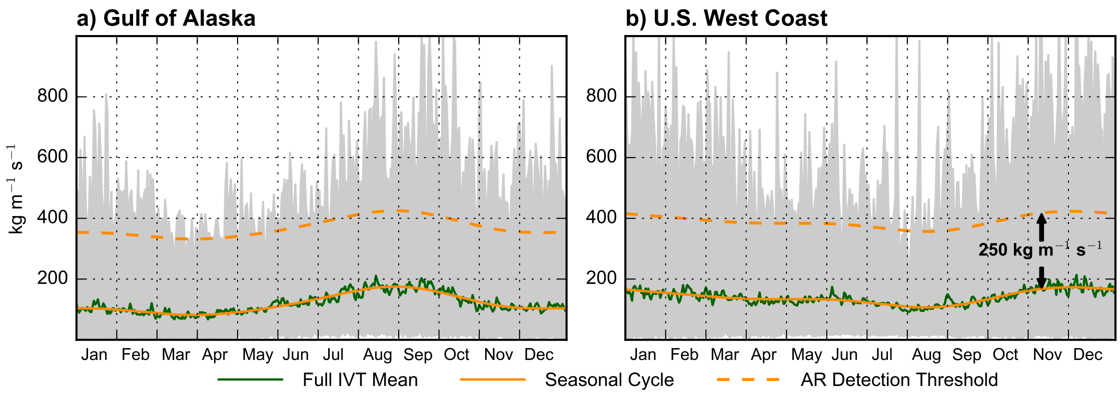

FIG. 3.2. Comparison of IVT values and the AR detection threshold along the (a) Gulf of Alaska and (b) U.S. West Coast landfall boundaries. In each panel, the seasonal cycle of IVT (solid orange curve) and the AR detection threshold (dashed orange curve) overlay the daily maximum/minimum range of IVT values from the 37-year record (gray shading) and the daily mean IVT (solid green curve).

The AR detection algorithm employs an occurrence-based approach (i.e., one AR "hit" for each 6-hour period during which the criteria are met). As a result, the AR frequencies described herein are calculated based on the number of 6-hourly periods during which an AR exists over a given grid point or landfall boundary divided by the number of 6-hour periods included in the composite. For example, Figure 3.1 shows the landfall boundaries overlaying the annual mean AR frequency of occurrence (ARF; shading) based on Mundhenk et al. (2016a), updated to encompass the available 37-year MERRA record. Besides AR frequencies based on 6-hour periods, ARs are also expressed in terms of unique events (i.e., one "hit" per feature lifecycle), defined as the consecutive periods during which an AR is detected over a landfall boundary.

The boundaries approximating landfall shown in Figure 3.1 are each roughly 1200 km in length in order to facilitate the comparison of ARs near both locations. The number of AR periods is a function of the length of these landfall boundaries, increasing as the boundary length increases. The separation between the boundaries is deliberate in order to reduce the number of AR events that simultaneously impact both locations, while still representing regions of potential societal importance. Also, ARs need only graze a landfall boundary to be considered landfalling and included in these analyses. Though these boundaries are referred to as landfall boundaries, ARs are not restricted based on the angle of incidence. Although the nearly linear boundaries are oriented orthogonally, the results are similar if the boundaries are replaced with rectangular regions of equal area. In general, the results presented in this work are insensitive to small changes in the position and orientation of the landfall boundaries.

3.2.3. Atmospheric River Attributes

In addition to the location, date, and time of occurrence of each AR, the detection algorithm also quantifies specific attributes of each AR. Attributes assessed in this work include:

(1) Persistence: approximate length of time, in hours, a unique AR event remains over a landfall boundary

(2) Length: approximate length, in kilometers, of an AR

(3) Area: approximate area, in square kilometers, of the region enclosed by an AR using the 250 kg m^{-1} s^{-1} IVT′ threshold

(4) Low-level zonal wind (u wind): mean of the layer averaged (1000–925 hPa) zonal wind within an AR

(5) Low-level meridional wind (v wind): mean of the layer averaged (1000–925 hPa) meridional wind within an AR

(6) Orientation: inclination of the mean low-level flow within an AR, in degrees, counterclockwise off the horizontal (e.g., 0° is due east, 90° is due north)

(7) Integrated water vapor transport (IVT): mean mass-weighted vertical integral of water vapor flux from 1000–300 hPa within an AR

(8) Integrated water vapor transport anomaly (IVT′): mean IVT, after the annual mean and seasonal cycle (calculated here as the first two harmonics of the annual climatology) have been removed via fast Fourier transform, within an AR

(9) Precipitable water (PWAT): mean mass-weighted vertical integral of tropospheric water vapor from 1000–300 hPa within an AR, also known as total precipitable water, total column water vapor, and/or integrated water vapor

3.2.4. Rossby Wave Breaking Events

In order to associate AR events and height anomalies with Rossby wave breaking (RWB) activity in section 3.5, we draw upon the output of the Rossby wave identification algorithm of Liu et al. (2014a). This algorithm is based on Strong and Magnusdottir (2008) and is also used and further described in Liu and Barnes (2015). Liu et al. (2014a) interpolate 6-hourly MERRA potential temperature values ranging from 300K to 350K, at an interval of 5K, onto the 2 potential vorticity unit (PVU) surface. If any of the potential temperature contours overturn and enclose an area of more than 25° on an equirectangular projection, an RWB event is identified and classified as either anticyclonic wave breaking (AWB) or cyclonic wave breaking (CWB) according to the direction of the overturning. Algorithm output is available for 1979–2010 at 6-hourly resolution. RWB climatologies based on this dataset are available in the supporting information accompanying Mundhenk et al. (2016b).

For the results presented in Section 3.5, the proximity of AR events to RWB activity is evaluated in both space and time. For each period during which a unique AR is detected over the respective boundary, the spatial extent of the AR is used to determine if the AR overlaps with a breaking region identified by the RWB detection scheme (that defined by the overturning potential temperature contours) during the same period. If an overlap is detected, the period is characterized by the amount of overlap and direction of the detected wave breaking. If no overlap is found, an additional check extends the AR extent by approximately 3° in all directions and repeats the test. The AR event is then classified based on the direction of the wave breaking occurring most often and with the greatest spatial overlap, giving preference to the overlap.

3.3. OCCURRENCE AND ATTRIBUTES OF ATMOSPHERIC RIVERS

3.3.1. Atmospheric River Occurrences

We begin by assessing the existence of ARs over the landfall boundaries. Figure 3.3 reveals the presence of ARs within the 37-year reanalysis record over both boundaries as a function of overlapping three-month seasons. ARs occur over both boundaries during each season; however, both locations display a pronounced seasonality in terms of the mean number of unique AR events (dotted curves; right ordinate), as well sizable interannual variability in the seasonal number of AR events (shading). The wintertime peak in AR activity along the U.S. West Coast is well documented (e.g., Neiman et al. 2008a). The shift in peak AR activity toward the Northern Hemisphere warm seasons at higher latitudes is also known (e.g., Neiman et al. 2008b; Mundhenk et al. 2016a), and relates to the seasonal migration of the eddy-driven jet (Mundhenk et al. 2016a).

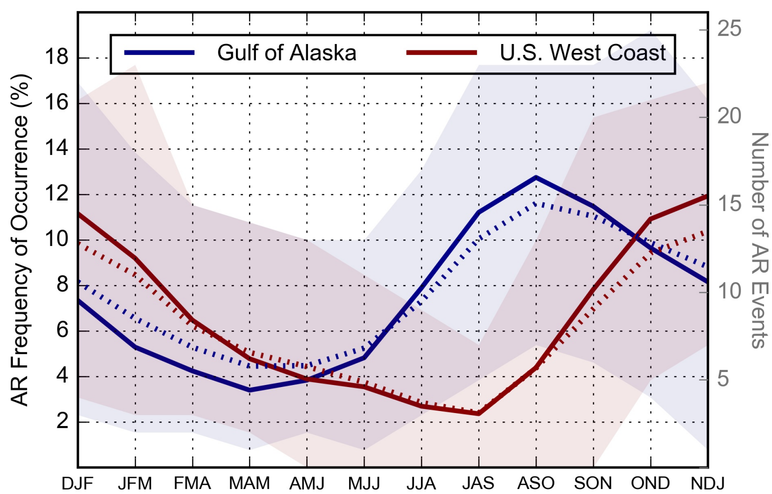

FIG. 3.3. Seasonality of AR frequency of occurrence (solid curves; left ordinate) and the average number AR events (dotted curves; right ordinate) by overlapping three-month seasons, each scaled to represent a uniform 90-day season, for the Gulf of Alaska (blue) and the U.S. West Coast (red) landfall boundaries. Shading highlights the range between the highest and lowest seasonal counts of AR events.

Figure 3.3 also depicts AR activity over the landfall boundaries in terms of frequency of occurrence (solid curves; left ordinate). Recall from section 3.2.2 that AR frequencies are based on the number of periods with an AR over a given landfall boundary divided by the total number of periods in each season, while the number of AR events consider the consecutive periods an AR exists over a boundary as one single event. The pronounced seasonality remains, with the AR frequencies peaking at nearly 12.7% for the Gulf of Alaska in August–October (ASO) and 11.9% for the U.S. West Coast in November–January (NDJ). Despite the difference in the AR seasonal cycle over the two landfall boundaries, the annual mean AR frequencies of 7.5% and 6.6%, for the Gulf of Alaska and U.S. West Coast respectively, are comparable. As the seasonality of ARs along the west coast of North America is roughly a function of latitude, one may expect shifts in the curves in Figure 3.3 if the boundaries are adjusted meridionally.

3.3.2. Composite Atmospheric Conditions

Figure 3.4 displays the composite atmospheric conditions for 383 unique AR events that passed over the Gulf of Alaska landfall boundary during December–February (DJF). DJF falls within the well-documented winter season for ARs along the U.S. West Coast, and thus facilitates comparisons with findings from other studies. While the results throughout this section are discussed in terms of DJF and/or annual values, the majority of the relationships are not unique to a particular season and exist throughout the year.

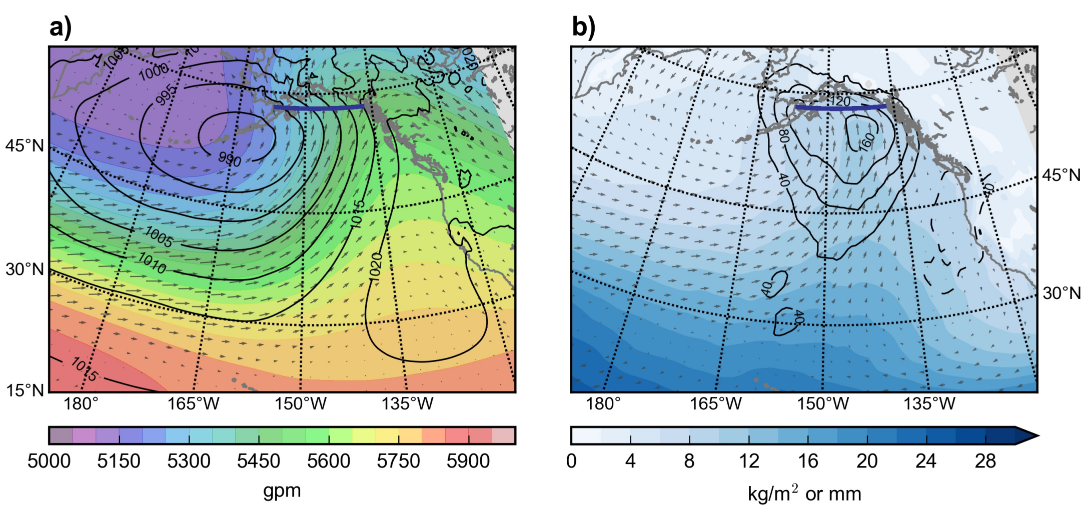

Fig. 3.4. Atmospheric conditions composited on the first period of the 383 unique DJF Gulf of Alaska AR events (blue demarcation). Panel (a) includes 500 hPa geopotential height (shading; intervals of 50 geopotential meters (gpm)), sea level pressure (black contours; intervals of 5 hPa), and 700 hPa vector winds (arrows). Panel (b) shows total precipitable water (shading; intervals of 2 mm), integrated water vapor transport anomalies (black contours; intervals of 40 kg m^{-1} s^{-1} with the zero contour omitted), and mean 1000-925 hPa winds (arrows).

The composite conditions in Figure 3.4 are based only on the first period from each AR event in order to best capture the conditions characteristic of initial landfall. Figure 3.4a shows a pronounced low pressure system (contours) over the eastern Aleutian Islands. To the east, amplified 500 hPa ridging (shading) roughly aligns with the west coast of the North American continent. The resulting gradient between these features supports the abrupt transition from nearly zonal flow at 700 hPa over the central Pacific to meridional flow toward the landfall boundary (arrows). Figure 3.4b shows a tongue of high total precipitable water (shading) extending towards southern Alaska coincident with strong low-level winds (arrows) and, therefore, a region of anomalous IVT (contours) encompassing the Gulf of Alaska landfall boundary. These characteristics are even more pronounced in composites where each AR's landfall position is shifted to a common longitude (not shown), confirming that the patterns in Figure 3.4 are smeared by variability along the 1200 km boundary. In their survey of subjectively selected rain and flooding events, Papineau and Holloway (2011) also found this general pattern of enhanced ridging over the far eastern Pacific and a broad, elongated low over the eastern Aleutians to be common among heavy rain events along the southern coast of Alaska.

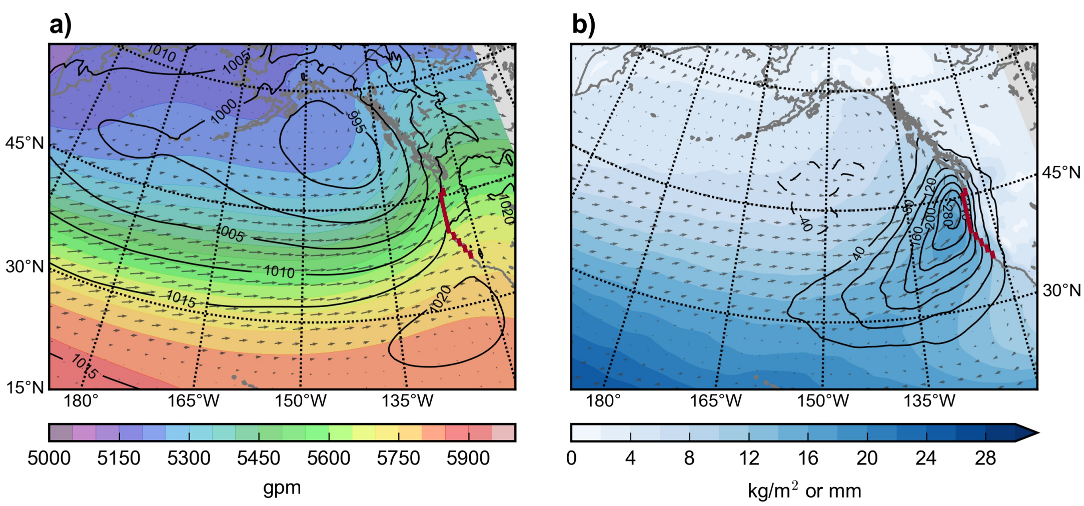

FIG. 3.5. As in Figure 3.4, but for composite first-period atmospheric conditions during 461 DJF U.S. West Coast AR events identified using the indicated landfall boundary (red demarcation).

Figure 3.5 depicts the atmospheric conditions composited from 461 first-period DJF U.S. West Coast AR events. A broad region of low pressure extends across the Gulf of Alaska and northeast Pacific in this composite. The pronounced 500 hPa ridging apparent in the Alaska composite (Figure 3.4a) is much weaker and farther inland in this U.S. West Coast AR analysis (Figure 3.5a). The flow at 700 hPa and at lower levels is predominantly zonal, with a subtle meridional perturbation just off shore of the west coast. Just as in the Gulf of Alaska AR composite, here a tongue of high total precipitable water extends from the semi-persistent tropical moisture reservoir toward the landfall boundary (Figure 3.5b). The general composite conditions apparent in Figures 3.4 and 3.5 appear not only in these first-period composites, but also in composites of conditions prior to landfall (not shown). This suggests that the tropospheric pattern that influences the location of AR landfall may begin to set up, in a composite sense, days prior to landfall.

3.3.3. Atmospheric River Attributes

Table 3.1 lists the mean attributes of ARs detected over the two landfall boundaries. Rather than using each AR event's first period as in Figures 3.4 and 3.5, Table 3.1 is constructed using mean attributes over the span of time each event persists over the landfall boundary. Boldface type in Table 3.1 denotes those attributes where the null hypothesis of equal means between the two locations can be rejected via a Welch's *t* test at the 95% confidence level.

TABLE 3.1. Mean AR attributes. See section 3.2.3 for definitions of the attributes and acronyms. Boldface type denotes where the null hypothesis of equal means between the two locations can be rejected via Welch's *t* test at the 95% confidence level

Location	Events Mean #	Persist. # Hours	Length km	Orient. $^\circ$	Area $1000\ km^2$	U Wind $m\ s^{-1}$	V Wind $m\ s^{-1}$	IVT $kg\ m^{-1}\ s^{-1}$	IVT′ $kg\ m^{-1}\ s^{-1}$	PWAT $kg\ m^{-2}$
					Annual					
Alaska	**40**	27	3383	**71**	1508	**2.1**	**11.9**	604	406	20
West Coast	**33**	28	3327	**58**	1532	**4.6**	**10.0**	599	406	20
					DJF					
Alaska	**11**	**14**	**3591**	**84**	1563	**-0.9**	**15.4**	**577**	**401**	**17**
West Coast	**13**	**18**	**3190**	**49**	1637	**8.1**	**10.7**	**603**	**415**	**19**

Table 3.1 reveals that, on average, many attributes are similar for ARs near the two locations. More specifically, the annual mean AR persistence, length, area, IVT, IVT′, and PWAT (see section 3.2.3 for definitions) are not statistically different. This suggests that the high-latitude ARs near Alaska are often comparable to their mid-latitude counterparts. The mean AR attributes in Table 3.1 also afford comparisons with other AR studies. Indeed, it is shown here that the mean AR lengths exceed the well-accepted 2000

km length minimum threshold (e.g., Ralph et al. 2004). The mean values of PWAT equal the oft-used 2 cm (or 20 kg m^{-2}) threshold in the annual mean analysis, but fall just shy when assessed over DJF only. The 28-hour mean persistence of annual U.S. West Coast ARs is longer than the 16- or 20-hour (depending calculation method) mean persistence reported in Ralph et al. (2013), that was based on in situ observations of 91 ARs making landfall near California's Russian River basin. While this difference in mean persistence may be due to the larger domain used this study, it is more likely that this difference results from the 6-hourly reanalysis data used in this comparison versus the hourly observations used in Ralph et al. (2013).

Some of the differences in the mean AR attributes in Table 3.1 can be visualized by the composite atmospheric conditions shown in Figures 3.4 and 3.5. For example, the abrupt shift from zonal to meridional flow over the North Pacific during DJF apparent in the composite of Gulf of Alaska ARs (Figure 3.4) substantiates the more north-south orientation, smaller mean low-level zonal winds (u wind), and greater mean low-level meridional winds (v wind) compared to the U.S. West Coast ARs. The difference between the mean AR lengths during DJF may be explained similarly. The Gulf of Alaska landfall boundary is farther removed from the mean position of the eddy-driven jet during the winter season, thus ARs associated with eddies along the jet must be longer in length, on average, in order to reach the fixed high-latitude boundary. That relationship is lost in the annual comparison of AR lengths, likely due to the seasonal migration of the eddy-driven jet. Again, these results are insensitive to small changes in the position and orientation of the landfall boundaries.

3.3.4. Atmospheric Conditions Comparison

Figure 3.6 reveals the differences between the Gulf of Alaska DJF AR event composite (Figure 3.4a) and the U.S. West Coast DJF AR event composite (Figure 3.5a) for 500 hPa geopotential heights (shading), sea level pressure (contours), and 700 hPa winds (arrows). The dominant feature in this difference plot is the resulting "anomalous" pressure, height, and circulation center in the northeast Pacific, for Gulf of Alaska ARs compared to U.S. West Coast ARs.

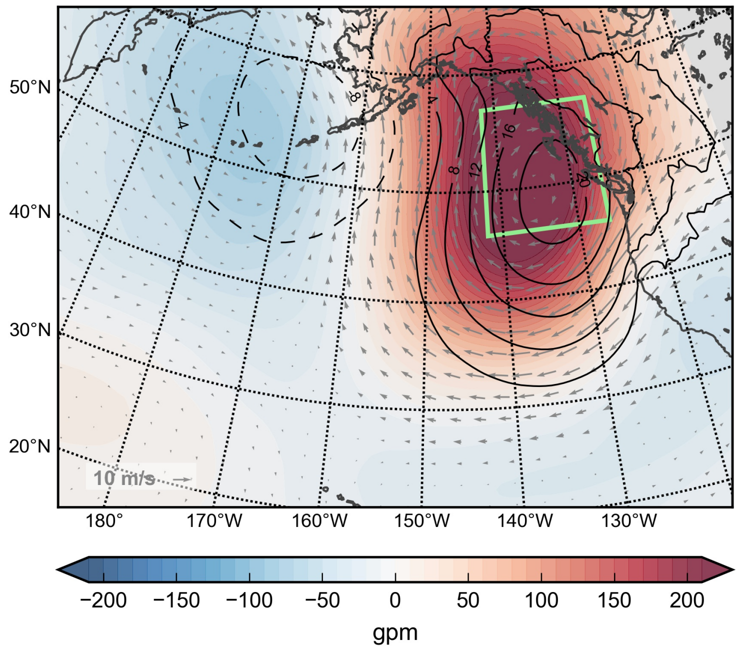

FIG. 3.6. Differences between the DJF composite atmospheric conditions resulting from the subtraction of the U.S. West Coast event composite (Figure 3.5a) from the Gulf of Alaska event composite (Figure 3.4a) in 500 hPa geopotential height (shading), sea level pressure (black contours; intervals of 4 hPa with the zero contour omitted), and 700 hPa vector winds (arrows). The green box outlines the region in which height anomalies are assessed (see text for description).

The spatial pattern of the height difference in Figure 3.6 is not unique to DJF, but is found in all seasons (not shown). The prevalence of this pattern motivates an assessment of the extent to which the anomaly feature over the northeast Pacific influences ARs near Alaska and the U.S. West Coast. Hereafter, this anomaly feature will be referred to as a geopotential height anomaly, but it may be thought of as a pressure or circulation anomaly too. To explore the relationship between this anomaly and ARs, we will evaluate 500 hPa geopotential height anomaly values (mean and seasonal cycle removed) averaged over the $11^\circ \times 16^\circ$ region identified by the green box in Figure 3.6. The resulting time series has an e-folding decay time of approximately 12 days, suggesting this anomaly is not just a transient feature associated with individual baroclinic waves. The height anomaly analysis box is located on the eastern periphery of the region of maximum annual geopotential height variability over the North Pacific (not shown). Shifting the box into the heart of the region of maximum variability may increase the dynamical signal, but reduces the influence on AR activity along southern Alaska.

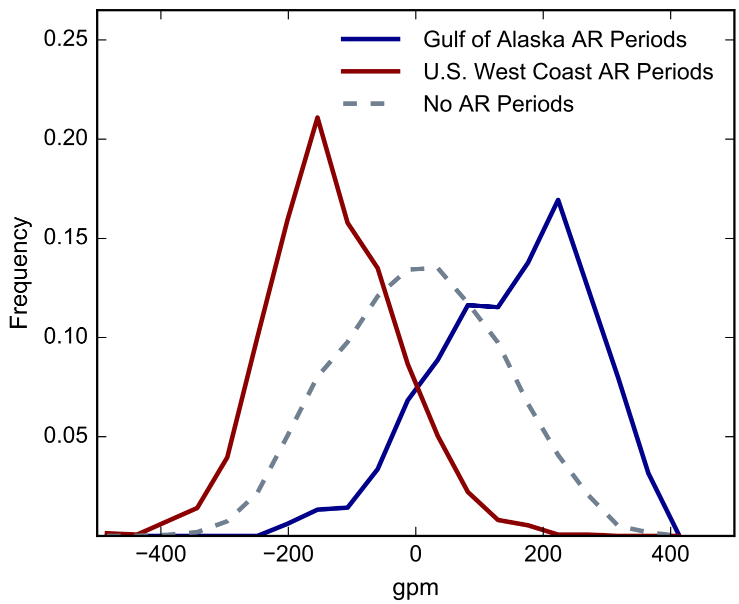

FIG. 3.7. Distributions of mean 500 hPa geopotential height anomalies for the region identified in Figure 3.6 for all DJF periods during which an AR was detected along the Gulf of Alaska landfall boundary (blue), along the U.S. West Coast landfall boundary (red), and during which no AR was detected near either location (gray).

Figure 3.7 presents frequency distributions of DJF height anomaly values averaged over the region identified in Figure 3.6. Here each 6-hour period is categorized based on whether an AR was detected over the Gulf of Alaska landfall boundary (blue), over the U.S. West Coast landfall boundary (red), or whether no AR was detected near either location (gray). Distinct distributions emerge. The distribution of height anomaly values associated with Gulf of Alaska AR periods is shifted toward positive anomalies. In contrast, the distribution of height anomaly values associated with U.S. West Coast AR periods is shifted toward negative values. These opposing shifts agree with the difference plot (Figure 3.6) that depicts greater height anomaly values from the Gulf of Alaska DJF composite compared to the U.S. West Coast composite. Though the distributions in Figure 3.7 are based only on DJF, frequency distributions for other seasons are similar (not shown). Thus, we find that the composite results are not dominated by a few outlier events, but rather represent the majority of ARs in the 37-year record.

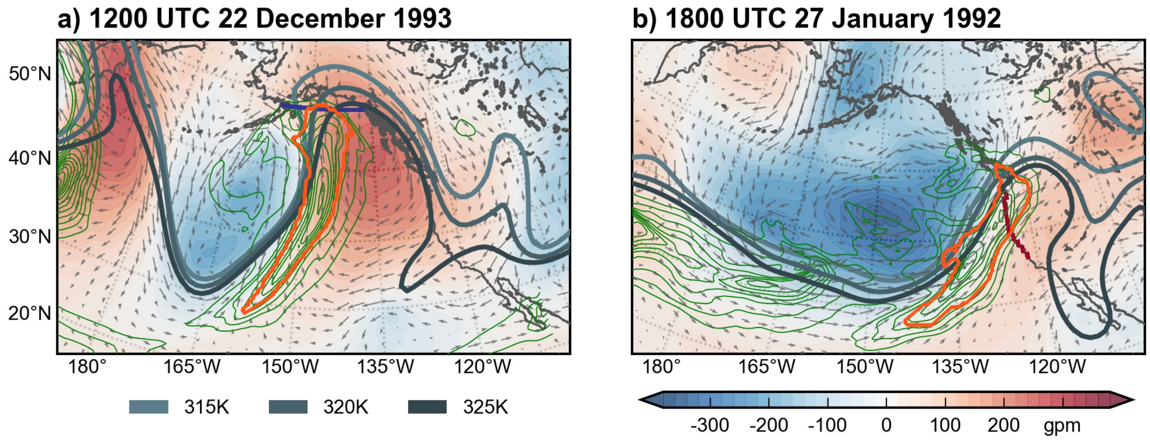

FIG. 3.8. ARs (orange outlines) impacting the (a) Gulf of Alaska and (b) U.S. West Coast landfall boundaries. Each panel includes 500 hPa geopotential height anomalies (shading), 700 hPa vector wind anomalies (arrows), IVT (thin green contours; intervals of 100 kg m^{-1} s^{-1} starting at 200 kg m^{-1} s^{-1}), and potential temperature contours on the 2 PVU surface used to assess Rossby wave breaking, smoothed via a two standard deviation multidimensional Gaussian filter (gray contours; 315–325K). The potential temperature legend (left bottom) and colorbar (right bottom) apply to both panels.

Up to this point we have presented composites and distributions based on large samples of ARs. Here we briefly analyze two representative ARs, one detected over each of the landfall boundaries. Each of the two panels in Figure 3.8 displays an AR that generally exemplifies the DJF mean attributes (i.e., those in Table 3.1) for the respective boundary. The 500 hPa geopotential height anomalies (shading) and 700 hPa wind anomalies (arrows) in Figure 3.8a generally reflect the composite difference plot in Figure 3.6, with a pronounced positive height anomaly center in the northeast Pacific. We propound that the timing, location, and character of this anomaly is important to the existence of the AR extending from the central Pacific to the Gulf of Alaska landfall boundary. The anomaly patterns in Figure 3.8b do not directly oppose those in Figure 3.8a, but a notable anomaly center of the opposite sign does extend into the northeast Pacific.

3.4. ATMOSPHERIC RIVER ACTIVITY ACROSS TIME SCALES

3.4.1. Synoptic Time Scale

From Figure 3.3 we appreciate that ARs are neither rare along the coast of southern Alaska nor the west coast of the U.S. mainland. However, we find that ARs concurrently impacting both boundaries simultaneously are rather uncommon. That is, only approximately 3.9% of all Gulf of Alaska AR events temporally overlap an AR landfalling along the U.S. West Coast. Similarly, approximately 4.8% of the U.S. West Coast ARs overlap in time an AR near Alaska. This rarity of concurrent landfalling ARs suggests that a dynamical link may exist for these two landfall boundaries, such that AR activity near one boundary relates, in part, to opposing AR activity near the other boundary.

Together with Figure 3.7, the two ARs depicted in Figure 3.8 provide evidence that height anomalies in the northeast Pacific may influence individual ARs near both landfall boundaries and may be the dynamical link influencing AR activity. Here we extend the analysis of this relationship over the entire 37-year record to quantify the association between ARs and these height anomalies on the scale of unique AR events. Of the AR events detected over the Gulf of Alaska landfall boundary, approximately 79% are associated with a positive mean height anomaly over the analysis box identified in Figure 3.6. These percentages vary seasonally, for example, ranging from 72% in July–September (JAS) to 85% in February–April (FMA). The opposing relationship holds for the U.S. West Coast landfall boundary, where approximately 14% of the detected AR events are associated with a positive mean height anomaly, while 86% are associated with a negative anomaly. Thus the ARs in Figure 3.8 are not outliers, but rather representative of a resilient relationship between northeast Pacific heights and AR activity on the scale of individual events.

The previous analysis assessed the northeast Pacific height anomaly and AR relationship in terms of individual AR events. If the relationship is robust and dynamically based, the relationship should also exist if assessed in terms of individual height anomaly events. Here, height anomaly events are defined as consecutive 6-hour periods during which the mean geopotential height anomaly within the analysis box maintains the same sign and meets or exceeds a +/- one standard deviation (sigma, σ) height anomaly threshold. When the one standard deviation threshold is used to define anomalous periods, the resulting height anomalies may hereafter be denoted as H'.

The probability of any AR occurring over the Gulf of Alaska boundary during a strong $+H'$ event is approximately 49% (see Table 3.2). That is to say, 49% of the 907 $+H'$ events within the 37-year record contain at least one period of time when an AR is detected near Alaska. In contrast, the probability of a Gulf of Alaska AR during a $-H'$ event drops to 6%. For the U.S. West Coast, the probability of an AR occurring is 3% and 45% during a $+H'$ event and a $-H'$ event, respectively. As with other measures, these probabilities vary seasonally, but generally follow the seasonality of ARs exhibited in Figure 3.3. These numbers indicate that the probability of any AR occurring may change drastically based on the state of the atmosphere over the northeast Pacific. While these calculations are based on +/- one standard deviation thresholds, we find a threshold of zero shows the same, yet weaker, relationships (not shown), and still indicates that the probability of any AR occurring may double or even triple based on tropospheric height conditions in the northeast Pacific.

TABLE 3.2. Percent of H' events with ≥ 1 AR period. Values in the parentheses represent the 95% confidence bounds from the distribution of 10,000 bootstrap iterations.

Location	$+H'$	$-H'$
Gulf of Alaska	**49%** (21–26%)	**6%** (19–24%)
U.S. West Coast	**3%** (17–22%)	**45%** (15–20%)

The probabilities in Table 3.2 are, perhaps, more meaningful when compared to rates of AR occurrence approximated by 10,000 bootstrap iterations. Each bootstrap iteration is constructed using the same number and duration of H' events as exist in the MERRA-based time series, with the starting periods randomly selected from the 37-year record. As constructed, this bootstrap analysis provides estimates of the probability of any AR occurring over the boundaries if no dynamical relationship with northeast Pacific height anomalies exists. For both landfall boundaries, we find that the actual AR probabilities exceed the 95% confidence bounds of the bootstrap distribution (given in Table 3.2), thus providing strong evidence of a dynamical link between H' and AR activity on the synoptic time scale.

The consistency of the northeast Pacific height anomaly and AR activity relationship regardless of whether it is evaluated based on AR events or height anomaly events demonstrates the robustness of the relationship. These analyses imply that this mechanistic relationship may provide predictability, such that knowledge of the current or future state of the large-scale flow over the northeast Pacific may provide information about the likelihood of AR activity. For example, if a broad, positive height anomaly is expected to build over the northeast Pacific and persist for approximately one week, the likelihood of AR activity near the Gulf of Alaska landfall boundary will be higher than climatology as a result, and the likelihood of AR activity near the U.S. West Coast will be lower than climatology, so long as the height anomaly persists.

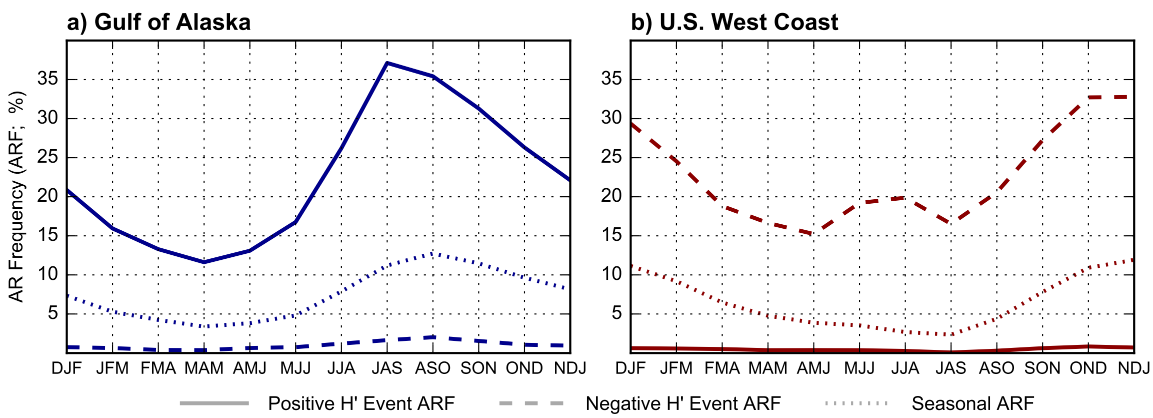

FIG. 3.9. Seasonality of the impact of northeast Pacific 500 hPa geopotential height anomalies (H′) meeting or exceeding a 1 σ threshold on AR frequency of occurrence (ARF) for the (a) Gulf of Alaska and (b) U.S. West Coast landfall boundaries. The solid curves represent the ARF during positive height anomaly events, the dashed curves represent the ARF during negative height anomaly events, and the dotted curves show the seasonal ARF (as shown in Figure 3.3) for comparison.

Ralph et al. (2013) documented that an AR's persistence over an area strongly influences its potential post-landfall impacts (e.g., heavy rainfall, flash flooding). Here we assess the combined influence of the total number, spatial extent, and persistence of ARs by considering AR frequencies (ARF). The seasonally-varying ARF for the two landfall boundaries are shown in Figure 3.3 and repeated as the dotted curves in Figure 3.9. Atmospheric river frequencies parsed by positive and negative height anomalies meeting or exceeding the respective one standard deviation threshold are also plotted (solid and dashed curves, respectively) for both landfall boundaries. Though the curves in Figure 3.9 display a pronounced seasonality, the percent increase or decrease relative to the seasonally-varying ARF are nearly constant throughout the year. Strong positive northeast Pacific height anomalies increase the ARF for the Gulf of Alaska boundary to nearly 22%, as compared to the annual mean frequency of 7.5%. The same positive height anomalies decrease the ARF for the U.S. West Coast boundary to less than 1%, or less than one-tenth of the annual mean frequency of 6.6%. Strong negative height anomalies have the opposite impact over the two locations of interest, decreasing the Gulf of Alaska ARF to 1% and increasing the U.S. West Coast ARF to 24%.

3.4.2. Subseasonal Time Scale

Finding a robust relationship between broad northeast Pacific height anomalies and AR activity at the synoptic time scale, we now assess whether the relationship holds for longer time scales. Extending the analysis to the subseasonal time scale, we consider the 444 calendar months in the 37-year record. A month is categorized as positive or negative H' if the month's mean anomaly value meets or exceeds a respective one standard deviation threshold. Similarly, a month is characterized as having increased or decreased AR activity based on the total number of AR periods in the month compared to climatology. The monthly values are compared to monthly climatologies, thus variability beyond subseasonal time scales (interannual, decadal, etc.) are retained in this analysis.

Figure 3.10 depicts the percent of calendar months with increased AR activity at each landfall boundary based on the monthly height anomaly. We find opposing AR activity during months with positive and negative height anomalies for the two landfall boundaries. For example, nearly 75% of the months with mean positive height anomalies meeting or exceeding one standard deviation have increased AR activity over the Gulf of Alaska, compared to only 13% with a mean negative height anomaly. For the U.S. West Coast, less than 10% of positive height anomaly months have increased AR activity, compared to nearly 80% of negative height anomaly months. The separation between the error bars, representing the 95% confidence intervals, for each location suggests a significant relationship at subseasonal resolution.

The results depicted in Figure 3.10 consider the height anomaly and AR activity relationship separately for each of the landfall boundaries. Here we expand the analysis to assess the combined, opposing response

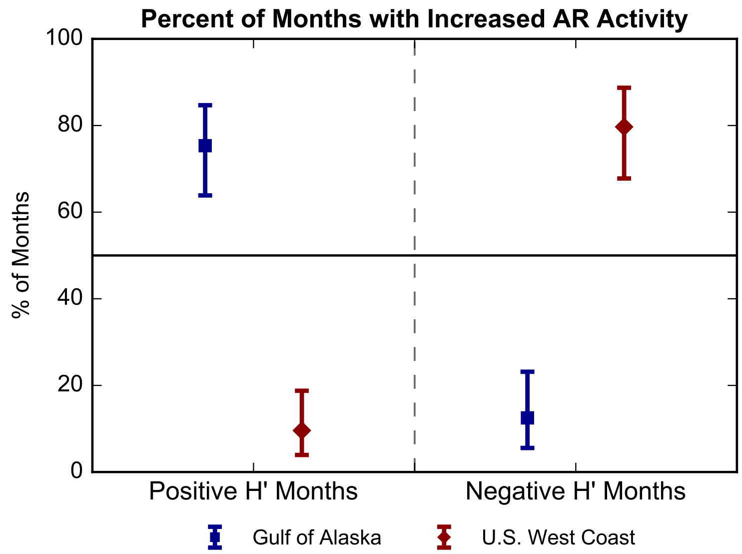

FIG. 3.10. Comparison of the percent of months with increased AR activity during months with mean positive northeast Pacific 500 hPa geopotential height anomalies $\geq 1\ \sigma$ (left) and mean negative height anomalies $\leq 1\ \sigma$ (right) for the Gulf of Alaska (blue with square markers) and U.S. West Coast (red with diamond markers). Error bars encompass the 95% confidence interval for a binomial distribution based on the Clopper-Pearson method (Clopper and Pearson 1934).

of AR activity at both locations (i.e., an increase in AR activity near Alaska together with a decrease in U.S. West Coast AR activity coincident with a positive height anomaly). We find that 69% of the months meeting or exceeding the one standard deviation height anomaly threshold exhibit a combined response in accordance with the northeast Pacific height anomaly and AR mechanistic relationship for both boundaries. Only 2% of the months display combined AR activity counter to the postulated relationships (i.e., a decrease in Alaska AR activity together with an increase in U.S. West Coast AR activity coincident with a positive height anomaly). However, 29% of the months show the same sign of anomalous AR activity over both boundaries regardless of the height anomaly, suggesting that a northeast Pacific height anomaly is not the sole mechanism responsible for subseasonal AR variability over the two landfall boundaries explored here.

3.4.3. INTERANNUAL TIME SCALE

We further extend our analysis to interannual anomalies, briefly evaluating year-to-year variations in the 36 extended boreal winter seasons (November through March (NDJFM)) within the MERRA reanalysis dataset. Here we explore whether seasons with notable mean height anomalies in the northeast Pacific, such as the persistent anomalous ridging that occurred during the winter of 2013–14 (e.g., Wang et al. 2014a; Lee et al. 2015; Bond et al. 2015), also have anomalous AR activity over the landfall boundaries. AR activity in the Gulf of Alaska is increased during only 52% of winter seasons with a mean positive northeast Pacific height anomaly and decreased during 60% of the seasons with a mean negative height anomaly. AR activity near the U.S. West Coast, however, exhibits the expected decrease in AR activity during 71% of seasons with a mean positive height anomaly and increase during 73% of the seasons with a mean negative anomaly. The higher percentages for the U.S. West Coast boundary suggest that the height anomaly box used in this study is positioned to better represent the forcing for interannual variability in wintertime AR activity for the U.S. West Coast than for Alaska.

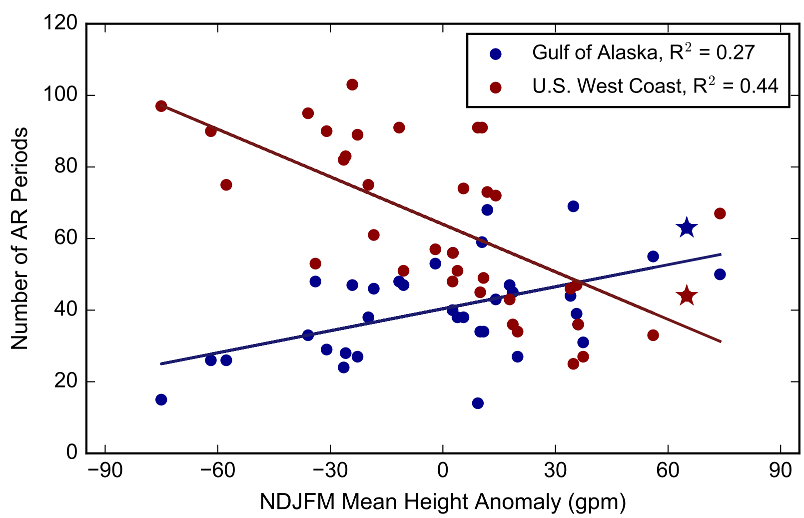

FIG. 3.11. Relationship between the total number of extended boreal winter (NDJFM) AR periods and the mean northeast Pacific height anomaly value, for the Gulf of Alaska (blue) and U.S. West Coast (red) landfall boundaries. Each winter season is indicated by a colored circle for each boundary, while the 2013–14 season noted in the text is identified by the stars. Solid lines represent the linear best fit, with the respective R^2 values listed in the legend.

These initial winter seasonal statistics are based solely on the signs of the mean NDJFM height anomalies. Next we assess the interannual relationship between anomalous heights and AR activity, but also include information regarding the strength of the height anomalies. Figure 3.11 reveals the relationship between the the total number of AR periods over each landfall boundary during each winter season compared to the mean height anomaly values. For the U.S. West Coast (red), we find an inverse relationship between AR activity and the height anomaly strength. A linear best fit line accounts for approximately 44% of the total variance. The opposite relationship exists for the Gulf of Alaska boundary (blue), where AR activity increases together with the strength of the mean height anomaly; the associated linear best fit line accounts for 27% of the variance. Thus, the relationship between height anomalies and AR activity identified at shorter time scales holds in terms of interannual variability.

Based on this analysis, the anomalous ridging that persisted over the northeast Pacific for much of the winter of 2013–14 (see, for example, Hartmann 2015, Figure 3a) was the second strongest of the 36 winter seasons (stars in Figure 3.11). AR activity was also extremely high over the Gulf of Alaska (third highest total number of AR periods out of the 36 seasons) and low over the U.S. West Coast (eighth lowest of the 36 seasons) during the winter of 2013–14. See Table S1 of the supporting information accompanying Mundhenk et al. (2016b) for a full listing of winter season ranks and values. This analysis suggests that the inclusion of a measure of the magnitude of height anomalies bolsters the mechanistic relationship between northeast Pacific height anomalies and AR activity at the interannual time scale.

3.5. LINKS TO LARGE-SCALE DYNAMICS

The preceding section documents a robust relationship between ARs both near southern Alaska and the U.S. West Coast and height anomalies over the northeast Pacific. The results suggest that this relationship applies across a range of time scales, from that of individual ARs and height anomaly events to interannual time scales. In an effort to link this relationship to the large-scale dynamics over the North Pacific, we are inspired by the documented association between wintertime ARs along the U.S. West Coast and Rossby wave breaking (RWB) (e.g., Ryoo et al. 2013; Payne and Magnusdottir 2014).

Using the RWB event atlas described in section 3.2.4, unique AR events may be linked in time and space with nearby RWB activity. For example, the representative ARs in Figure 3.8 are found to be associated with a developing cyclonic wave breaking (CWB) event and an anticyclonic wave breaking (AWB) event, for Figure 3.8a and Figure 3.8b, respectively (see the gray contours). Figure 3.12 reveals the percent of all AR events associated with CWB (green) and AWB (orange) for each of the landfall boundaries in terms of overlapping three-month seasons.

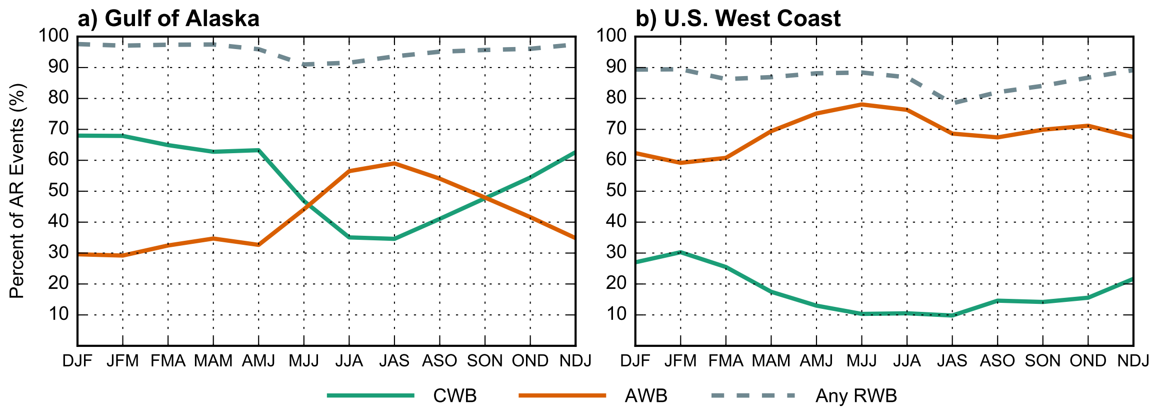

FIG. 3.12. Seasonality of the percent of AR events from 1979–2010 associated with Rossby wave breaking for the (a) Gulf of Alaska and (b) U.S. West Coast landfall boundaries. The colors denote different wave breaking directions with green representing cyclonic wave breaking (CWB) and orange representing anticyclonic wave breaking (AWB). The dashed gray curve in each panel represents the percent of AR events associated with any breaking event, regardless of type.

Over the Gulf of Alaska, ARs are collocated with both types of wave breaking throughout the year, as shown in Figure 3.12a. The seasonality in the dominant wave breaking direction may be attributed to the seasonal migration of the eddy-driven jet over the North Pacific. The Gulf of Alaska landfall boundary is positioned well poleward of the climatological jet position in boreal winter, thus in a region of cyclonic shear and favored CWB from OND–AMJ. As the jet migrates poleward during boreal spring and then retreats in the autumn, the landfall boundary is nearer the jet core itself, thus subject to cyclonic and/or anticyclonic shear, and associated wave breaking, as perturbations propagate through. During a brief period during boreal summer months (JJA–ASO), AWB dominates. Over the period 1979–2010, approximately 95% of all of the AR events detected over the Gulf of Alaska boundary are associated with RWB (dashed gray curve).

Figure 3.12b shows the percent of U.S. West Coast AR events associated with wave breaking, parsed by wave breaking direction. The U.S. West Coast boundary exhibits far less seasonal variability than the

Gulf of Alaska boundary and the apparent year-round link between ARs and AWB can be explained by the prevalence of anticyclonic breaking equatorward of the mean jet position (e.g., Payne and Magnusdottir 2014). Overall, nearly 86% of all AR events over the U.S. West Coast are associated with RWB.

Similarly, northeast Pacific height anomaly events are associated with nearby RWB activity. Over the northeast Pacific anomaly analysis box, the onset of approximately 97% of the positive height anomaly events that persist for at least two days during 1979–2010 spatially and temporally coincide with RWB. Here height anomaly events are defined as those meeting or exceeding a one standard deviation anomaly threshold and the onset defined as the 24 hours leading up to and including the first period when that is met. The 97% value exceeds the 99.9th percentile of a distribution of 10,000 bootstrap simulations of RWB occurrence with randomly selected onset periods. As defined, these broad, persistent positive height anomalies may be thought of as blocking anticyclones, the onset of which are often associated with the breaking of upper-level Rossby waves (e.g., Pelly and Hoskins 2003; Berrisford et al. 2007; Woollings et al. 2008; Tyrlis and Hoskins 2008). As a result, RWB should be considered integral to what we refer to in this work as positive northeast Pacific height anomalies.

Landfalling ARs and northeast Pacific height anomalies are both associated with Rossby wave breaking. Consequently, the mechanistic relationship identified in this work that relates AR activity near the landfall boundaries with northeast Pacific height anomalies is linked to the dynamics of the broader North Pacific. This dynamical linkage may bolster the understanding of periods of anomalous AR activity. For example, the documented relationships between organized tropical convection and remote Rossby wave activity (e.g., Moore et al. 2010; Adames and Wallace 2014; Branstator 2014) may help explain variability in AR activity over the west coast of North America, though a more extensive analysis shall remain for future work.

3.6. CONCLUSIONS

ARs occur throughout the year near southern Alaska and the U.S. West Coast. Climatologically, AR activity over both boundaries displays a pronounced seasonal cycle, peaking in August–October (ASO) near Alaska and in November–January (NDJ) near the U.S. West Coast. We find that, on average, AR attributes such as their persistence, length, area, IVT, IVT′, and PWAT are comparable for ARs in both regions, while attributes such as their orientation and low-level wind speeds often differ.

A comparison of composite atmospheric conditions over the North Pacific during Gulf of Alaska and U.S. West Coast AR events reveals a broad anomaly over the northeast Pacific differentiating the contrasting composites. Though this anomaly feature may be characterized as a pressure and/or circulation anomaly, we define it in terms of a 500 hPa geopotential height anomaly. Quantitatively, nearly 79% of Gulf of Alaska ARs are associated with a positive northeast Pacific height anomaly and 86% of U.S. West Coast ARs are associated with a negative anomaly. Therefore, the composites used in the comparison are not dominated by a few outlier events, but rather representative of the majority of ARs detected near the landfall boundaries.

We find that these height anomalies over the northeast Pacific are influential to AR activity over both landfall boundaries, presenting an AR activity "tradeoff" between the two locations. When a positive height anomaly exists over the northeast Pacific, AR activity is often deflected poleward toward Alaska. This increase in AR activity near Alaska comes at the cost of AR activity along the U.S. West Coast, which experiences a decrease in AR activity relative to climatology. The opposing relationship also applies, that is, AR activity is decreased near Alaska and increased along the west coast of the U.S. in the presence of a negative northeast Pacific height anomaly.

Results indicate that this modulation of AR activity is robust, as the impacts on AR activity are consistent and quantifiable in terms of AR events, height anomaly events, and AR frequencies. We find that the anomalous circulation associated with broad northeast Pacific height anomalies influences the landfall location and character of ARs. However, height anomalies in the northeast Pacific analysis box alone are insufficient to account for all of the variability in AR activity (see the distribution spread in Figure 3.7).

The modulation of AR activity by northeast Pacific height anomalies not only applies at the synoptic time scale, but also at subseasonal and interannual time scales. For example, we find that the anomalous ridging that persisted over the northeast Pacific for much of the winter of 2013–14 coincided with anomalously high AR activity near the Gulf of Alaska boundary and low AR activity near the U.S. West Coast boundary over the same period.

Landfalling ARs and persistent positive northeast Pacific height anomalies are both found to be associated with Rossby wave breaking, thereby dynamically linking AR activity and blocking-like height anomalies with broader North Pacific dynamics. These dynamical relationships may be exploited to assess, and perhaps predict, anomalous AR activity. For example, Henderson et al. (2016) found a near doubling of the frequency of wintertime east Pacific blocking events following the propagation of the intraseasonal Madden–Julian oscillation's (MJO's) active phase over the western Pacific (i.e., the real-time multivariate MJO index's phase 7). After compositing AR occurrences by the state of the MJO, both Guan and Waliser (2015) and Mundhenk et al. (2016a) found increased AR frequencies over portions of the northeast Pacific associated with similar MJO phase events.

Together with the investigation of AR occurrences and their composite atmospheric conditions, the Rossby wave breaking evaluation and related dynamical analysis afford a better understanding of the dynamics supporting high-latitude ARs over the North Pacific compared to their mid-latitude counterparts. Though the predictive skill of the mechanistic relationship is not quantified in this chapter, knowledge of the current or future state of the large-scale flow over the northeast Pacific may provide valuable, predictive information about the likelihood of AR activity over a range of time scales.

CHAPTER 4

SUBSEASONAL PREDICTION OF ATMOSPHERIC RIVER ACTIVITY

4.1. INTRODUCTION

A comparative gap in forecast guidance exists between medium-range weather forecasts (up to 2 weeks) and seasonal outlooks (3+ months) (e.g., Robertson et al. 2015; Vitart et al. 2017; White et al. 2017). Thus, opportunities abound to add far-reaching value to society with skillful predictions of extreme, and frequently hazardous, weather events that occur within this so-called subseasonal-to-seasonal gap (White et al. 2017). Sectors such as agriculture, energy production, resource management, and insurance stand to benefit from advance notice of weather extremes in order to prepare for such events.

Here, we focus on the subseasonal time scale that spans forecast lead times of approximately 2–5 weeks. Skillful predictions of extratropical phenomena within this time scale generally rely on the prediction of large-scale atmospheric circulation anomalies (e.g., Black et al. 2017), which are often linked to tropical disturbances that excite quasi-stationary Rossby waves that propagate into the extratropics (e.g., Hoskins and Karoly 1981; Sardeshmukh and Hoskins 1988; Matthews 2004). Indeed, predictive power in the subseasonal time scale is largely associated with the evolution of far-reaching teleconnections produced by tropical phenomena such as the Madden-Julian oscillation (MJO) (e.g., Hoskins 2013; Zhang 2013). The MJO is the dominant mode of intraseasonal variability in the tropical troposphere, and is often characterized by a large-scale pattern of coupled anomalous atmospheric circulation and deep convection that propagates eastward along the equator with a period of approximately 30–90 days (Zhang 2005). Additionally, the MJO is known to be an important source of subseasonal predictability (Gottschalck et al. 2010; Waliser 2011; Zhang 2013) and can support predictions of various phenomena outside of the tropics. For example, an empirical model for predicting North American 2-meter temperatures recently developed in Johnson et al. (2014) based on the MJO, linear trends, and the El Niño-Southern Oscillation (ENSO) cycle produces skill and provides valuable guidance beyond a basic climatological forecast. Moreover, the teleconnection patterns associated with the ENSO cycle and the MJO provide a scientific basis for subseasonal prediction with operational forecast models (e.g., DelSole et al. 2017).

Emerging science is illuminating the influence that the state of the tropical stratosphere has on the MJO and its teleconnections. Here, the state of the stratosphere is represented by the phase of the quasi-biennial oscillation (QBO). The QBO is the dominant mode of the variability in the tropical stratosphere and is itself highly predictable (Scaife et al. 2014). The QBO represents a downward propagating shift in the mean zonal winds in the equatorial stratosphere from westerlies to easterlies and back again, with a period of approximately two years (see Baldwin et al. 2001, and references therein). A growing body of research suggests that the state of the stratosphere, as represented by the QBO, influences the nature and predictability of the MJO (Yoo and Son 2016; Marshall et al. 2016), as well as the MJO's associated atmospheric teleconnections (Marshall et al. 2016; Son et al. 2017). For example, MJO activity during boreal winter is generally higher in amplitude and slower to propagate during the easterly phase of the QBO than during the westerly phase (Liu et al. 2014b; Yoo and Son 2016; Nishimoto and Yoden 2017; Son et al. 2017). This modulation of the MJO by the QBO can occur independent of the ENSO cycle (Yoo and Son 2016; Son et al. 2017; Nishimoto and Yoden 2017). While the physical processes responsible for the modulation of the MJO by the QBO are still being investigated, the relationship appears to be dominated by the regulation of the near-tropopause temperature and static stability and hence a modulation of organized deep convection (Yoo and Son 2016; Nishimoto and Yoden 2017).

In this chapter, we construct and evaluate an empirical prediction scheme targeting anomalous landfalling atmospheric river (AR) activity along the west coast of North America. ARs are plumes of intense tropospheric water vapor transport that often result in weather and/or hydrologic extremes (e.g., heavy rainfall, flash floods) upon landfall (e.g., Ralph et al. 2006; Smith et al. 2010; Neiman et al. 2011; Ralph and Dettinger 2011). Repeated landfalling ARs or a complete lack thereof may result in periods of precipitation abundance or drought for regions along the west coast of North America (e.g., Dettinger et al. 2011; Dettinger 2013). Several studies suggest the potential for skillful subseasonal prediction based on observed relationships between the MJO and AR activity (Ralph et al. 2011; Guan et al. 2012b; Payne and Magnusdottir 2014; Guan and Waliser 2015; Mundhenk et al. 2016a). Here, we show for the first time that knowledge of the state of the MJO and the QBO can provide actionable predictions of anomalous AR activity up to 5 weeks in advance during boreal winter months. Because of the wide-ranging impacts associated with landfalling ARs, myriad sectors of society may benefit from skillful predictions of anomalous AR activity along the west coast of North America.

4.2. RESULTS

ARs impact the west coast of North America during every month of the year (Mundhenk et al. 2016a). However, regions along the coast experience a pronounced seasonality in AR frequency of occurrence that generally varies with latitude (Neiman et al. 2008b; Mundhenk et al. 2016b). The landfall boundaries used in this study, as identified in Figure 4.1a, are no exception. Figure 4.1b shows the seasonal cycle of landfalling ARs near British Columbia (BC; blue) and California (CA; red) based on ARs identified in the second Modern-Era Retrospective Analysis for Research and Applications (MERRA-2) dataset (GMAO 2015). We focus our analysis on the December through March (DJFM) period, as shaded in Figure 4.1b, when ARs frequently occur near both the British Columbia and California landfall boundaries, when teleconnection patterns are expected to be the most robust over the North Pacific, and when the aforementioned MJO–QBO link has been observed. In Figure 4.1b, ARs occur at a frequencies of approximately 12.4% and 11.5% of all days during DJFM for the British Columbia and California boundaries, respectively. Not shown is the substantial year-to-year variability in AR occurrences (e.g., Mundhenk et al. 2016a,b) indicating that landfalling ARs are also influenced by longer time scale modes of variability such as the ENSO cycle.

AR activity near these landfall boundaries not only varies on seasonal and longer time scales, but also within the subseasonal time scale. Here, we assess the modulation of AR activity following periods when the MJO is active. The MJO is parsed into eight phases that relate to the approximate location of the anomalous convection associated with the MJO, according to the components of the real-time multivariate MJO (RMM) index (Wheeler and Hendon 2004). Figure 4.2 depicts anomalous AR frequency of occurrence following

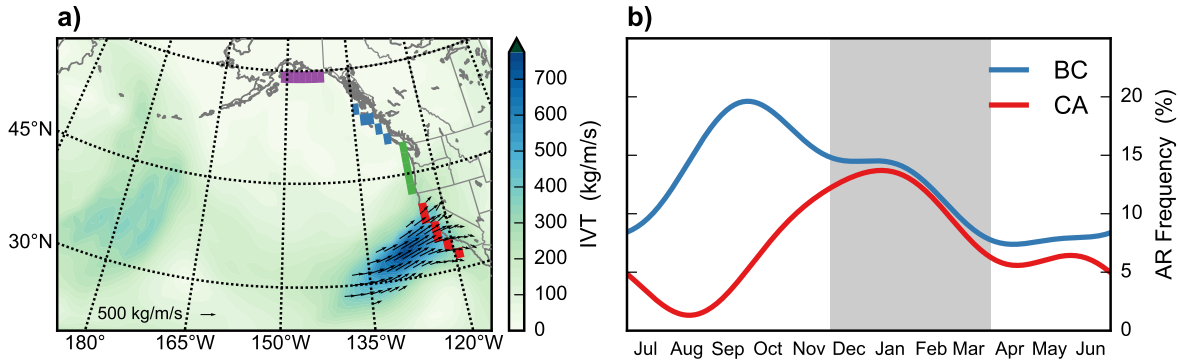

FIG. 4.1. (a) Location of the Alaska (purple), British Columbia (BC; blue), Washington/Oregon (green), and California (CA; red) landfall boundaries overlaying the daily mean integrated water vapor transport (IVT; shaded) from 20 February 2017. The black IVT vectors highlight an AR that impacted the CA boundary on that date. (b) The seasonal cycle of AR frequency of occurrence for the BC (blue curve) and CA (red curve) landfall boundaries, with the December–March (DJFM) period shaded.

dates when the MJO is active at time zero and in a given phase, based on the 36 DJFM seasons (1980–2016) within the MERRA-2 record. These composite anomalies may also be thought of in terms of percent change relative to the aforementioned 12.4% and 11.5% DJFM mean AR frequencies for British Columbia and California, respectively. As such, Figure 4.2 reveals composite patterns of anomalous AR activity following certain MJO phases that exceed +/- 50% of the seasonal AR frequency of occurrence. The opposing anomaly patterns in Figure 4.2 also capture a tradeoff in AR activity between British Columbia and California. For example, the increase in AR activity near British Columbia approximately two weeks following MJO phase 2 contrasts with a simultaneous decrease in activity near California (see also Mundhenk et al. 2016b).

In addition to the modulation of AR activity following active MJO periods, Figure 4.2 captures some key characteristics of the MJO and its extratropical response. For example, the angled, alternating pattern of anomalous AR activity captures the eastward propagation of the canonical MJO signal. Additionally, Figure 4.2 reveals that the maximum MJO-related impacts may take several days, or even weeks, to manifest, in agreement with the results of earlier theoretical work (e.g., Jin and Hoskins 1995; Matthews 2004). Notably, these patterns emerge despite the high degree of variability (duration, strength, evolution, etc.) within the underlying MJO events.

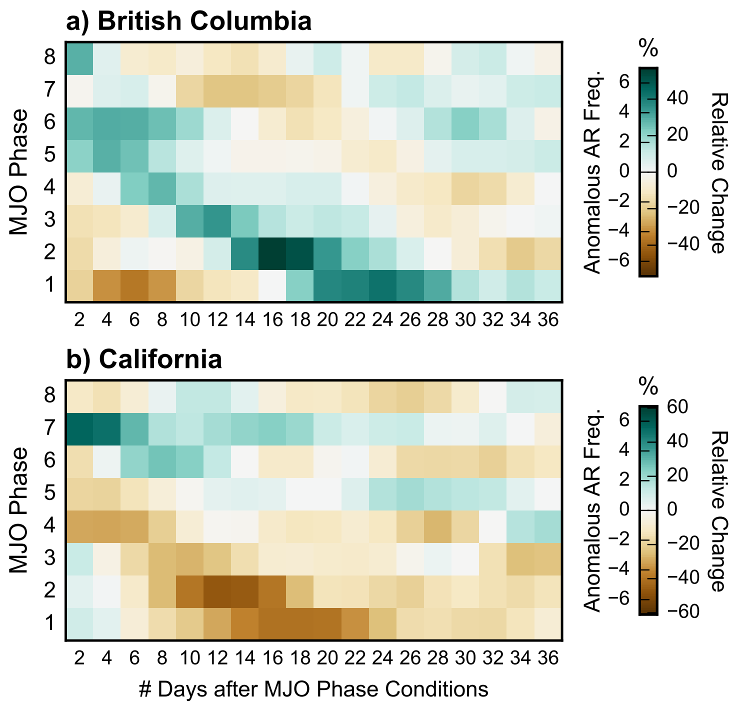

FIG. 4.2. Composite anomalous AR activity as a function of MJO phase (y axis) and number of days after active MJO phase conditions (x axis) in terms of anomalous frequency of occurrence (%, left range of colorbar) and the change relative to the location's mean DJFM AR frequency (% change, right range of colorbar) for the (a) British Columbia and (b) California landfall boundaries.

Despite the revealing patterns in Figure 4.2, such an analysis does not assess whether the modulation of AR activity following MJO activity is of use in a predictive sense. Here, we develop an empirical prediction scheme to evaluate the predictive potential of the MJO–AR relationship. In this first version of the scheme, the predictor is the initial state of the MJO, represented simply by the numeric MJO phase on the date of forecast issuance. The predictand is anomalous AR activity at some date in the future (i.e., forecast lead) near a given landfall boundary. While others have evaluated the ability of medium-range weather forecasts to represent individual AR events (Wick et al. 2013b), we target periods of AR activity relative to the seasonal cycle and smoothed by a 5-day running mean. This particular choice of predictand transforms the transient, synoptic-scale nature of individual ARs into a broader representation of the propensity of the large-scale flow pattern to support anomalous AR activity (i.e., increased or decreased activity relative to the seasonal climatology) and is a more suitable target for subseasonal prediction.

Using a leave-one-out cross-validation training and verification approach, we verify the prediction scheme on all DJFM dates for forecast lead times spanning 2 to 36 days. Forecast leads are defined as the number of days between the initial conditions (i.e., when forecasts are made) and the verification dates (i.e., the dates for which AR activity is forecast). Thus, MJO conditions as early as late October are used as predictors. The Heidke skill score (HSS; see Methods) is used to quantify the value added by this prediction scheme. As constructed, the HSS ranges from -100 (no correct forecasts) to 100 (all forecasts are correct), and HSS values greater than zero indicate conditions when the scheme adds value compared to a climatological forecast.

Figure 4.3 depicts the skill of the empirical prediction scheme as a function of MJO phase and forecast lead time for the British Columbia and California landfall boundaries. The panels in Figure 4.3 are shaded where the HSS is positive, that is, where skill emerges from this empirical prediction scheme. The extent of the shading in Figure 4.3a–b reveals that the MJO–AR relationship provides useful information within the subseasonal time scale beyond a simple climatological forecast. For context, an HSS value of 33 means that there are twice as many correct forecasts as incorrect forecasts. The color of the shading in Figure 4.3 relates to the AR response, with orange shading for decreased AR activity and green shading for increased AR activity. The skillful response patterns in Figure 4.3a–b share some similarities with the composite patterns shown in Figure 4.2. For example, the band of anomalously high AR activity near British Columbia following MJO phases 1–6 in Figure 4.2a supports skillful predictions of increased AR activity following the same phases in Figure 4.3a. Additionally, the patterns of skillful predictions suggest that the composites in Figure 4.2 are not dominated by just a few outlier events, but rather capture robust shifts in AR activity due to the state of the MJO up to 5 weeks prior.

Inspired by recent work investigating the impacts of the QBO on the MJO, we repeat our predictions but now include the phase of the QBO as an additional predictor. In Figure 4.3, panels c–f follow the format of panels a–b, but are parsed according to QBO phase: easterly QBO (EQBO) and westerly QBO (WQBO). As an example, the streak of statistically significant skill for increased AR activity near British Columbia

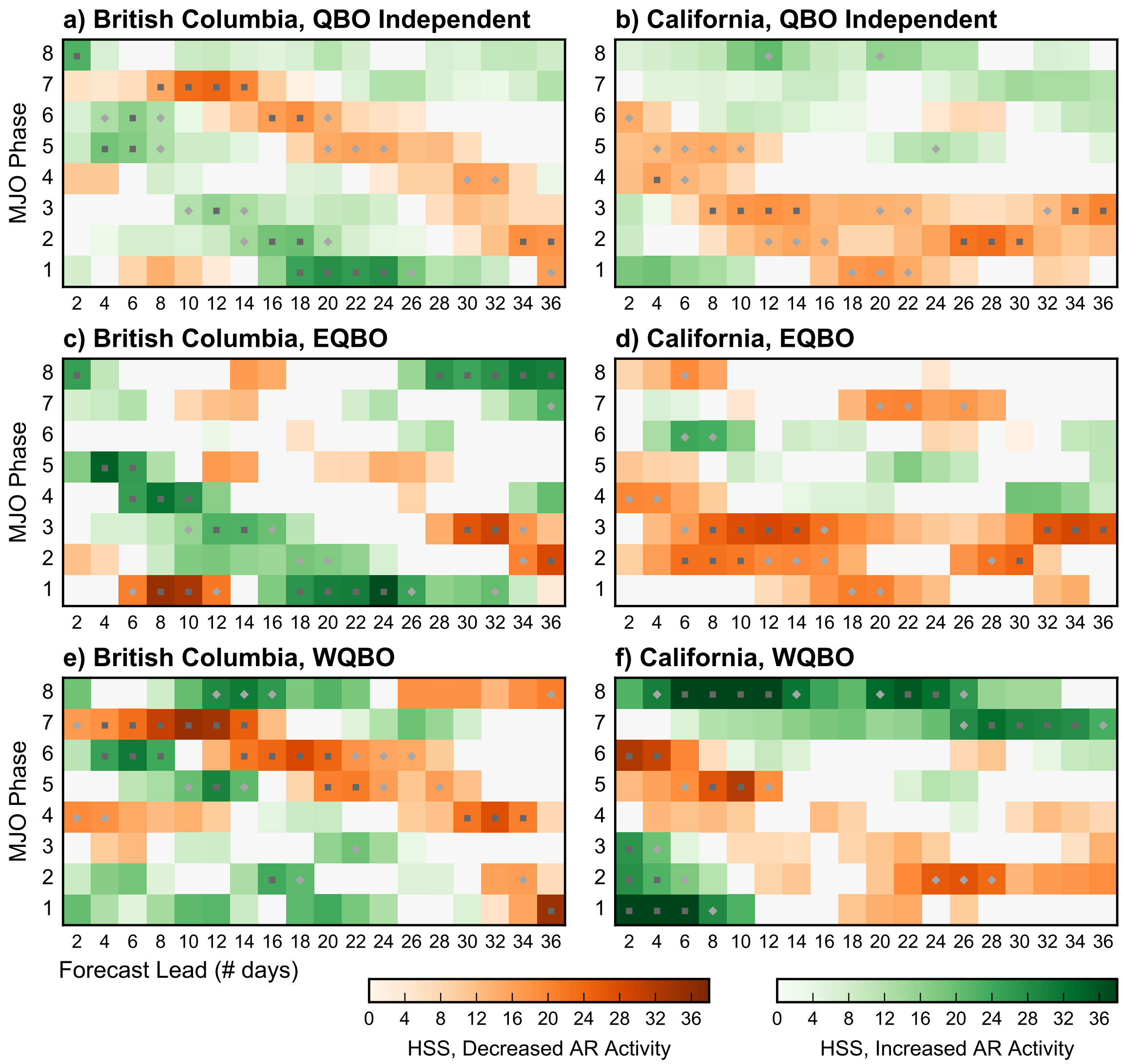

FIG. 4.3. Heidke skill score (HSS) values as a function of MJO phase (y axis) and forecast lead time (x axis) for the British Columbia (left column) and California (right column) landfall boundaries, (a–b) independent of the state of the QBO, as well as conditioned on (c–d) EQBO and (e–f) WQBO. Only conditional combinations where the HSS is positive are shaded. The shading is based on the dominant AR activity response: decreased activity (oranges) or increased activity (greens). Statistical significance of the skill scores is denoted by the light gray diamonds ($\geq$ 80th percentile) and dark gray squares ($\geq$ 90th percentile), based on 1000 block bootstrap samples (see Methods).

during EQBO conditions and 18–26 days following MJO phase 1 (bottom row of Figure 4.3c) indicates that given the initial conditions of EQBO and active MJO phase 1, one should expect an increase in AR activity relative to the seasonal climatology approximately three weeks following. The skill metric suggests that such a prediction of increased AR activity would be correct approximately 20 times out of 30. We also find that when the prediction scheme adds value (HSS >0), the skill is often higher with the addition of the QBO as a predictor. While some of the general skill and response patterns from the "QBO independent" panels remain once parsed by QBO phase, it is apparent that the patterns of AR activity not conditioned on QBO are dominated by one phase of the QBO. For example, the band of increased AR activity near British Columbia 1–3 weeks following MJO phases 1–3 is most pronounced during EQBO conditions.

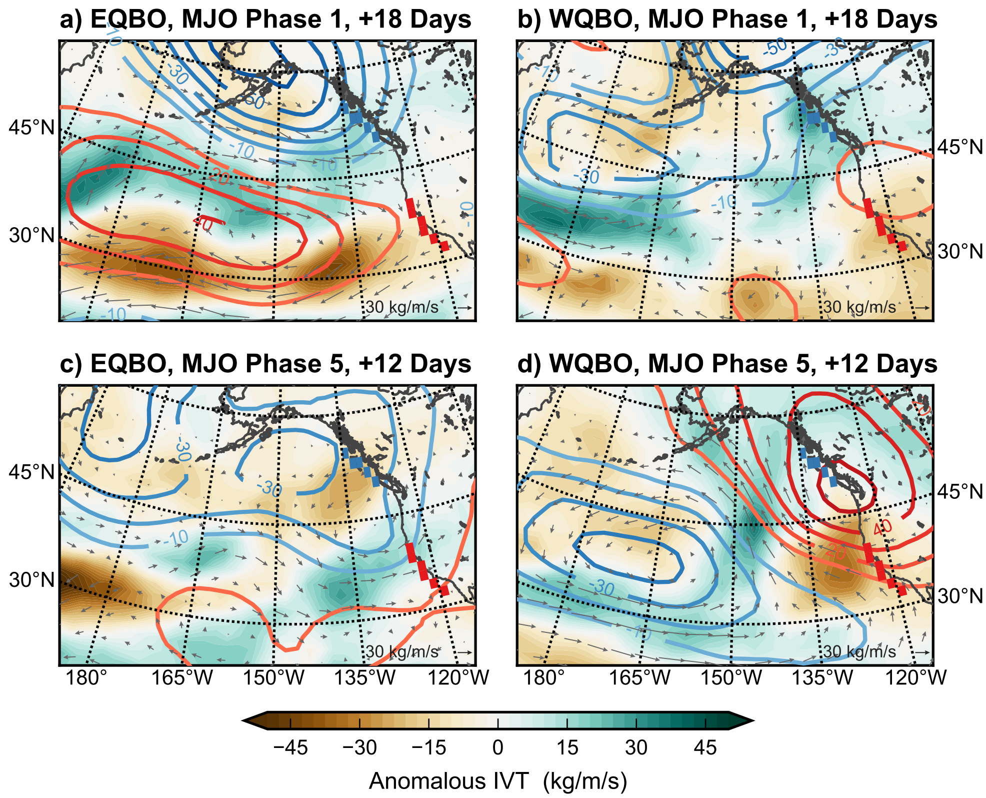

FIG. 4.4. Composites of anomalous integrated water vapor transport (IVT; shaded and arrows), positive 500 hPa geopotential height anomalies (red contours), and negative 500 hPa geopotential height anomalies (blue contours) for (a) 18 days following DJFM MJO phase 1 dates during EQBO conditions, (b) 18 days following MJO phase 1 dates during WQBO, (c) 12 days following MJO phase 5 dates during EQBO, and (d) 12 days following MJO phase 5 dates during WQBO. The British Columbia (blue) and California (red) landfall boundaries are overlaid.

To learn more about the dynamics that contribute to the AR response patterns shown in Figure 4.3, we examine composites of integrated water vapor transport (IVT) and 500 hPa geopotential height anomalies over the North Pacific. The large-scale anomaly patterns reveal conditions that act to influence AR activity near the landfall boundaries. Perhaps not surprisingly, the more skillful the prediction scheme (i.e., higher and more significant HSS), the more coherent the associated anomaly patterns appear over the North Pacific. For example, conditional composites for 18 days following MJO phase 1 dates during easterly and westerly QBO conditions are shown in Figures 4.4a and 4.4b, respectively. In Figure 4.4a, a negative height anomaly centered over mainland Alaska contrasts with a broad positive height anomaly encompassing much of the North Pacific. These anomaly patterns favor anomalously high AR activity near British Columbia and low AR activity near California. The anomaly patterns are less pronounced during westerly QBO conditions (Figure 4.4b), but the associated AR activity impacts are of the same sign regardless of QBO phase. In contrast, panels c–d of Figure 4.4 show composite conditions for 12 days following MJO phase 5 dates with dissimilar extratropical anomaly patterns based on QBO phase and with the composite anomaly pattern appearing substantially weaker and less coherent in the easterly QBO phase. In both panels, the composite height and IVT anomaly patterns are conducive for an AR activity tradeoff between the two landfall boundaries (Mundhenk et al. 2016b). Overall, the example composites shown in Figure 4.4 highlight that the anomalous AR response patterns (e.g., Figure 4.3) are linked to the large-scale modulation of the extratropical circulation.

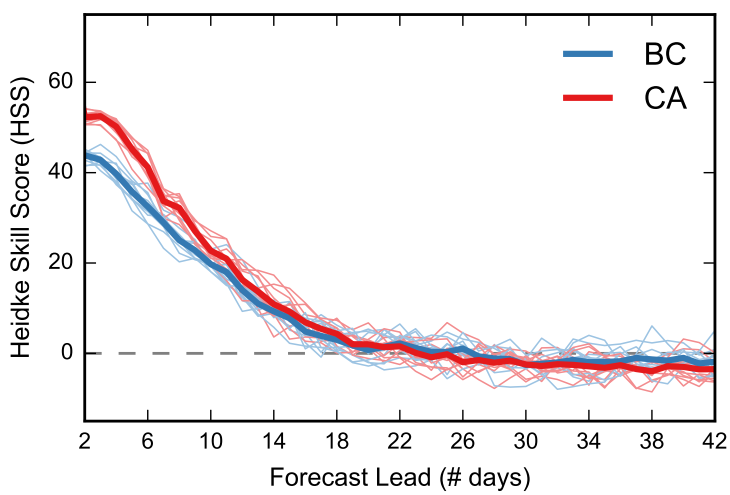

FIG. 4.5. HSS values based on ECMWF reforecast predictions of anomalous AR activity as a function of forecast lead time (x axis) for the British Columbia (BC; blue) and California (CA; red) landfall boundaries. Fine lines represent individual ensemble members and the bold lines denote the mean skill of all ensemble members for each region.

A worthwhile question is how does the level of skill from this empirical prediction scheme compare to the skill available from numerical weather prediction models? To answer this question, we evaluate a suite of 46-day European Centre for Medium-Range Weather Forecasts (ECMWF) retrospective forecasts initialized from 1995 to 2016 (Vitart et al. 2017). As with the empirical method, we target 5-day average anomalous AR activity for each landfall boundary. Figure 4.5 shows the resulting HSS based on all verification dates in DJFM as a function of forecast lead time for both the British Columbia (blue) and California (red) landfall boundaries. The ECMWF ensemble prediction system shows skill initially; however, the skill decreases to near zero at approximately 18 days. Thus, the model's subseasonal skill with this metric is roughly equivalent to a climatological forecast beyond forecast lead times of 18 days. The HSS values plotted in Figure 4.5 are not parsed by MJO and QBO phase; however, the results do not vary remarkably when the initial state of the MJO and the QBO are considered. This brief assessment is not intended to be a critique of this particular model, but rather to provide a rough estimate of the ability of a current generation numerical weather prediction model to predict anomalous AR activity within the subseasonal time scale.

4.3. DISCUSSION

This research illuminates the predictive potential of the relationship between anomalous landfalling AR activity along the west coast of North America and the state of the tropics up to 5 weeks prior. Earlier works have documented an MJO–AR relationship in terms of the modulation of AR occurrences (e.g., Payne and Magnusdottir 2014; Guan and Waliser 2015; Mundhenk et al. 2016a) and their impacts (e.g., Guan et al. 2012b), but here we demonstrate that the time-lagged modulation of AR activity by the extratropical response to the MJO can be leveraged for skillful subseasonal forecasts. We further show that the MJO–AR relationship is influenced by the QBO. Thus, the variability of the MJO–AR relationship can be better understood and predicted by also considering the state of the stratosphere. Furthermore, key aspects of the skill and AR response patterns are generally robust to the indices and thresholds used to characterize the MJO and the QBO.

An empirical prediction scheme using the initial state of the MJO and the QBO as predictors can support skillful subseasonal "forecasts of opportunity." As shown, during certain phase combinations (i.e., MJO phase, QBO phase, and forecast lead) the prediction scheme produces skill at forecast lead times of 2–5 weeks exceeding that of a state-of-the-art numerical weather prediction model, when evaluated using a similarly-constructed metric for above and below normal AR activity. Our scheme could be operationalized in such a manner as to revert to climatology if no additional skill can be expected, thus affording continuous application to complement available numerical weather prediction guidance. Furthermore, the method could be married with predictions of the MJO itself (e.g., Wang et al. 2014b), predictions which now show skill out 3–4 weeks in some dynamic models and situations (Vitart and Molteni 2010; Kim et al. 2016).

As ARs can trigger wide-ranging impacts, even modest gains in the subseasonal prediction of these impactful features may benefit numerous sectors of society. Also significant is the result that the MJO–AR relationship is responsible for not only periods of increased landfalling AR activity, but also periods of decreased activity. Given the potential consequences of a lack of AR activity, inactive periods may be just as viable and valuable a predictive target as abnormally active periods. Whatever the response, this study elucidates key relationships that contribute to the subseasonal variability of these extreme events and support skillful predictions thereof. The resulting empirical prediction scheme can help close the subseasonal gap in forecast guidance and foster timely decision making.

4.4. METHODS

4.4.1. ATMOSPHERIC RIVER DETECTION

ARs are identified using an updated version of an objective detection algorithm documented in Mundhenk et al. (2016a) and Appendix A. The algorithm uses gridded fields of positive anomalous vertically integrated water vapor transport (IVT), together with a series of intensity and geometric tests (e.g., mean intensity, total area, length, length-to-width ratio), to identify features that are of the appropriate spatial scale and are sufficiently plumelike in nature. This detection algorithm employs an occurrence-based approach (i.e., an AR occurrence is recorded for each period during which the criteria are satisfied), wherein each time step is scrutinized independently. As a result, the calculations regarding AR "hits" described in this study are based on the number of days during which AR-like conditions exist over a given landfall boundary. The updated detection algorithm used in this study does not contain the "multiple peak" logic that scrutinizes connected features within fields of anomalous IVT. We find that the mid- and high-latitude results are generally insensitive to the removal of this logic test. The majority of the results presented in this work are based on this detection algorithm applied to IVT calculated via the mass-weighted vertical integration of component winds and specific humidity from 1000-250 hPa from the second Modern-Era Retrospective Analysis for Research and Applications (MERRA-2) from 1980-2016 (GMAO 2015). Daily means are calculated and the dataset is regridded to a $1.5^\circ \times 1.5^\circ$ latitude-longitude grid before calculating IVT. With this dataset, a static anomalous IVT magnitude threshold of $\sim$173 kg m^{-1} s^{-1} is used to isolate features of interest. This value represents the 94th percentile of the all-season distribution of daily IVT anomaly values over the North Pacific Ocean. For the model skill comparison, this AR detection scheme is also applied to gridded IVT anomalies calculated from a set of retrospective forecasts from the European Centre for Medium-Range Weather Forecasts (ECMWF) reforecast ensemble prediction system.

4.4.2. Atmospheric river activity

To construct time series of anomalous AR activity along the landfall boundaries, we first create a continuous time series of boolean AR "hits" for each boundary by recording a hit whenever the spatial extent of any AR feature overlaps at least one grid point of a given landfall boundary. Second, we remove the seasonal cycle of AR activity by subtracting the mean and first two harmonics calculated via fast Fourier transform applied to the calendar-day means of each AR time series. Third, we apply a 5-day running mean to each anomaly time series. Based on the premise that subseasonal predictions are founded on the presence and modulation of large-scale circulation anomalies, the running mean transitions the time series from representing only individual transient hits to capturing the larger-scale propensity of the anomalous flow pattern to influence the landfalling activity. The resulting time series are used to create the conditional composites for Figure 4.2 and to train and verify the prediction scheme described throughout this work.

4.4.3. PREDICTORS

Two potential sources of subseasonal predictability are used as initial conditions for the prediction scheme: the MJO and the QBO. We characterize the MJO according to the strength and location of the enhanced near-equatorial convection and the associated anomalous circulation, as determined by the components of the real-time multivariate MJO (RMM) index (Wheeler and Hendon 2004). This MJO index is a combination of two component indices, RMM1 and RMM2, representing the two leading principal components from a multivariate (equatorially averaged tropical outgoing longwave radiation and 200- and 850-hPa zonal winds) empirical orthogonal function analysis. When combined and considered in terms of their two-dimensional phase space, these component indices provide daily phase (1–8) and amplitude values (Wheeler and Hendon 2004). We consider the MJO as active when the amplitude meets or exceeds a value of one and also apply the basic logic test that the index must remain in that phase (e.g., location of active MJO signal) for at least two, but less than 20, days. See the Supplementary Information for alternative characterizations of the MJO (e.g., different index or more stringent phase event criteria). The QBO is characterized by the standardized monthly 50 hPa zonal wind index provided by the National Oceanic and Atmospheric Administration (NOAA) National Weather Service (NWS) Climate Prediction Center (CPC). We apply this index as a continuous time series, such that all months within the period of record are categorized as either EQBO (monthly mean standardized anomaly <0) or WQBO (>0). The QBO is not considered alone based on the presumption that the influence of the QBO on anomalous AR activity will primarily manifest via the modulation of the MJO's convection and its ability to elicit an extratropical response. Hence, the predictors investigated in this study are simply the daily MJO phase (1–8) and the monthly QBO phase (EQBO or WQBO).

4.4.4. EMPIRICAL PREDICTION

We generate a two-class prediction scheme from the DJFM AR anomaly time series for each region; that is, we assess the probability of being above and the probability of being below an "equal chances" 50th percentile of the time series given the initial state of the MJO and the QBO. As constructed, the probability of being above (increased AR activity) and below (decreased AR activity) are equal when all verification dates in DJFM are considered. However, the probability distribution may shift as a function of MJO phase, QBO phase, and forecast lead. For example, the distribution of 5-day average anomalous AR activity near British Columbia is shifted toward higher values 18 days following MJO phase 1 dates during EQBO conditions, relative to the mean DJFM distribution. As a result, given the initial conditions of MJO phase 1 and EQBO, the empirical scheme will predict increased AR activity for the British Columbia landfall boundary around 18 days following these initial conditions. In evaluating the two-class scheme, a prediction is considered correct when the observed response, in terms of above or below the 50th percentile threshold, from the 5-day running mean of the independent verification time series matches the predicted response; the prediction is considered incorrect otherwise. As illustrated by this example, the predictors are not explicitly weighted as they may be in a scheme based on some form of regression; in contrast, the predictors (MJO phase and QBO phase) are simply used to parse the training data in order to assess the conditional shift in the likelihood of increased or decreased AR activity relative to seasonal climatology. Though the results presented herein are based on the use of a single DJFM 50th percentile threshold, we find that the overarching conclusions (time-lagged response, patterns of increased/decreased AR activity, etc.) remain even if the threshold is allowed to vary by day-of-season. We use a leave-one-out cross-validation approach to conditionally construct and evaluate this prediction scheme (e.g., van den Dool 2007). Specifically, the verification statistics for a given season are based on distributions constructed from historical AR activity parsed by phase of the MJO and the QBO for all DJFM seasons excluding the one "left out" verification season, ensuring independence of the verification subset. As a given season is left out, we use the training data to generate forecasts for all 121 days within the left out season and for all possible forecast leads. In so doing, we perform this leave-one-out procedure 36 times, each time leaving out just one DJFM season from the available MERRA-2 record. Because the training periods differ during the leave-one-out process, the 50th percentile threshold is recalculated each time; however, the threshold value is nearly unchanged throughout the cross-validation.

The output of the cross-validation procedure is the number of correct and incorrect predictions parsed by initial conditions and forecast lead times.

4.4.5. Skill assessment

The skill of the prediction scheme is evaluated using the Heidke Skill Score (HSS), a measure of the proportion of correct forecasts (see, for example, van den Dool 2007; Johnson et al. 2014). The HSS is calculated as:

$$HSS = \frac{(H - E)}{(T - E)} \times 100,$$

where *H* is the number of correct forecasts, *T* is the total number of forecasts evaluated, and *E* is the number of correct forecasts expected by chance ($T/2$ in this two-class scenario). With the multiplication by 100, the two-class HSS ranges from -100 to 100. A set of perfect forecasts garners a HSS of 100, forecasts equivalent to the reference forecast (i.e., climatology) score 0, and forecasts less skillful than the reference forecast receive negative scores. The HSS values may be interpreted in terms of value added relative to a climatological reference forecast. For example, a HSS of 33 indicates twice as many correct forecasts as incorrect forecasts and a skill score of 50 indicates three times as many correct as incorrect forecasts; whereas, the reference forecast with a skill score of 0 indicates an equal number of correct and incorrect forecasts.

4.4.6. Significance of skill

A block bootstrapping approach is used to assess the statistical significance of the HSS values. For every conditional combination (i.e., MJO phase, QBO phase, and forecast lead), we generate a distribution of 1000 skill score values by randomly reassigning the calendar year and shifting the day-of-year indices of the "blocks" of the occurrences of the conditional data. We then perform the verification calculations on the random data in order to construct a distribution of resampled HSS values against which the actual conditional HSS may be compared. In doing so, each block bootstrap sample retains the sample size and potential autocorrelation associated with the conditional data.

4.4.7. Atmospheric river response assessment

For Figure 4.3 and the associated discussion we aim to not only communicate the skill within the prediction scheme, but also characterize the conditional AR response. To achieve this, we evaluate the shift in the probability of above and below normal AR activity for each conditional combination throughout the leave-one-out training and verification process. For example, if a given MJO phase, QBO phase, and forecast lead combination consistently produces a probability of above normal AR activity greater than the probability of below normal activity, we record the condition as resulting in above normal, or increased, AR activity and shade the combination green in Figure 4.3.

4.4.8. Model skill comparison

In order to provide a numerical weather prediction skill benchmark, we calculate HSS values for a set of 46-day ECMWF retrospective forecasts from 1995-2016. The ECMWF reforecast ensemble prediction system dataset consists of 11 members (one control and ten perturbed) that are created "on-the-fly." That is to say that the database is comprised of output from different versions of the ECMWF model, as reforecasts are produced progressively as the the operational model is updated (Vitart et al. 2017). We obtain instantaneous 0000 UTC variables on a $1.5^{\circ} \times 1.5^{\circ}$ latitude-longitude grid, from which we calculate IVT and identify AR-like features. We use the first 7 days from every available control run reforecast to calculate calendar-day means from which we calculate the seasonal cycle via fast Fourier transform. Time series of anomalous AR activity are created for each ensemble member's reforecasts by removing the control run's seasonal cycle and applying a 5-day running mean. The 50th percentile threshold used to evaluate AR activity is based on anomalies from the control run, subset for the boreal winter. Each member is evaluated separately and for all verification dates within DJFM. Following this approach, 1919 reforecasts are used.

CHAPTER 5

CONCLUDING REMARKS

5.1. SUMMARY AND SIGNIFICANCE OF RESULTS

The results in this dissertation document temporal and spatial variability in atmospheric river (AR) activity over the North Pacific. In general, this research reveals situations when the broader climate system is influencing weather. It is shown that large-scale mean state and circulation anomalies—to include those associated with modes of tropical variability—can influence AR activity, as well as the predictability thereof. Summarized below are some of the key results that increase the understanding of these oft-impactful features.

5.1.1. Chapter 2

ARs exist throughout the year within the North Pacific basin, but a clear seasonality exists in AR activity. The results in Chapter 2 reveal that this seasonality manifests itself more as a displacement of ARs toward the north and west during the boreal warm seasons than it does in a marked change in the total number of ARs that occur within the basin. Thus, studies that focus only on some representation of the boreal winter season may provide incomplete assessments of ARs, especially for domains that extend beyond the U.S. West Coast. Therefore, the seasonal cycle of AR activity for a given location of interest must be understood and conveyed as part of any research into AR activity.

The El Niño-Southern Oscillation (ENSO) cycle and the Madden-Julian oscillation (MJO)—the leading mode of interannual and intraseasonal tropical variability, respectively—can modulate AR activity, triggering changes upwards of +/- 40–50% of the local AR frequency of occurrence. Both modes of variability impact the displacement and occurrence of ARs in a way not unlike the seasonal cycle, but on different time scales. These results emphasize the close relationship between AR activity over the North Pacific and the eddy-driven jet, such that "where goes the storm track, goes the ARs." This relationship holds whether the jet modulation stems from the seasonal migration or as a result of tropical variability.

5.1.2. Chapter 3

Chapter 3 delivers new results regarding the modulation of landfalling AR activity and the character of high-latitude ARs that occur near southern Alaska. When compared to the well-documented AR activity along the U.S. West Coast, it is shown that both locations have similar annual AR frequencies of occurrence but different, yet pronounced, seasonal cycles in AR activity. Average AR characteristics (e.g., spatial dimensions, persistence, magnitude) are also similar between the regions.

Broad height anomalies over the northeast Pacific influence landfalling AR activity near southern Alaska and along the U.S. West Coast and can effect a "tradeoff" in AR activity between the two regions. For example, when a positive 500 hPa height anomaly exists over the northeast Pacific, AR activity is often deflected poleward toward Alaska. This increase in AR activity near Alaska comes at the cost of AR activity along the U.S. West Coast, which experiences a decrease in AR activity relative to climatology during the same conditions. The opposing relationship also applies. The results highlight that this modulation of AR activity by northeast Pacific height anomalies pertains to synoptic, subseasonal, and interannual time scales.

Both landfalling ARs and northeast Pacific height anomalies are associated with Rossby wave breaking; therefore, the "tradeoff" relationship is dynamically linked to the broader North Pacific. As a result, knowledge of the current or future state of the large-scale flow over the northeast Pacific—perhaps modulated by modes of tropical variability—may provide valuable, predictive information about the likelihood of AR activity over a range of time scales.

5.1.3. Chapter 4

Chapter 4 highlights the relationship between anomalous landfalling AR activity along the west coast of North America with a known (i.e., the MJO) and an emerging (i.e., the quasi-biennial oscillation (QBO)) source of subseasonal predictability. The results reveal that the time-lagged modulation of AR activity by the extratropical response to the MJO can be leveraged for skillful subseasonal forecasts. Additionally, the MJO–AR relationship can be better understood and predicted by also considering the state of the stratosphere. The results underscore the ability of tropical anomalies to elicit extratropical impacts. These relationships not only contribute to the subseasonal variability of ARs activity, but also support skillful predictions thereof.

An empirical prediction scheme based on the initial state of the MJO and the QBO supports skillful subseasonal predictions of anomalous AR activity. More specifically, during certain phase combinations (i.e., MJO phase, QBO phase, and forecast lead), the prediction scheme produces skill competitive with, or even exceeding, a state-of-the-art numerical weather prediction model. The resulting empirical predication scheme could be operationalized to help close the subseasonal gap in forecast guidance.

5.2. POSSIBLE EXTENSIONS

While this dissertation may represent the culmination of an academic endeavor, many open, applicable research questions still remain. Possible ways in which the research presented in this dissertation could be extended include, but are certainly not limited to, the topics briefly outlined in the subsections that follow.

5.2.1. ATMOSPHERIC RIVER METRICS

Much of the work in this dissertation derives from Boolean occurrence-based AR "hits" over a given grid point or landfall boundary. It would be interesting to extend the methods beyond these hit-based measures to metrics relating to accumulated transport. Consider, for example, NOAA's accumulated cyclone energy (ACE) metric for tropical cyclones or the related integrated kinetic energy (IKE) measure. Just as those quantities consider the frequency, duration, and/or intensity of tropical cyclones, a set of similar metrics could be used to characterize and categorize AR-like features. The AR detection algorithm could be extended to track features, thus enabling the integration of variables of interest (e.g., anomalous water vapor flux, mass flux) over an ARs life cycle. Such metrics may help to analyze individual AR events, but may also prove useful in characterizing activity over periods of time (e.g. more transport via ARs during one particular phase of the QBO or change in poleward flux in response to Arctic sea ice loss).

5.2.2. Quasi-Biennial Oscillation's Influence

The modulation of the MJO's extratropical response and the associated time-lagged AR impacts by the QBO that are documented in Chapter 4 demand further investigation. Idealized modeling studies could isolate the physical mechanisms that support the apparent influence of the state of the tropical stratosphere on the MJO's teleconnection patterns, whether the mechanisms manifest primarily via the modulation of the MJO itself or the ability of MJO-like heating to elicit an extratropical response. Furthermore, idealized simulations could help disentangle any ENSO influence on the QBO–MJO relationships. Additional research could also influence one's choice of QBO index (pressure level, amplitude threshold, etc.) and time lag to best characterize the modulation. The results of this type of modeling study could have scientific implications far beyond the subseasonal prediction of anomalous AR activity.

5.2.3. Prediction Scheme Enhancements

Numerous opportunities exist to extend the prediction scheme that is presented in Chapter 4. As noted in the text, the method could be brought closer to operations by employing a "do no harm" methodology to exploit the skillful "forecasts of opportunity" and then revert to a basic climatology forecast when no skill is expected. Then one could apply a suite of skill metrics (see, for example, Wilks 2006) to further assess the potential utility of such a scheme. The prediction scheme also has many prospects for refinement, such as choices of locations, thresholds, indices, forecast lead times, and season. The scheme could also be married to predictions of the MJO itself (e.g., Wang et al. 2014b), though employing a predictor that is also a predictand may dampen the already modest skill. Furthermore, the same predictors could be used for other predictands, as far more could be evaluated than just lagged AR activity impacts. Empirical predictions within the subseasonal time scale are not limited to the two-class scheme described in Chapter 4. Indeed, other approaches (see, for example, van den Dool 2007) may provide probabilistic output (e.g., logistic regression). Probabilistic output may be incredibly powerful for many decision makers, who could tailor actions based on predicted probabilities relative to some user-defined probability of occurrence value.

5.2.4. Location Impacts

Subregions and landfall boundaries are used throughout this dissertation to illustrate the climatology and variability of AR activity on a sub-basin scale. While the locations are of general societal importance and/or meteorological significance, they are also somewhat arbitrary. The results presented herein could be extended to capture and communicate AR activity near more "meaningful" locations. It may be a worthwhile exercise to translate these research results into actionable information, all while still communicating the requisite uncertainties. For example, could one quantify AR impacts (due to the seasonal cycle, the ENSO cycle, the MJO, etc.) for a location of interest, then communicate the likelihood of AR activity given the time of year and state of the tropics? Such an effort would help translate research to operations. The forecast-informed reservoir operations initiative being supported by the Center for Western Weather and Water Extremes at Scripps Institution of Oceanography may provide worthwhile examples relating to characterizing and communicating AR variability.

5.2.5. Madden-Julian Oscillation's Extratropical Response

Why do some MJO events appear to elicit a teleconnection response while others do not? The answer to this could benefit the interpretation and application of the results shown in this dissertation. A working hypothesis is the basic state must be receptive to interact with and communicate the anomalous divergence and convergence associated with the tropical convection. Maintaining an impact focus (i.e., modulation of landfalling AR activity), one could produce lag/lead composites of key atmospheric variables (e.g., jet, Rossby wave source) associated with MJO events with an observable response/impact compared to those without. Idealized modeling with prescribed heating could then be used to test the impact of varying key aspects of the basic state. Is the propensity to teleconnect sensitive to the strength of the anomalous heating, the character of the heating propagation (pulsing versus eastward progressing), and/or the state of the stratosphere? Perhaps this information could be used to generate a useful index, metric, and/or logic tree to convey the likelihood of a given MJO phase event to elicit an extratropical response. This investigation could also lead into an extension of the body of work regarding the tropical influence on extratropical wave packets (see Dole 2008, and references therein), features likely influential to and associated with ARs (e.g., Ralph et al. 2011).

REFERENCES

Adames, Á. F. and J. M. Wallace, 2014: Three-dimensional structure and evolution of the MJO and its relation to the mean flow. *J. Atmos. Sci.*, **71**, 2007–2026, doi:10.1175/JAS-D-13-0254.1.

American Meteorological Society, 2017: Atmospheric river. Glossary of Meteorology, [Available online at http://glossary.ametsoc.org/wiki/Atmospheric_river].

Arkin, P. A., 1982: The relationship between interannual variability in the 200 mb tropical wind field and the Southern Oscillation. *Mon. Wea. Rev.*, **110**, 1393–1404, doi:10.1175/1520-0493(1982)110⟨1393:TRBIVI⟩2.0.CO;2.

Baldwin, M. P., et al., 2001: The quasi-biennial oscillation. *Rev. Geophys.*, **39**, 179–229, doi:10.1029/1999RG000073.

Bao, J.-W., S. A. Michelson, P. J. Neiman, F. M. Ralph, and J. M. Wilczak, 2006: Interpretation of enhanced integrated water vapor bands associated with extratropical cyclones: Their formation and connection to tropical moisture. *Mon. Wea. Rev.*, **134**, 1063–1080, doi:10.1175/MWR3123.1.

Barnes, E. A. and L. M. Polvani, 2013: Response of the midlatitude jets, and of their variability, to increased greenhouse gases in the CMIP5 models. *J. Climate*, **26**, 7117–7135, doi:10.1175/JCLI-D-12-00536.1.

Berrisford, P., B. J. Hoskins, and E. Tyrlis, 2007: Blocking and Rossby wave breaking on the dynamical tropopause in the Southern Hemisphere. *J. Atmos. Sci.*, **64**, 2881–2898, doi:10.1175/JAS3984.1.

Black, J., N. Johnson, S. Baxter, S. Feldstein, D. Harnos, and M. L'Heureux, 2017: The predictors and forecast skill of Northern Hemisphere teleconnection patterns for lead times of 3-4 weeks. *Mon. Wea. Rev.*, doi:10.1175/MWR-D-16-0394.1, in press.

Bond, N. A., M. F. Cronin, H. Freeland, and N. Mantua, 2015: Causes and impacts of the 2014 warm anomaly in the NE Pacific. *Geophys. Res. Lett.*, **42**, 3414–3420, doi:10.1002/2015GL063306.

Brands, S., J. M. Gutiérrez, and D. San-Martín, 2016: Twentieth-century atmospheric river activity along the west coasts of Europe and North America: Algorithm formulation, reanalysis uncertainty and links to atmospheric circulation patterns. *Climate Dyn.*, 1–25, doi:10.1007/s00382-016-3095-6.

Branstator, G., 2014: Long-lived response of the midlatitude circulation and storm tracks to pulses of tropical heating. *J. Climate*, **27**, 8809–8826, doi:10.1175/JCLI-D-14-00312.1.

Browning, K. A. and C. W. Pardoe, 1973: Structure of low-level jet streams ahead of mid-latitude cold fronts. *Quart. J. Roy. Meteor. Soc.*, **99**, 619–638, doi:10.1002/qj.49709942204.

Capotondi, A., et al., 2015: Understanding ENSO diversity. *Bull. Amer. Meteor. Soc.*, **96**, 921–938, doi:10.1175/BAMS-D-13-00117.1.

Carlson, T. N., 1998: *Mid-latitude Weather Systems*. Amer. Meteor. Soc., 507 pp.

Clopper, C. and E. S. Pearson, 1934: The use of confidence or fiducial limits illustrated in the case of the binomial. *Biometrika*, **26**, 404–413, doi:10.1093/biomet/26.4.404.

Cordeira, J. M., F. M. Ralph, and B. J. Moore, 2013: The development and evolution of two atmospheric rivers in proximity to western North Pacific tropical cyclones in October 2010. *Mon. Wea. Rev.*, **141**, 4234–4255, doi:10.1175/MWR-D-13-00019.1.

Dacre, H. F., P. A. Clark, O. Martinez-Alvarado, M. A. Stringer, and D. A. Lavers, 2015: How do atmospheric rivers form? *Bull. Amer. Meteor. Soc.*, **96**, 1243–1255, doi:10.1175/BAMS-D-14-00031.1.

DelSole, T., L. Trenary, M. K. Tippett, and K. Pegion, 2017: Predictability of week-3–4 average temperature and precipitation over the contiguous United States. *J. Climate*, **30**, 3499–3512, doi: 10.1175/JCLI-D-16-0567.1.

Dettinger, M. D., 2013: Atmospheric rivers as drought busters on the U.S. West Coast. *J. Hydrometeor.*, **14**, 1721–1732, doi:10.1175/JHM-D-13-02.1.

Dettinger, M. D., F. M. Ralph, T. Das, P. J. Neiman, and D. R. Cayan, 2011: Atmospheric rivers, floods, and the water resources of California. *Water*, **3**, 445–478, doi:10.3390/w3020445.

Dole, R. M., 2008: *Linking weather and climate. Synoptic-Dynamic Meteorology and Weather Analysis and Forecasting, Meteor. Monogr.*, Vol. 33. Amer. Meteor. Soc., 51 pp.

Dufour, A., O. Zolina, and S. K. Gulev, 2016: Atmospheric moisture transport to the Arctic: assessment of reanalyses and analysis of transport components. *J. Climate*, **29**, 5061–5081, doi: 10.1175/JCLI-D-15-0559.1.

Gimeno, L., R. Nieto, M. Vázquez, and D. A. Lavers, 2014: Atmospheric rivers: a mini-review. *Front. Earth Sci.*, **2**, 2.1–2.6, doi:10.3389/feart.2014.00002.

GMAO, 2015: MERRA-2 inst6_3d_ana_Np: 3d, 6-Hourly, Instantaneous, Pressure-Level, Analysis, Analyzed Meteorological Fields V5.12.4. Greenbelt, MD, USA, Goddard Earth Sciences Data and Information Services Center (GES DISC), Accessed 2017-03-23, doi:10.5067/A7S6XP56VZWS.

Gottschalck, J., et al., 2010: A framework for assessing operational Madden-Julian oscillation forecasts: a CLIVAR MJO Working Group project. *Bull. Amer. Meteor. Soc.*, **91**, 1247–1258, doi: 10.1175/2010BAMS2816.1.

Guan, B., N. P. Molotch, D. E. Waliser, E. J. Fetzer, and P. J. Neiman, 2012a: Extreme snowfall events linked to atmospheric rivers and surface air temperature via satellite measurements. *Geophys. Res. Lett.*, **37**, L20 401, doi:10.1029/2010GL044696.

Guan, B., N. P. Molotch, D. E. Waliser, E. J. Fetzer, and P. J. Neiman, 2013: The 2010/2011 snow season in California's Sierra Nevada: Role of atmospheric rivers and modes of large-scale variability. *Water Resour. Res.*, **49**, 6731–6743, doi:10.1002/wrcr.20537.

Guan, B. and D. E. Waliser, 2015: Detection of atmospheric rivers: Evaluation and application of an algorithm for global studies. *J. Geophys. Res. Atmos.*, **120**, 12 514–12 535, doi:10.1002/2015JD024257.

Guan, B., D. E. Waliser, N. P. Molotch, E. J. Fetzer, and P. J. Neiman, 2012b: Does the Madden-Julian oscillation influence wintertime atmospheric rivers and snowpack in the Sierra Nevada? *Mon. Wea. Rev.*, **140**, 325–342, doi:10.1175/MWR-D-11-00087.1.

Hartmann, D. L., 2015: Pacific sea surface temperature and the winter of 2014. *Geophys. Res. Lett.*, **42**, 1894–1902, doi:0.1002/2015GL063083.

Henderson, S. A., E. D. Maloney, and E. A. Barnes, 2016: The influence of the Madden–Julian oscillation on Northern Hemisphere winter blocking. *J. Climate*, **29**, 4597–4616, doi:10.1175/JCLI-D-15-0502.1.

Higgins, R. W., J.-K. E. Schemm, W. Shi, and A. Leetmaa, 2000: Extreme precipitation events in the western United States related to tropical forcing. *J. Climate*, **13**, 793–820, doi:10.1175/1520-0442(2000)013⟨0793:EPEITW⟩2.0.CO;2.

Hoerling, M. P. and A. Kumar, 2002: Atmospheric response patterns associated with tropical forcing. *J. Climate*, **15**, 2184–2203, doi:10.1175/1520-0442(2002)015⟨2184:ARPAWT⟩2.0.CO;2.

Horel, J. D. and J. M. Wallace, 1981: Planetary-scale atmospheric phenomena associated with the Southern Oscillation. *Mon. Wea. Rev.*, **109**, 813–829, doi:10.1175/1520-0493(1981)109⟨0813:PSAPAW⟩2.0.CO;2.

Hoskins, B. J., 2013: The potential for skill across the range of the seamless weather-climate prediction problem: a stimulus for our science. *Quart. J. Roy. Meteor. Soc.*, **139**, 573–584, doi:10.1002/qj.1991.

Hoskins, B. J. and D. J. Karoly, 1981: The steady linear response of a spherical atmosphere to thermal and orographic forcing. *J. Atmos. Sci.*, **38**, 1179–1196, doi:10.1175/1520-0469(1981)038⟨1179:TSLROA⟩2.0.CO;2.

Jackson, D. L., M. Hughes, and G. A. Wick, 2016: Evaluation of landfalling atmospheric rivers along the U.S. West Coast in reanalysis data sets. *J. Geophys. Res. Atmos.*, **121**, 2705–2718, doi:10.1002/2015JD024412.

Jin, F. and B. J. Hoskins, 1995: The direct response to tropical heating in a baroclinic atmosphere. *J. Atmos. Sci.*, **52**, 307–319, doi:10.1175/1520-0469(1995)052⟨0307:TDRTTH⟩2.0.CO;2.

Johnson, N. C., D. C. Collins, S. B. Feldstein, M. L. L'Heureux, and E. E. Riddle, 2014: Skillful wintertime North American temperature forecasts out to 4 weeks based on the state of ENSO and the MJO. *Wea. Forecasting*, **29**, 23–38, doi:10.1175/WAF-D-13-00102.1.

Kim, H.-M. and M. A. Alexander, 2015: ENSO's modulation of water vapor transport over the Pacific-North American region. *J. Climate*, **28**, 3846–3856, doi:10.1175/JCLI-D-14-00725.1.

Kim, H.-M., D. Kim, F. Vitart, V. E. Toma, J.-S. Kug, and P. J. Webster, 2016: MJO propagation across the Maritime Continent in the ECMWF ensemble prediction system. *J. Climate*, **29**, 3973–3988, doi:10.1175/JCLI-D-15-0862.1.

Knapp, K. R., 2008: Scientific data stewardship of International Satellite Cloud Climatology Project B1 global geostationary observations. *J. Appl. Remote Sens.*, **2**, 023 548, doi:10.1117/1.3043461.

Knippertz, P. and H. Wernli, 2010: A Lagrangian climatology of tropical moisture exports to the Northern Hemispheric extratropics. *J. Climate*, **23**, 987–1003, doi:10.1175/2009JCLI3333.1.

Knippertz, P., H. Wernli, and G. Gläser, 2013: A global climatology of tropical moisture. *J. Climate*, **26**, 3031–3045, doi:10.1175/JCLI-D-12-00401.1.

Lavers, D. A., R. P. Allan, G. Villarini, B. Lloyd-Hughes, and A. J. Wade, 2013: Future changes in atmospheric rivers and their implications for winter flooding in Britain. *Environ. Res. Lett.*, **8**, 034 010, doi:10.1088/1748-9326/8/3/034010.

Lavers, D. A. and G. Villarini, 2013: The nexus between atmospheric rivers and extreme precipitation across Europe. *Geophys. Res. Lett.*, **40**, 3259–3264, doi:10.1002/grl.50636.

Lavers, D. A., G. Villarini, R. P. Allan, E. F. Wood, and A. J. Wade, 2012: The detection of atmospheric rivers in atmospheric reanalyses and their links to British winter floods and the large-scale climatic circulation. *J. Geophys. Res.*, **117**, D20 106, doi:10.1029/2012JD018027.

Lavers, D. A., D. E. Waliser, F. M. Ralph, and M. D. Dettinger, 2016: Predictability of horizontal water vapor transport relative to precipitation: Enhancing situational awareness for forecasting western U.S. extreme precipitation and flooding. *Geophys. Res. Lett.*, **43**, 2275–2282, doi:10.1002/2016GL067765.

Lee, M.-Y., C.-C. Hong, and H.-H. Hsu, 2015: Compounding effects of warm sea surface temperature and reduced sea ice on the extreme circulation over the extratropical North Pacific and North America during the 2013-2014 boreal winter. *Geophys. Res. Lett.*, **42**, 1612–1618, doi:10.1002/2014GL062956.

Liu, C. and E. A. Barnes, 2015: Extreme moisture transport into the Arctic linked to Rossby wave breaking. *J. Geophys. Res. Atmos.*, **120**, 3774–3788, doi:10.1002/2014JD022796.

Liu, C., X. Ren, and X. Yang, 2014a: Mean flow-storm track relationship and Rossby wave breaking in two types of El-Niño. *Adv. Atmos. Sci.*, **31**, 197–210, doi:10.1007/s00376-013-2297-7.

Liu, C., B. Tian, K.-F. Li, G. L. Manney, N. J. Livesey, Y. L. Yung, and D. E. Waliser, 2014b: Northern Hemisphere mid-winter vortex-displacement and vortex-split stratospheric sudden warmings: Influence of the Madden-Julian oscillation and quasi-biennial oscillation. *J. Geophys. Res. Atmos.*, **119**, 12 599–12 620, doi:10.1002/2014JD021876.

Maloney, E. D. and M. J. Dickinson, 2003: The intraseasonal oscillation and the energetics of summertime tropical western North Pacific synoptic-scale disturbances. *J. Atmos. Sci.*, **60**, 2153–2168, doi:10.1175/1520-0469(2003)060⟨2153:TIOATE⟩2.0.CO;2.

Marshall, A. G., H. H. Hendon, S.-W. Son, and Y. Lin, 2016: Impact of the quasi-biennial oscillation on predictability of the Madden-Julian oscillation. *Climate Dyn.*, doi:10.1007/s00382-016-3392-0, in press.

Matthews, A. J., 2004: Atmospheric response to observed intraseasonal tropical sea surface temperature anomalies. *Geophys. Res. Lett.*, **31**, L14 107, doi:10.1029/2004GL020474.

McGuirk, J. P., A. H. Thompson, and N. R. Smith, 1987: Moisture bursts over the tropical Pacific Ocean. *Mon. Wea. Rev.*, **115**, 787–798.

Moore, R. W., O. Martius, and T. Spengler, 2010: The modulation of the subtropical and extratropical atmosphere in the Pacific basin in response to the Madden-Julian oscillation. *Mon. Wea. Rev.*, **138**, 2761–2779, doi:10.1175/2010MWR3194.1.

Mundhenk, B. D., E. A. Barnes, and E. D. Maloney, 2016a: All-season climatology and variability of atmospheric river frequencies over the North Pacific. *J. Climate*, **29**, 4885–4903, doi:10.1175/JCLI-D-15-0655.1.

Mundhenk, B. D., E. A. Barnes, E. D. Maloney, and K. M. Nardi, 2016b: Modulation of atmospheric rivers near Alaska and the U.S. West Coast by northeast Pacific height anomalies. *J. Geophys. Res. Atmos.*, **121**, 12 751–12 765, doi:10.1002/2016JD025350.

Nayak, M. A., G. Villarini, and D. A. Lavers, 2014: On the skill of numerical weather prediction models to forecast atmospheric rivers over the central United States. *Geophys. Res. Lett.*, **41**, 4354–4362, doi:10.1002/2014GL060299.

Neiman, P. J., F. M. Ralph, G. A. Wick, Y.-H. Kuo, T.-K. Wee, Z. Ma, G. H. Taylor, and M. D. Dettinger, 2008a: Diagnosis of an intense atmospheric river impacting the Pacific Northwest: Storm summary and offshore vertical structure observed with COSMIC satellite retrievals. *Mon. Wea. Rev.*, **138**, 4398–4420, doi:10.1175/2008MWR2550.1.

Neiman, P. J., F. M. Ralph, G. A. Wick, J. D. Lundquist, and M. D. Dettinger, 2008b: Meteorological characteristics and overland precipitation impacts of atmospheric rivers affecting the west coast of North America based on eight years of SSM/I satellite observations. *J. Hydrometeor.*, **9**, 22–47, doi: 10.1175/2007JHM855.1.

Neiman, P. J., L. J. Schick, F. M. Ralph, M. Hughes, and G. A. Wick, 2011: Flooding in western Washington: The connection to atmospheric rivers. *J. Hydrometeor.*, **12**, 1337–1358, doi:10.1175/2011JHM1358.1.

Newell, R. E., N. E. Newell, Y. Zhu, and C. Scott, 1992: Tropospheric rivers? – A pilot study. *Geophys. Res. Lett.*, **19**, 2401–2404, doi:10.1029/92GL02916.

Newell, R. E. and Y. Zhu, 1994: Tropospheric rivers: A one-year record and possible application to ice core data. *Geophys. Res. Lett.*, **21**, 113–116, doi:10.1029/93GL03113.

Newman, M., G. N. Kiladis, K. M. Weickmann, F. M. Ralph, and P. D. Sardeshmukh, 2012: Relative contributions of synoptic and low-frequency eddies to time-mean atmospheric moisture transport, including the role of atmospheric rivers. *J. Climate*, **25**, 7341–7360, doi:10.1175/JCLI-D-11-00665.1.

Nishimoto, E. and S. Yoden, 2017: Influence of the stratospheric quasi-biennial oscillation on the Madden-Julian oscillation during Austral summer. *J. Atmos. Sci.*, **74**, 1105–1125, doi:10.1175/JAS-D-16-0205.1.

Palmén, E. and C. W. Newton, 1969: *Atmospheric Circulation Systems: Their Structure and Physical Interpretation*, International Geophysics Series, Vol. 13. Academic Press, 606 pp.

Papineau, J. and E. Holloway, 2011: The nature of heavy rain and flood events in Alaska. Anchorage Forecast Office Research Papers, NOAA/NWS/ARH, 20 pp. [Available online at http://citeseerx.ist.psu.edu/viewdoc/summary?doi=10.1.1.729.6444.].

Papineau, J. and E. Holloway, 2012: The dry side of atmospheric rivers in Alaska. Anchorage Forecast Office Research Papers, NOAA/NWS/ARH, 9 pp. [Available online at http://citeseerx.ist.psu.edu/viewdoc/summary?doi=10.1.1.729.4947.].

Payne, A. E. and G. Magnusdottir, 2014: Dynamics of landfalling atmospheric rivers over the North Pacific in 30 years of MERRA reanalysis. *J. Climate*, **27**, 7133–7150, doi:10.1175/JCLI-D-14-00034.1.

Pelly, J. L. and B. J. Hoskins, 2003: A new perspective on blocking. *J. Atmos. Sci.*, **60**, 743–755, doi: 10.1175/1520-0469(2003)060⟨0743:ANPOB⟩2.0.CO;2.

Radić, V., A. J. Cannon, B. Menounos, and N. Gi, 2015: Future changes in autumn atmospheric river events in British Columbia, Canada, as projected by CMIP5 global climate models. *J. Geophys. Res. Atmos.*, **120**, 9279–9302, doi:10.1002/2015JD023279.

Ralph, F. M., T. Coleman, P. J. Neiman, R. J. Zamora, and M. D. Dettinger, 2013: Observed impacts of duration and seasonality of atmospheric-river landfalls on soil moisture and runoff in coastal Northern California. *J. Hydrometeor.*, **14**, 443–459, doi:10.1175/JHM-D-12-076.1.

Ralph, F. M. and M. D. Dettinger, 2011: Storms, floods, and the science of atmospheric rivers. *Eos, Trans. Amer. Geophys. Union*, **92**, 265–272, doi:10.1029/2011EO320001.

Ralph, F. M. and M. D. Dettinger, 2012: Historical and national perspectives on extreme West Coast precipitation associated with atmospheric rivers during December 2010. *Bull. Amer. Meteor. Soc.*, **93**, 783–790, doi:10.1175/BAMS-D-11-00188.1.

Ralph, F. M., P. J. Neiman, G. N. Kiladis, K. Weickmann, and D. W. Reynolds, 2011: A multiscale observational case study of a Pacific atmospheric river exhibiting tropical/extratropical connections and a mesoscale frontal wave. *Mon. Wea. Rev.*, **139**, 1169–1189, doi:10.1175/2010MWR3596.1.

Ralph, F. M., P. J. Neiman, and R. Rotunno, 2005: Dropsonde observations in low-level jets over the northeastern Pacific Ocean from CALJET-1998 and PACJET-2001: Mean vertical-profile and atmospheric-river characteristics. *Mon. Wea. Rev.*, **133**, 889–910, doi:10.1175/MWR2896.1.

Ralph, F. M., P. J. Neiman, and G. A. Wick, 2004: Satellite and CALJET aircraft observations of atmospheric rivers over the eastern North Pacific ocean during the winter of 1997/98. *Mon. Wea. Rev.*, **132**, 1721–1745, doi:10.1175/1520-0493(2004)132⟨1721:SACAOO⟩2.0.CO;2.

Ralph, F. M., P. J. Neiman, G. A. Wick, S. I. Gutman, M. D. Dettinger, D. R. Cayan, and A. B. White, 2006: Flooding on California's Russian River: The role of atmospheric rivers. *Geophys. Res. Lett.*, **33**, L13 801, doi:10.1029/2006GL026689.

Ralph, F. M., et al., 2016: CalWater field studies designed to quantify the roles of atmospheric rivers and aerosols in modulating U.S. West Coast precipitation in a changing climate. *Bull. Amer. Meteor. Soc.*, **97**, 1209–1228, doi:10.1175/BAMS-D-14-00043.1.

Ralph, F. M., et al., 2017: Atmospheric rivers emerge as a global science and applications focus. *Bull. Amer. Meteor. Soc.*, **98**, 1–2, doi:10.1175/BAMS-D-16-0262.1, in press.

Riehl, H., T. C. Yeh, and N. E. La Seur, 1950: A study of variations of the general circulation. *J. Meteor.*, **7**, 181–194, doi:10.1175/1520-0469(1950)007⟨0181:ASOVOT⟩2.0.CO;2.

Rienecker, M. M., et al., 2011: MERRA: NASA's Modern-Era Retrospective Analysis for Research and Applications. *J. Climate*, **24**, 3624–3648, doi:10.1175/JCLI-D-11-00015.1.

Roberge, A., J. R. Gyakum, and E. H. Atallah, 2009: Analysis of intense poleward water vapor transports into high latitudes of western North America. *Wea. Forecasting*, **24**, 1732–1747, doi: 10.1175/2009WAF2222198.1.

Robertson, A. W., A. Kuma, M. Peña, and F. Vitart, 2015: Improving and promoting subseasonal to seasonal prediction. *Bull. Amer. Meteor. Soc.*, **96**, ES49–ES53, doi:10.1175/BAMS-D-14-00139.1.

Rutz, J. J., W. J. Steenburgh, and F. M. Ralph, 2014: Climatological characteristics of atmospheric rivers and their inland penetration over the western United States. *Mon. Wea. Rev.*, **142**, 905–920, doi:10.1175/MWR-D-13-00168.1.

Ryoo, J.-M., Y. Kaspi, D. W. Waugh, G. N. Kiladis, D. E. Waliser, E. J. Fetzer, and J. Kim, 2013: Impact of Rossby wave breaking on U.S. West Coast winter precipitation during ENSO events. *J. Climate*, **26**, 6360–6382, doi:10.1175/JCLI-D-12-00297.1.

Sampe, T. and S.-P. Xie, 2010: Large-scale dynamics of the meiyu-baiu rainband: Environmental forcing by the westerly jet. *J. Climate*, **23**, 113–134, doi:10.1175/2009JCLI3128.1.

Sardeshmukh, P. D. and B. J. Hoskins, 1988: The generation of global rotational flow by steady idealized tropical divergence. *J. Atmos. Sci.*, **45**, 1228–1251, doi:10.1175/1520-0469(1988)045⟨1228:TGOGRF⟩2.0.CO;2.

Scaife, A. A., et al., 2014: Predictability of the quasi-biennial oscillation and its northern winter teleconnection on seasonal to decadal timescales. *Geophys. Res. Lett.*, **41**, 1752–1758, doi:10.1002/2013GL059160.

Smith, B. L., S. E. Yuter, P. J. Neiman, and D. E. Kingsmill, 2010: Water vapor fluxes and orographic precipitation over Northern California associated with a landfalling atmospheric river. *Mon. Wea. Rev.*, **138**, 74–100, doi:10.1175/2009MWR2939.1.

Smith, T. M., R. W. Reynolds, T. C. Peterson, and J. Lawrimore, 2008: Improvements to NOAA's historical merged land-ocean surface temperature analysis (1880-2006). *J. Climate*, **21**, 2283–2296, doi:10.1175/2007JCLI2100.1.

Sodemann, H. and A. Stohl, 2013: Moisture origin and meridional transport in atmospheric rivers and their association with multiple cyclones. *Mon. Wea. Rev.*, **141**, 2850–2868, doi:10.1175/MWR-D-12-00256.1.

Son, S., Y. Lim, C. Yoo, H. Hendon, and J. Kim, 2017: Stratospheric control of Madden-Julian oscillation. *J. Climate*, **30**, 1909–1922, doi:10.1175/JCLI-D-16-0620.1.

Strong, C. and G. Magnusdottir, 2008: Tropospheric Rossby wave breaking and the NAO/NAM. *J. Atmos. Sci.*, **65**, 2861–2876, doi:10.1175/2008JAS2632.1.

Tyrlis, E. and B. J. Hoskins, 2008: The morphology of Northern Hemisphere blocking. *J. Atmos. Sci.*, **65**, 1653–1665, doi:10.1175/2007JAS2338.1.

van den Dool, H., 2007: *Empirical Methods in Short-Term Climate Prediction*. Oxford University Press, 215 pp.

Vitart, F. and F. Molteni, 2010: Simulation of the Madden-Julian oscillation and its teleconnections in the ECMWF forecast system. *Quart. J. Roy. Meteor. Soc.*, **136**, 842–855, doi:10.1002/qj.623.

Vitart, F., et al., 2017: The subseasonal to seasonal (S2S) prediction project database. *Bull. Amer. Meteor. Soc.*, **98**, 163–173, doi:10.1175/BAMS-D-16-0017.1.

Waliser, D. E., 2011: *Chapter 12, Intraseasonal Variability of the Atmosphere-Ocean Climate System*. 2d ed., Springer, Heidelberg, Germany, 613 pp., Predictability and Forecasting, W. K. M. Lau and D. E. Waliser, Eds.

Waliser, D. E., et al., 2012: The “year” of tropical convection (May 2008-April 2010): Climate variability and weather highlights. *Bull. Amer. Meteor. Soc.*, **93**, 1189–1218, doi:10.1175/2011BAMS3095.1.

Wang, S.-Y., L. Hipps, R. R. Gillies, and J.-H. Yoon, 2014a: Probable causes of the abnormal ridge accompanying the 2013–2014 California drought: ENSO precursor and anthropogenic warming footprint. *Geophys. Res. Lett.*, **41**, 3220–3226, doi:10.1002/2014GL059748.

Wang, W., M.-P. Hung, S. Weaver, A. Kumar, and X. Fu, 2014b: MJO prediction in the NCEP Climate Forecast System version 2. *Climate Dyn.*, **42**, 2509–2520, doi:10.1007/s00382-013-1806-9.

Warner, M. D., C. F. Mass, and E. P. Salathé Jr., 2012: Wintertime extreme precipitation events along the Pacific Northwest coast: Climatology and synoptic evolution. *Mon. Wea. Rev.*, **140**, 2021–2043, doi:10.1175/MWR-D-11-00197.1.

Warner, M. D., C. F. Mass, and E. P. Salathé Jr., 2015: Changes in winter atmospheric rivers along the North American west coast in CMIP5 climate models. *J. Hydrometeor.*, **16**, 118–128, doi:10.1175/JHM-D-14-0080.1.

Wheeler, M. C. and H. H. Hendon, 2004: An all-season real-time multivariate MJO index: Development of an index for monitoring and prediction. *Mon. Wea. Rev.*, **132**, 1917–1932, doi:10.1175/1520-0493(2004)132⟨1917:AARMMI⟩2.0.CO;2.

White, C. J., et al., 2017: Potential applications of subseasonal-to-seasonal (S2S) predictions. *Meteor. Appl.*, doi:10.1002/met.1654, in press.

Wick, G. A., P. J. Neiman, and F. M. Ralph, 2013a: Description and validation of an automated objective technique for identification and characterization of the integrated water vapor signature of atmospheric rivers. *IEEE Trans. Geosci. Remote Sens.*, **51**, 2166–2176, doi:10.1109/TGRS.2012.2211024.

Wick, G. A., P. J. Neiman, F. M. Ralph, and T. M. Hamill, 2013b: Evaluation of forecasts of the water vapor signature of atmospheric rivers in operational numerical weather prediction models. *Wea. Forecasting*, **28**, 1337–1352, doi:10.1175/WAF-D-13-00025.1.

Wilks, D. S., 2006: *Statistical Methods in the Atmospheric Sciences*, International Geophysics Series, Vol. 91. Academic Press, 627 pp.

Woods, C. and R. Caballero, 2016: The role of moist intrusions in winter Arctic warming and sea ice decline. *J. Climate*, **29**, 4473–4485, doi:10.1175/JCLI-D-15-0773.1.

Woods, C., R. Caballero, and G. Svensson, 2013: Large-scale circulation associated with moisture intrusions into the Arctic during winter. *Geophys. Res. Lett.*, **40**, 4717–4721, doi:10.1002/grl.50912.

Woollings, T., A. Hannachi, and B. Hoskins, 2010: Variability of the North Atlantic eddy-driven jet stream. *Quart. J. Roy. Meteor. Soc.*, **136**, 856–868, doi:10.1002/qj.625.

Woollings, T., B. Hoskins, M. Blackburn, and P. Berrisford, 2008: A new Rossby wave-breaking interpretation of the North Atlantic Oscillation. *J. Atmos. Sci.*, **65**, 609–626, doi:10.1175/2007JAS2347.1.

Yoo, C. and S.-W. Son, 2016: Modulation of the boreal wintertime Madden-Julian oscillation by the stratospheric quasi-biennial oscillation. *Geophys. Res. Lett.*, **43**, 1392–1398, doi:10.1002/2016GL067762.

Zhang, C., 2005: Madden-Julian oscillation. *Rev. Geophys.*, **43**, RG2003, doi:10.1029/2004RG000158.

Zhang, C., 2013: Madden-Julian oscillation: bridging weather and climate. *Bull. Amer. Meteor. Soc.*, **94**, 1849–1870, doi:10.1175/BAMS-D-12-00026.1.

Zhu, Y. and R. E. Newell, 1994: Atmospheric rivers and bombs. *Geophys. Res. Lett.*, **21**, 1999–2002, doi:10.1029/94GL01710.

Zhu, Y. and R. E. Newell, 1998: A proposed algorithm for moisture fluxes from atmospheric rivers. *Mon. Wea. Rev.*, **126**, 725–735, doi:10.1175/1520-0493(1998)126⟨0725:APAFMF⟩2.0.CO;2.

APPENDIX A

ATMOSPHERIC RIVER DETECTION ALGORITHM

A.1. OVERVIEW

This appendix outlines the atmospheric river (AR) detection algorithm that is used throughout this dissertation. The algorithm, written in the Python 2.7 programming language, is available online at `http://hdl.handle.net/10217/170619`. This algorithm follows the objective detection approaches of others (e.g., Lavers and Villarini 2013; Wick et al. 2013a; Payne and Magnusdottir 2014), but employs a unique technique of detecting AR-like features from within fields of anomalous integrated water vapor transport (IVT). The use of anomalies was found to be efficient and to benefit automated feature detection in large spatial (i.e., North Pacific) and temporal (i.e., sub-daily across all seasons) domains. Additionally, this algorithm was developed to facilitate climatological and dynamical analyses and compositing, more so than to output a definitive AR event atlas.

As in Nayak et al. (2014), no temporal persistence is required for the identification of an AR by this algorithm. In this approach, each feature of interest and time step is scrutinized independently. Differences, perhaps subtle, should be expected in output from an algorithm tuned to detect an event (i.e., one "hit" per feature lifecycle) versus this occurrence-based (i.e., one "hit" for each time step during which the criteria are met) approach. The AR frequencies of occurrence in this research are calculated based on the number of periods during which a detected AR exists over each grid point divided by the number of periods in the composite. Additionally, the presented AR period counts are determined by the number of periods during which an AR-like feature extended sufficiently into the subregion of interest, not as a count of distinct ARs per se. While such results may be weighted by persistent events, this influence is not inappropriate as the persistence of an AR over an area greatly affects its potential impacts (Ralph et al. 2013).

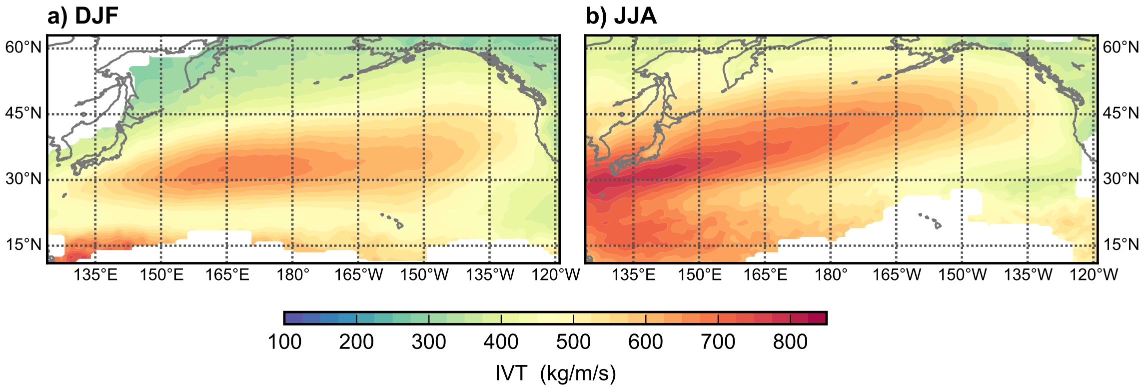

FIG. A.1. Seasonal mean comparable, or equivalent, full-field IVT values associated with the static 250 kg m^{-1} s^{-1} anomalous IVT threshold, calculated from all points along the periphery of retained AR-like features for (a) December–February (DJF) and (b) June–August (JJA). Grid locations with fewer than four detected AR perimeter points are masked.

A.2. METHODOLOGY

The algorithm begins by reading in pre-calculated IVT data. Scrutinizing each time period separately, a two-dimensional array of IVT anomaly values is created by removing the IVT mean and seasonal cycle as described in Section 2.2. An anomalous IVT magnitude threshold of 250 kg m^{-1} s^{-1} is then used to isolate so-called features of interest. While the 250 kg m^{-1} s^{-1} anomaly threshold is itself static and fixed within the algorithm, the comparable full-field IVT threshold value varies spatially and temporally as the underlying mean and seasonal cycle from which the anomalies are calculated vary spatially and/or temporally. Figure A.1 depicts the seasonal mean comparable, or equivalent, full IVT values associated with the static anomaly detection threshold for two contrasting three-month seasons. The basin-wide mean values in Figure A.1 are approximately 475 kg m^{-1} s^{-1} and 550 kg m^{-1} s^{-1} for December–February (DJF) and June–August (JJA), respectively. A direct comparison of threshold values between this and other algorithms is complicated by the use of IVT anomaly fields in this approach. However, it is clear from Figure A.1 that the 250 kg m^{-1} s^{-1} anomaly threshold cannot be considered as equivalent to a 250 kg m^{-1} s^{-1} full-field IVT threshold for the majority of periods and locations. An alternative percentile-based threshold approach may produce results that are similar to this anomaly method, provided the distributions from which the percentiles are calculated are allowed to vary spatially and temporally.

To emphasize large-scale features, those features encompassing less than 150 contiguous grid points on the MERRA $\frac{1}{2}^{\circ} \times \frac{2}{3}^{\circ}$ grid are removed. The remaining anomalous IVT features are then labeled and retained for individual assessment. Characteristics of each remaining feature of interest are determined using standard image processing techniques. These characteristics are passed through layered logic and thresholding in order to retain only those features of interest that exhibit AR-like characteristics. First, the length of the major axis of the feature and ratio of major axis length to minor axis length are tested, requiring a minimum of 25 grid points (approximately 1,400 km, but variable based on position within the domain) and a ratio of 1.6:1, respectively, to ensure that the features are of the appropriate spatial scale and are plume-like in nature. Second, comparatively weak features with a mean anomalous IVT intensity less than 305 kg m^{-1} s^{-1} and/or those west–east oriented features with a center of mass equatorward of 20°N and orientation off the parallels of less than 0.95 radians are believed to be associated more with broad/lower-frequency moisture swells and are removed. The eccentricity of a representative ellipse with the same second moments as each feature is then evaluated to eliminate those remaining features that still lack the requisite filament-like character, but were not captured by the earlier length/width test. The logic then assesses low-latitude features and removes those more representative of a well-developed tropical cyclone (i.e., intense circular features or features with tropical cyclone eye-like holes in the IVT anomaly field).

Features of interest that remain following the first round of logic are then evaluated to determine if multiple IVT anomaly peaks exist within each feature. The 250 kg m^{-1} s^{-1} IVT anomaly threshold is conservative by design, but does occasionally result in "connected" anomalous IVT features, a subsection of which may be an actual AR. If multiple IVT anomaly peaks exist within a feature, the feature is segmented surrounding the peaks and then each segment's eccentricity, mean intensity, and orientation are scrutinized for possible removal. These segmented features are flagged within the archive to afford a straightforward and deliberate inclusion or exclusion of these features during AR analyses.

Approximately 66% of the features identified in the 36-year MERRA dataset are retained by this detection methodology. Figure A.2 displays an example of the ability of the algorithm to detect AR features for an individual period. The majority of eliminated features are removed early in the algorithm due to their dimensions (e.g., too small in size or too low of a length/width aspect ratio). Varying the static thresholds within reasonable limits slightly impacts the total number of retained features by 1–3%. Furthermore, the order of the logical tests has little impact on the outcome of the overall algorithm, suggesting a fair amount of overlap among the series of logic tests and that no individual test is sufficient to eliminate all non-AR features.

In an effort to create a robust detection scheme that is applicable across the entire basin and all seasons, the static thresholds employed are more numerous, but perhaps not as stringent as those described in studies with more focused spatial and temporal scales (i.e., ARs making landfall along the U.S. West Coast during boreal winter). A manual review of a subset of detected features suggests that the thresholds used here are viable and important to provide a basin-wide, year round view of ARs, while still predominantly capturing significant filament-like regions of water vapor transport. As much of the imbedded logic relates to discerning ARs from tropical features in the lower latitudes of the domain (see code for details), several logic tests could be eliminated for a domain that does not extend into the tropics.

A.3. PERFORMANCE AND YIELD

There exists no real, objective way to score this algorithm short of a manual comparison over the entire period of interest; however, such an approach is unreasonable—and arguably unnecessary—to facilitate these climatological analyses. Instead, a panel-by-panel visual comparison between the output and satellite imagery was performed for a random subset of the periods and facilitated the tuning of the static thresholds. For example, the 250 kg m^{-1} s^{-1} threshold was observed to reliably outline the characteristic filamentary extent of ARs in the dataset, whereas a higher initial threshold often only captured the most intense region within each AR, thereby reducing the spatial expanse of the identified features. Visual inspection suggests that the vast majority of the retained features—even those near the periphery of the domain—are indeed filament-like, focused regions of water vapor transport.

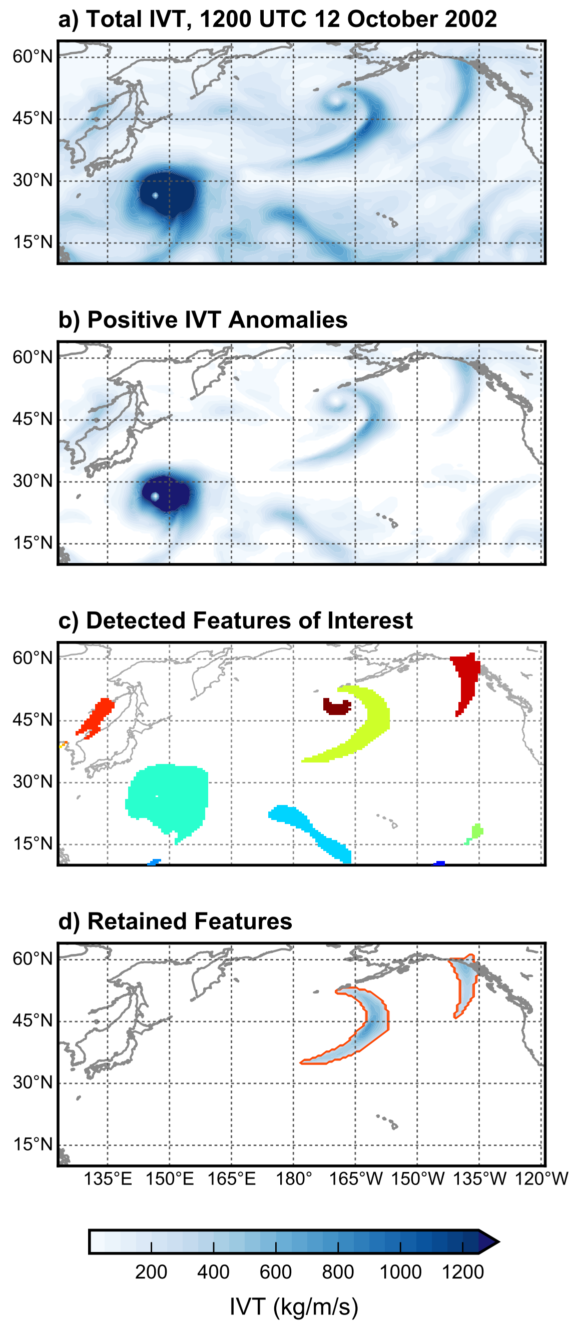

FIG. A.2. An example of the ability of the algorithm to detect AR-like features in MERRA-based output from 1200 UTC 12 October 2002.

Running the detection algorithm over 36-years of MERRA data at 6-hourly resolution results in 84,462 features identified as possible ARs, the centers of mass of which fall within the defined North Pacific domain. For the results presented in Chapters 2 and 3, the aforementioned segmented features with multiple IVT anomaly peaks are excluded, reducing the total number of AR features available for analysis to 81,409. The omission of the 3,053 segmented features has little impact on the depicted composites and no bearing on the conclusions. In addition to the information regarding the time of occurrence and location of each AR, the detection algorithm also provides information regarding each feature's character, to include approximations of feature length, width, orientation, anomalous water vapor flux, etc.

A.4. UPDATES

The AR detection algorithm detailed in the preceding sections was published, with slight modifications, as an appendix in Mundhenk et al. (2016a) and detailed the algorithm's application specifically with respect to MERRA output. Output from the algorithm also enabled the analysis in Mundhenk et al. (2016b). Since that time, the detection scheme has been modified for enhanced applicability.

First, the static anomaly threshold values have been recast as percentile values from a distribution of anomalous IVT. For example, the static 250 kg m^{-1} s^{-1} anomaly threshold has been replaced by a value representing the 94th percentile of the all-season distribution of daily IVT anomaly values over the North Pacific Ocean. This conversion to a dataset-dependent value affords enhanced comparisons between datasets that are less sensitive to any underlying biases in winds and/or specific humidity.

Second, some of the logic tests have been modified to enable their easy inclusion/exclusion within the detection scheme. For example, the algorithm has been applied to daily mean model output at comparatively coarse 1.5° and 2° horizontal resolution (not shown). At these resolutions, the multiple peak logic is not as necessary, thus version of the detection scheme used does not contain the logic that scrutinizes "connected" features within fields of anomalous IVT. Mid- and high-latitude results are generally insensitive to the removal of this logic test.

Third, the detection scheme was altered to improve feature handling around edges of the domain and to better handle different latitude-longitude grids. Additional updates are planned to bolster the algorithm's performance on a continuous, global domain.

APPENDIX B

DATA AVAILABILITY

Listed below are the key datasets and indices used in this dissertation and, when available, applicable URLs valid as of the submission date.

ECMWF reforecasts via the World Weather Research Programme/World Climate Research Programme Subseasonal-to-Seasonal Prediction Project database
`http://apps.ecmwf.int/datasets/data/s2s/`

ENSO index (i.e., ONI) via the National Oceanic and Atmospheric Administration National Weather Service Climate Prediction Center (NOAA NWS CPC)
`http://www.cpc.ncep.noaa.gov/products/analysis_monitoring/ensostuff/ensoyears.shtml`

MERRA via the NASA Global Modeling and Assimilation Office and Goddard Earth Sciences Data and Information Services Center (GMAO GES DISC)
`https://disc.gsfc.nasa.gov/`

MERRA-2 via the NASA GMAO GES DISC
`https://disc.gsfc.nasa.gov/`

MJO index (i.e., RMM) via the Australian Bureau of Meteorology
`http://www.bom.gov.au/climate/mjo/`

MJO indices (i.e., FMO, OMI, and VPM) via the NOAA Earth System Research Laboratory
`https://www.esrl.noaa.gov/psd/mjo/mjoindex/`

QBO index via the NOAA NWS CPC
`http://www.cpc.ncep.noaa.gov/data/indices/qbo.u50.index`

Rossby wave breaking data courtesy of Chengji Liu, see Liu et al. (2014a)